The Role of Various Geometrical Structures in Scalar Advection-Diffusion

Thesis by

Shubhro Ghosh

In Partial Fulfillment of the Requirements

for the Degree of

Doctor of Philosophy

California Institute of Technology

Pasadena, California

1994

(Submitted May 26, 1994)

Acknowledgements

I thank my principal advisor, Professor Stephen Wiggins, for his guidance and support. As his research assistant I enjoyed a lot of freedom in my work, for which I am very grateful. I also thank my co-advisor, Professor Anthony Leonard, for his help and guidance. I owe thanks to Professor Anthony E. Perry – who was a Sherman Fairchild distinguished visiting scholar during my first year at Caltech – for offering me help and encouragement with Part II of this thesis. Finally, I would like to offer thanks to Professor John Brady for taking the time to discuss the problem studied in Part II during the early stages of that project. This research was supported by a grant from the Air Force Office of Scientific Research, Grant No. AFOSR-91-0241.

Abstract

This thesis is divided in two parts: in Part I, using a time-periodic perturbation of a two-dimensional steady separation bubble on a plane no-slip boundary to generate chaotic particle trajectories in a localized region of an unbounded boundary-layer flow, we study the impact of various geometrical structures that arise naturally in chaotic advection fields on the transport of a passive scalar from a local "hot spot" on the no-slip boundary. We consider here the full advection-diffusion problem, though attention is restricted to the case of small scalar diffusion, or large Peclet number. In this regime, a certain one-dimensional unstable manifold is shown to be the dominant organizing structure in the distribution of the passive scalar. In general, it is found that the chaotic structures in the flow strongly influence the scalar distribution while, in contrast, the flux of passive scalar from the localized active no-slip surface is, to dominant order, independent of the overlying chaotic advection. Increasing the intensity of the chaotic advection by perturbing the velocity field further away from integrability results in more non-uniform scalar distributions, unlike the case in bounded flows where the chaotic advection leads to rapid homogenization of diffusive tracer. In the region of chaotic particle motion the scalar distribution attains an asymptotic state which is time-periodic, with the period same as that of the time-dependent advection field. Some of these results are understood by using the shadowing property from dynamical systems theory. The shadowing property allows us to relate the advection-diffusion solution at large Peclet numbers to a fictitious zero-diffusivity or frozen-field solution – the so-called stirring solution – corresponding to infinitely large Peclet number. The zero-diffusivity solution is an unphysical quantity, but it is found to be a powerful heuristic tool in understanding the role of small scalar diffusion. A novel feature in

this problem is that the chaotic advection field is adjacent to a no-slip boundary. The interaction between the necessarily non-hyperbolic particle dynamics in a thin near-wall region with the strongly hyperbolic dynamics in the overlying chaotic advection field is found to have important consequences on the scalar distribution; that this is indeed the case is shown using shadowing. Comparisons are made throughout with the flux and the distributions of the passive scalar for the advection-diffusion problem corresponding to the steady, unperturbed, integrable advection field.

In Part II, the transport of a passive scalar from a no-slip boundary into a two-dimensional steady boundary-layer flow is studied in the vicinity of a laminar separation point, where the dividing streamline – which is also a one-dimensional unstable manifold – is assumed to be normal to the boundary locally near the separation point. The novelty of the ensuing convection-diffusion process derives from the convective transport normal to the active boundary resulting from convection along the dividing streamline, and because of which the standard thermal boundary-layer approximations become invalid near the separation point. Using only the topology of the laminar, incompressible separated flow, a local solution of the Navier-Stokes equations is constructed in the form of a Taylor-series expansion from the separation point. The representation is universal, without regard to the outer inviscid flow and it is used in obtaining an asymptotically exact solution for the steady scalar distribution near the separation point at large Peclet number, using matched asymptotic expansions. The method demonstrates the application of local solutions of the Navier-Stokes equations in seeking asymptotic solutions to convection-diffusion problems. Verification of the asymptotic result is obtained from numerical computations based on the Wiener bundle solution – which is particularly well-suited to the large-Peclet-number transport problem.

Table of Contents

PART I

Diffusion of a passive scalar from a no-slip boundary into a two-dimensional chaotic advection field

Chapter 1

Introduction

The kinematics of a perfect or non-diffusive tracer is purely advective. In other words, perfect tracer particles will follow the pathlines of the flow. The dispersion of these particles is then directly related to the fluid particle trajectories and, in Eckart's terminology (see Eckart 1948), is called "stirring." Given some initial distribution of perfect tracer particles, how this distribution evolves in time is entirely dependent on the dynamics of particle motion in the flow, and therefore the associated transport issues are often best understood using the global geometrical viewpoint of dynamical systems theory. In stirring by chaotic advection (Aref 1984), the individual particle trajectories might be very complicated, but the underlying geometrical structures such as invariant manifolds and homoclinic/heteroclinic tangles provide a dynamical template that in certain cases considerably simplifies questions related to the transport or dispersion of particles (e.g., see Wiggins 1992). A more realistic scalar impurity will, however, undergo both advection and diffusion. Thus the time-evolution of some given initial scalar field will be dictated not only by the purely fluid-mechanical stirring process but also by the generally slower process of molecular diffusion of the now diffusive tracer, which is called "mixing"

(Eckart 1948). In the Lagrangian framework, the kinematics of a diffusive tracer has a Brownian-motion-component in addition to the advective component due to the fluid motion, and tracer particles no longer follow the pathlines of the flow. That raises several fundamental questions regarding the role of the underlying geometrical structures in the transport of a passive scalar and the manner in which they influence the time-evolution of a scalar field, particularly at small scalar diffusivities. Moreover, scalar advection in chaotic flows creates fine-scale structure since the attendant strong stretching and folding operations result in arbitrarily small striation thicknesses (Aref & Jones 1989, Jones 1991), so that even asymptotically small diffusivity cannot be ignored. It is therefore also a matter of considerable practical importance to incorporate small scalar diffusion. Among other considerations are the relationship between the stirring and mixing processes, in particular how small scalar diffusion affects the zero-diffusivity solution corresponding to pure advection.

An important isssue which has been mostly ignored in the existing literature is the transport of a passive scalar from an active no-slip boundary into a chaotic advection field, even though heat and mass transfer from stationary surfaces is common in engineering applications. A stagnation point (or, fixed point) is called *hyperbolic* if the velocity field expanded about the stagnation point has no eigen values with zero real part. The linear part of the velocity field expanded about any stagnation point on the no-slip boundary has zero eigen-values, and therefore every point on the no-slip boundary is non-hyperbolic. The non-hyperbolicity of the stagnation points on a no-slip boundary makes analysis difficult. Further, stirring, by itself, becomes meaningless since diffusion is essential for "lifting" heat or a passive impurity from the active no-slip surface. Given these complications, it is not clear how the geometrical structures in a chaotic advection field adjacent to an

active no-slip surface can influence the time-dependent distribution of the scalar field as the scalar impurity diffuses into the flow. Our objective is to investigate some of these issues using a simple two-dimensional time-periodic separation bubble with chaotic particle trajectories, over a plane stationary surface.

We use a method devised by Perry & Chong (1986a) to obtain a simple Taylor-series representation of a chaotic separation bubble which is also an asymptotically exact solution of the Navier-Stokes and continuity equations, close to the origin of the series-expansion. The method relies on the availability of sufficient number of topological constraints (Perry & Chong 1986a) and is therefore particularly well-suited to study steady two- and three-dimensional separated flows (Perry & Chong 1986a, Tobak & Peake 1982, Dallmann 1988) on account of their readily available topological features such as location and stability-type of stagnation points, location of points of zero shear-stress on the no-slip boundary, angles of separation and attachment, etc. Our scheme is to construct a low-order series-representation of a steady two-dimensional separation bubble at a plane wall and then introduce time-periodic terms to obtain an unsteady bubble with chaotic particle trajectories, such that the representation satisfies incompressibility and remains an asymptotically exact solution of the now time-dependent Navier-Stokes equations. The truncated series-solution constitutes a simple time-periodic perturbation of an integrable dynamical system. There are methods (Perry & Chong 1986a) for testing the accuracy of a truncated series-solution over any given region of the flow, but we will not concern ourselves with identifying a domain of applicability of the series-solution since attention will be mostly confined to regions close to the origin of the expansion. Only a localized portion of the plane wall is considered as an active surface such that finite-time distributions of the scalar field remain confined near the origin of the series-expansion.

The relative importance of advection versus diffusion is measured by the Peclet number, which is the ratio of the diffusion and advection time-scales. We are interested in the regime of small scalar diffusion, or more precisely, the regime where the diffusion time-scale is much greater than the advection time-scale, which means large Peclet numbers. At large Peclet numbers, the scalar advection-diffusion problem is best tackled by random-walk methods based on the theory of Brownian motion (Wang & Uhlenbeck 1945), and we develop numerical implementations of these methods to solve for the time-dependent scalar field. We introduce a fictitious "zero-diffusivity" solution as a heuristic tool in demonstrating the role of the underlying geometrical structures in the flow and in interpreting the role of slow mixing as a local smoothing of fine-scale structure in the scalar field, created by the stirring process.

The hyperbolic invariant set (Smale 1967) associated with Smale horseshoes (Smale 1967) is the prototype of a chaotic dynamical system, and the *shadowing lemma* (Bowen 1975) from dynamical systems theory is one of the fundamental results for the dynamics on a hyperbolic invariant set. Recent work of Klapper (1992a) has used shadowing theory (Anosov 1967, Bowen 1975) to study the small-diffusivity scalar advection-diffusion problem. Asymptotic results were obtained for the restricted class of uniformly hyperbolic systems, and therefore apply to typical chaotic processes in only a non-rigorous sense. Justification (Klapper 1992a) for its validity is based on existing numerical evidence (Hammel, Yorke & Grebogi 1987, 1988, Grebogi *et al.* 1990) that typical chaotic dynamical processes have the shadowing property. In a rough sense, a dynamical system that has the shadowing property is guaranteed to have a deterministic orbit that remains close to any noisy orbit with bounded noise, where how "close" depends on the noise level. The shadowing property has been used previously to reduce bounded additive noise in

orbits generated by chaotic dynamical systems (Hammel 1990, Farmer & Sidorowich 1991). That the shadowing property can be used to treat scalar diffusion is not surprising since diffusion can be regarded as a noisy component in the kinematics of a diffusive tracer. We use these ideas to develop a qualitative understanding of our random-walk solutions of the time-dependent scalar field and the interplay between the stirring and mixing processes. It is found that increased chaotic advection produces more localized and non-uniform distributions, even in regions of the flow that have no islands of stability bounded by invariant closed curves; near integrability, such curves will be provided by Kolmogorov-Arnold-Moser (KAM) tori and island bands, but as one perturbs the dynamical system further away from integrability there are no surviving invariant closed curves, and we choose such a parameter-regime to emphasize our result. The phenomenon contrasts sharply with that in the case of chaotic advection in bounded domains where the chaotic particle motion promotes rapid homogenization (Jones 1991) of diffusive tracer, giving rise to an asymptotically uniform scalar distribution. Reasons for this phenomenon are sought using shadowing theory. For the sake of comparison we also present computations of the scalar field for a set of parameters at which islands bounded by KAM tori occupy a significant portion of the flow region above the plane active surface, though the presence of large islands of regular particle motion precludes the possibility of applying shadowing theory. The form of the asymptotic distribution and the time-scale over which it is attained is also intimately linked with the geometrical structures in the flow, and the connection is made explicit by considering the details of exact dynamical trajectories that "shadow" the "noisy" Wiener trajectories of a diffusive tracer. We also show how the presence of the plane wall and the consequent regular dynamics of particles in a narrow near-wall region strongly influences the time-evolution of the scalar field, thus underlining the role of non-hyperbolicity

at the wall. In engineering applications the flux of passive scalar, integrated over the active surface, is a quantity of considerable practical importance; our computations show it is largely independent of the details of the chaotic advection-diffusion phenomena above the wall. Dominant balance arguments in the thermal boundary-layer adjacent to the active no-slip surface further clarify this issue.

Part I of this thesis is organized as follows. In Chapter 2 we construct an approximate representation of a chaotic separation bubble over a plane wall. In Chapter 3 we set up the scalar advection-diffusion problem. Numerical schemes are developed to obtain finite-time solutions of the large-Peclet-number or small-diffusivity advection-diffusion problem. In Chapter 4, a "zero-diffusivity" solution is constructed by solving for the scalar field in the thermal boundary-layer at the wall at small time and treating this as an "initial distribution" of perfect tracers which is subsequently stirred but not mixed by chaotic advection. In Chapter 5 we apply shadowing theory to our scalar advection-diffusion problem. We end with a discussion and concluding remarks in Chapter 6.

Chapter 2

Time-periodic separation bubble at a plane wall

We first construct a viscous, incompressible, two-dimensional flow that has the topology of a steady separation bubble at a plane wall in the form of a Taylor-series expansion from a point on the no-slip boundary. The construction suggests ways in which time-dependent terms can be introduced in the vector field such that one obtains an asymptotically exact representation of a time-periodic bubble with chaotic particle trajectories. The advantage of the Taylor-series expansion method (Perry & Chong 1986a) is that one can generate boundary-layer flows, especially separation patterns with desired topological features, as local Taylor-series expansions to arbitrary order, without regard to the outer inviscid flow. The method assumes the solutions of the continuity and Navier-Stokes equations for incompressible flow are smooth. For considerations related to the existence and uniqueness of smooth solutions, see Ladyzhenskaya (1975).

2.1 Construction of a local Taylor-series representation of the flow field

A point on the plane wall is chosen to be the origin for two-dimensional rect-

angular coordinates (x_1, x_2), where x_1 is a coordinate along the wall and x_2 is the coordinate normal to the wall. The velocity vector $u(x,t)$, $x \equiv (x_1, x_2) \in \mathbb{R}^1 \times \mathbb{R}^+$, $u \in \mathbb{R}^2$, is written in the form of an asymptotic third-order expansion from the origin

$$u_i = A_i + A_{ij}x_j + A_{ijk}x_jx_k + A_{ijkl}x_jx_kx_l + O(4), \tag{2.1}$$

where $O(m)$ represents a homogeneous polynomial of degree $n \geq m$. The $i, j, k, \ldots$'s can take values of 1 or 2, since the flow is two-dimensional. The coefficients A_i, A_{ij}, etc. are functions of time if the flow is unsteady, and they are symmetric tensors in all indices except the first. The number of independent coefficients, N_c, in our two-dimensional third-order expansion is easily determined (Perry & Chong 1986a), $N_c = 20$. The basic idea behind the method is to force the tensor coefficients $A_{ijk..}$'s to satisfy the Navier-Stokes and continuity equations, as well as boundary and symmetry conditions. The number of unknown independent tensor coefficients is greater than the number of equations generated from the Navier-Stokes equations, continuity equations and no-slip constraints, and the difference between the number of unknown coefficients and the number of connecting relationships grows rapidly with increasing order of the expansion. The "extra" coefficients are determined using the topological constraints that are prescribed by the desired topology of the separation pattern. The greater the order of the expansion, the more is the number of topological constraints required to close the problem.

Applying the no-slip constraint at the wall ($x_2 = 0$) on the third-order expansion of (2.1) specifies eight independent tensor coefficients to be identically zero. The equation of continuity yields six relationships which, combined with the no-slip constraint, forces yet another three coefficients to vanish, leaving the following three relationships:

$$A_{112} + A_{222} = 0, \tag{2.2a}$$

$$A_{1112} + A_{2212} = 0, \tag{2.2b}$$

$$A_{1122} + A_{2222} = 0. \tag{2.2c}$$

Following Perry & Chong (1986a), we specify the boundary vorticity $w(x_2 = 0)$ to vary according to the equation

$$w(x_2 = 0) \equiv -\frac{\partial u_1}{\partial x_2}\bigg|_{x_2=0} = -K(x_1^2 - x_s^2), \tag{2.3}$$

with $K > 0$, thus generating two points of zero shear-stress on the wall at $(-x_s, 0)$ and $(+x_s, 0)$, which act as a point of separation and a point of attachment, respectively. We note that in the time-dependent flow the parameter K can be a function of time. From (2.1) and (2.3) one obtains

$$A_{12} = -Kx_s^2, \; A_{112} = 0, \; A_{1112} = K/3,$$

and using (2.2a) and (2.2b) gives,

$$A_{222} = 0, \; A_{2212} = -K/3.$$

The time-dependent Navier-Stokes equations yields one ordinary differential equation (see Perry & Chong 1986b)

$$\dot{A}_{12} = 6\nu[2A_{1112} + A_{1222}], \tag{2.4}$$

where ν is the kinematic viscosity of the fluid. Four independent coefficients are still unspecified. Only two connecting relationships are available : (2.2c) from continuity, and (2.4) from the Navier-Stokes equations. Expressing the asymptotic expansion of (2.1) in terms of the known and unknown coefficients gives

$$\begin{aligned} u_1 &= -Kx_s^2x_2 + A_{122}x_2^2 + Kx_1^2x_2 + 3A_{1122}x_1x_2^2 + A_{1222}x_2^3 + O(4), \\ u_2 &= -Kx_1x_2^2 + A_{2222}x_2^3 + O(4). \end{aligned} \tag{2.5}$$

Consider first the time-independent problem. At steady-state, (2.4) yields

$$A_{1222} = -2K/3.$$

There are now only two independent unknown coefficients. These are specified using the two topological constraints that (2.5) must satisfy in order that the steady flow field has the topology of a symmetrical (about the origin) separation bubble, and these are : (1) symmetry condition on u_2, requiring $u_2(x_1 = 0, x_2) = 0$, (2) elliptic stagnation point at $(0, x_2^*)$, $0 < x_2^* \ll 1$; a stagnation point on the plane is called *elliptic* if the velocity field linearized about the stagnation point has a purely imaginary pair of eigen values. Condition (1) specifies $A_{2222} = 0$, and it follows from (2.2c), $A_{1122} = 0$. Substituting these in (2.5) and applying condition (2) gives,

$$-Kx_s^2 + A_{122}x_2^* - \frac{2K}{3}x_2^{*^2} = 0,$$
$$-Kx_s^2 + 2A_{122}x_2^* - 2Kx_2^{*^2} > 0,$$

which yields an elliptic stagnation point on the x_2-axis, located at $x_2^* \in (0, (3/2)^{\frac{1}{2}}x_s)$ for $A_{122} \in ((8/3)^{\frac{1}{2}}Kx_s, \infty)$. As $A_{122} \to \infty$, the elliptic stagnation point approaches the wall, i.e., $x_2^* \to 0$, and the bubble shrinks closer to the wall. As $A_{122} \to (8/3)^{\frac{1}{2}}Kx_s$ from above, $x_2^* \to (3/2)^{\frac{1}{2}}x_s$ from below and the bubble grows in size. For $A_{122} < (8/3)^{\frac{1}{2}}Kx_s$, there are no stagnation points in the entire domain of the flow. We note that for $A_{122} \in ((8/3)^{\frac{1}{2}}Kx_s, \infty)$ there is also a hyperbolic stagnation point or saddle located at $(0, \bar{x}_2)$, and $\bar{x}_2 \in ((3/2)^{\frac{1}{2}}x_s, \infty)$; as $A_{122} \to \infty$, $\bar{x}_2 \to \infty$ and the separation between the two stagnation points is maximum, while as $A_{122} \to (8/3)^{\frac{1}{2}}Kx_s$ from above, $\bar{x}_2 \to (3/2)^{\frac{1}{2}}x_s$ from above, so that at $A_{122} = (8/3)^{\frac{1}{2}}Kx_s$ the hyperbolic and elliptic stagnation points coalesce, and disappear as A_{122} decreases below $(8/3)^{\frac{1}{2}}Kx_s$. At $A_{122} = 3Kx_s$, the elliptic stagnation point is located at $(0, 0.3625)$. The hyperbolic stagnation point or saddle is located at $(0, 4.1374)$. It is therefore sufficiently far away from the wall to have any bearing

on passive scalar transport close to the wall, and is ignored hereafter. With this choice of A_{122}, the time-independent velocity field is completely specified

$$\begin{aligned} u_1 &= -Kx_s^2x_2 + 3Kx_sx_2^2 + Kx_1^2x_2 - \frac{2}{3}Kx_2^3 + O(4), \\ u_2 &= -Kx_1x_2^2 + O(4), \end{aligned} \tag{2.6}$$

and is a low-order approximation of a steady two-dimensional separation bubble at a plane wall. By varying the coefficient A_{122}, the size of the steady separation bubble can be varied with important consequences on the associated advection-diffusion problem, and is the subject of §3.6. At present we continue with our choice of $A_{122} = 3Kx_s$. The streamlines (or pathlines) corresponding to the steady velocity field of (2.6) are shown in figure 2.1. From a dynamical systems viewpoint, the phase space of (2.6) has a heteroclinic connection ψ_h between the point of separation and the point of attachment, separating bounded and unbounded motion, where ψ_h is the value of the time-independent stream function (obtained below) on the separatrix. Introducing a time-periodic perturbation in (2.6) is expected to destroy this degenerate structure, giving rise to chaotic particle motion. An obvious way is to break the symmetry in the steady state. We let $A_{1122}(t) = K\beta\sin(\omega t)$. Continuity requires $A_{2222}(t) = -K\beta\sin(\omega t)$. The remaining coefficients are left unchanged. From (2.4), K remains independent of t and hence all remaining tensor coefficients are also time-independent. Nondimensionalising, $u_i \to u_iKx_s^3$, $x_i \to x_ix_s$, $t \to t/Kx_s^2$, $\omega \to \omega Kx_s^2$, the time-dependent velocity field becomes

$$\begin{aligned} u_1 &= -x_2 + 3x_2^2 + x_1^2x_2 - \frac{2}{3}x_2^3 + 3\beta x_1x_2^2\sin(\omega t) + O(4), \\ u_2 &= -x_1x_2^2 - \beta x_2^3\sin(\omega t) + O(4). \end{aligned} \tag{2.7}$$

The stream function ψ is easily obtained,

$$\psi(x_1, x_2, t) = -\frac{x_2^2}{2} + x_2^3 + \frac{x_1^2x_2^2}{2} - \frac{x_2^4}{6} + \beta x_1x_2^3\sin(\omega t) + O(5). \tag{2.8}$$

Truncated to third order, (2.7) can be expressed in the form

$$u(x,t) = f^u(x) + \beta g^u(x)\sin(\omega t), \tag{2.9}$$

where $f^u \equiv (f_1^u, f_2^u) = (-x_2 + 3x_2^2 + x_1^2 x_2 - \frac{2}{3}x_2^3,\ -x_1 x_2^2)$, $g^u \equiv (g_1^u, g_2^u) = (3x_1 x_2^2,\ -x_2^3)$, and β can be considered as the perturbation amplitude, while ω is the frequency of the perturbation.

2.2 The chaotic advection field

In the context of dynamical systems theory, the velocity field of (2.9) is a time-periodic perturbation of a planar Hamiltonian vector field, where the stream function of (2.8) plays the role of the Hamiltonian. The analysis of the global structure of the flow is most clearly carried out by studying the associated Poincaré map, which is the time-T map obtained by considering the discrete motion of points in time-intervals of one period T of the perturbation, and since the perturbation is also Hamiltonian the Poincaré map is area preserving. In this case one would expect Smale horseshoes, resonance bands and KAM tori to arise in the phase space of (2.9), which is also the physical space of the flow. The associated Poincaré map or time-T map, $T = 2\pi/\omega$, shows highly irregular motion in the bubble-region indicating chaotic particle trajectories: two Poincaré maps at two different values of the perturbation amplitude, $\beta = 0.6$ and 0.2, but perturbation frequency fixed at $\omega = 0.72$, are shown in figures 2.2(a) and (b) respectively. For the perturbation parameters considered here there are clearly no surviving KAM tori enclosing the core-region of the bubble, where "core-region" refers to the circulation region or region of closed streamlines in the steady, unperturbed bubble. Notice further that the surviving KAM islands occupy a small fraction of the bubble-region; indeed, none are detected in the Poincaré map for the case with $\beta = 0.6$ (figure 2.2a). For certain values of the perturbation parameters there are surviving KAM tori

enclosing the core-region of the bubble as well as island bands, and one such case will be considered in Chapter 3.

However, despite the numerical evidence in figures 2.2(a,b), the highly irregular particle motion does not amount to a mathematical proof of chaotic dynamics of the Smale-horseshoe type. Owing to the non-generic nature of the stagnation points on the no-slip boundary, a mathematical proof showing existence of chaotic dynamics seems difficult. From the dynamical systems viewpoint, our problem is non-generic because every point on the no-slip boundary is a non-hyperbolic stagnation point, despite the fact that it is a commonly encountered situation in fluid flows. Consequently, the mathematical theorems (see Wiggins 1990, 1992) proving existence of chaotic dynamics do not apply ; we will address these issues again in Chapter 5.

For the case of hyperbolic stagnation points the existence of stable and unstable manifolds is familiar, but the non-hyperbolic case requires special consideration. In the unperturbed ($\beta = 0$) integrable system, the bubble has a point of separation, denoted by p^-, a point of attachment, denoted by p^+, and a heteroclinic connection ψ_h between p^- and p^+. The points $p^+ \equiv (+1, 0)$ and $p^- \equiv (-1, 0)$, which are the points of zero shear-stress on the wall, are non-hyperbolic stagnation points. The standard scheme of introducing the phase of the periodic perturbation in (2.9) gives an autonomous vector field

$$\begin{aligned} \dot{x} &= f^u(x) + \beta g^u(x) \sin(\phi), \\ \dot{\phi} &= \omega, \end{aligned} \tag{2.10}$$

where the phase space of the autonomous system is now $\mathbb{R}^2 \times S^1$. For $\beta = 0$, when viewed in the three-dimensional phase space $\mathbb{R}^2 \times S^1$, p^+ and p^- become periodic orbits

$$\gamma^{\pm}(t) = (p^{\pm}, \phi(t) = \omega t), \tag{2.11}$$

with a two-dimensional stable and two-dimensional unstable manifold respectively, denoted by $W^s(\gamma^+(t))$ and $W^u(\gamma^-(t))$. Therefore, $W^s(\gamma^+(t))$ and $W^u(\gamma^-(t))$ coincide along a two-dimensional heteroclinic manifold, Γ_γ. We note that the invariant manifold theorem (see Theorem 4.1, Hirsch, Pugh & Shub 1977) for the persistence of normally hyperbolic invariant manifolds and the persistence and smoothness of their stable and unstable manifolds (at sufficiently small β) does not apply to $\gamma^\pm(t)$; in our problem, persistence of the invariant manifolds is decided by computation of the corresponding invariant manifolds of the associated Poincaré map, which we shall define momentarily. Assume for now that the periodic orbits $\gamma^\pm(t)$ of the suspended system (2.10) at $\beta = 0$, persist for $\beta \neq 0$. We denote the perturbed periodic orbits as $\gamma^\pm_\beta(t)$. It shall be seen in Appendix C that in fact $\gamma^\pm_\beta(t) = \gamma^\pm(t)$, and is closely related to the fact that the points of zero shear-stress on the wall remain fixed at $p^\pm$ at all times; it is easily verified from (2.9) that for $\beta \neq 0$, $p^\pm$ persist as the points of zero shear stress on the wall. Assuming $W^s(\gamma^+(t))$ and $W^u(\gamma^-(t))$ persist for $\beta \neq 0$, the stable and unstable manifolds of $\gamma^+_\beta(t)$ and $\gamma^-_\beta(t)$, denoted by $W^s(\gamma^+_\beta(t))$ and $W^u(\gamma^-_\beta(t))$ respectively, will generically not coincide. The Poincaré map is defined as a global cross-section in the usual way,

$$P^{\bar\phi}_\beta : \Sigma^{\bar\phi} \longrightarrow \Sigma^{\bar\phi},$$

$$(x_1(\bar\phi), x_2(\bar\phi)) \longmapsto (x_1(\bar\phi + 2\pi), x_2(\bar\phi + 2\pi)).$$

The intersection with $\Sigma^{\bar\phi}$ of the stable and unstable manifolds of $\gamma^+_\beta(t)$ and $\gamma^-_\beta(t)$ respectively are denoted as

$$W^s_\beta(\bar\phi) \equiv W^s(\gamma^+_\beta(t)) \cap \Sigma^{\bar\phi},$$

$$W^u_\beta(\bar\phi) \equiv W^u(\gamma^-_\beta(t)) \cap \Sigma^{\bar\phi}.$$

The unstable manifold of p^- for the Poincaré map corresponding to the cross-section $\bar\phi = 0$, $P_\beta \equiv P^{\bar\phi=0}_\beta$, denoted $W^u_\beta \equiv W^u_\beta(\bar\phi = 0)$, is computed for two different values of the perturbation amplitude, $\beta = 0.2,\ 0.6$, keeping the frequency

of the perturbation fixed at $\omega = 0.72$, and these are shown in figure 2.3(a) and (b) respectively.

In physical terms, the time-periodic perturbation in (2.9) that leads to bubble break-up and chaotic trajectories in the viscous boundary-layer can be attributed to an oscillatory outer inviscid flow. In particular, it should be noted that the chaotic advection field of (2.9) does not arise from any inherent oscillatory instability in the equations of motion at large Reynolds number but, instead, arises from an external forcing presumably caused by the outer inviscid flow. The Reynolds number, $Re = Kx_s^4/\nu$, for our boundary-layer flow is arbitrary, though it must be noted that the region of accuracy of the truncated series-solution shrinks as the Reynolds number is increased (Perry & Chong 1986a).

Finally, there are alternative schemes of introducing a time-periodic perturbation in (2.6) such that the time-dependent velocity field remains an asymptotically exact solution of the Navier-Stokes and continuity equations, and again gives rise to chaotic particle trajectories; there is of course no unique representation of a two-dimensional chaotic advection field adjacent to a no-slip boundary. However we shall show that the qualitative aspects of the associated passive scalar advection-diffusion problem depends primarily on certain generic structures in these chaotic advection fields, regardless of the specific form of the equations giving rise to the chaotic particle motion. Section 3.5 deals with this issue by considering an alternative local representation of a chaotic advection field.

2.3 The Melnikov function

Both, for the Poincaré maps displayed in figure 2.2 and the unstable manifolds displayed in figure 3.3, the frequency of the perturbation ω was chosen to be 0.72. This choice was based on the *Melnikov function* which gives some indication as to

the value of the perturbation frequency at which the chaotic particle motion can be expected to be the most widespread, albeit at small perturbation amplitudes. Melnikov's method is a global perturbation technique for showing the existence of transverse homoclinic/heteroclinic orbits arising from the transversal intersection of stable and unstable manifolds of certain normally hyperbolic invariant sets. The method was originally (Melnikov 1963) developed for time-periodic perturbations of an autonomous planar vector field having a homoclinic connection at a hyperbolic fixed point, in which case the existence of transverse homoclinic orbits implies the complicated dynamics associated with Smale horseshoes. We use Melnikov's method below to show transversal intersection of $W^s_\beta(\bar{\phi})$ and $W^u_\beta(\bar{\phi})$. However, in our case this does not prove the existence of chaotic dynamics of the Smale-horseshoe type owing both to the non-hyperbolicity of p^+ and p^-, as well as the invariance of the wall, the latter implying a non-transverse heteroclinic cycle. While the numerical evidence suggests this type of chaos exists in this situation, there are no mathematical theorems to this effect. For applications of the Melnikov function in studies of chaotic dynamics in similar situations, see Weiss & Knobloch (1989), Rom-Kedar, Leonard & Wiggins (1990), and Camassa & Wiggins (1991).

The Melnikov function is a signed measure of the distance between $W^s_\beta(\bar{\phi})$ and $W^u_\beta(\bar{\phi})$. Melnikov's theory, however, requires not only persistence but also smoothness of $W^s_\beta(\bar{\phi})$ and $W^u_\beta(\bar{\phi})$, for which we have no analytical verification. Assuming smoothness of $W^s_\beta(\bar{\phi})$ and $W^u_\beta(\bar{\phi})$, Melnikov's theory can be used to obtain the following Melnikov function for our problem,

$$M(\tau) = A(\omega)\sin(\omega\tau), \tag{2.12}$$

where τ parametrizes the heteroclinic connection ψ_h, and

$$A(\omega) = \int_{-\infty}^{+\infty} (f_1^u g_2^u - f_2^u g_1^u)(q^0(t))\cos(\omega t)dt, \tag{2.13}$$

where $f^u \equiv (f_1^u, f_2^u)$ and $g^u \equiv (g_1^u, g_2^u)$ are from the velocity field of (2.9), and $q^0(t)$ is the heteroclinic orbit. For $A(\omega) \neq 0$, it is a straightforward conclusion that W_β^s and W_β^u do intersect transversely (Wiggins 1990). Details of the derivation of $M(\tau)$ can be found in Appendix A. We do remark that the derivation of the Melnikov function requires careful consideration of *boundary-terms* that can arise due to the non-hyperbolicity of p^- and p^+ (e.g., see Camassa & Wiggins 1991). The variation of $A(\omega)$ with ω is shown in figure 2.4. We note that the perturbation frequency ω was chosen to be 0.72 in our computations since $A(\omega)$ is maximum at $\omega = 0.72$; it is desirable to have large $A(\omega)$ since the width of the chaotic layer increases with $A(\omega)$ (Ghosh, Chang & Sen 1992). Moreover, it is evident from figure 2.4 that the distance between the stable and unstable manifolds falls rapidly as ω is increased beyond 0.72 and for such ω, $W_\beta^s(\bar{\phi})$ and $W_\beta^u(\bar{\phi})$ do not sweep out the entire bubble-region for any given cross-section $\bar{\phi}$. This is certainly true for $\omega = 2.0$, which will be our choice of the perturbation frequency to study the case with surviving KAM tori enclosing the core-region of the bubble.

FIGURES

Figure 2.1: Streamlines for the steady two-dimensional separation bubble at a plane wall, obtained using (2.6).

Figure 2.2: Poincaré map P_β for the advection field of (2.9) at $\omega = 0.72$ and (a) $\beta = 0.6$, (b) $\beta = 0.2$.

Figure 2.3: The unstable manifold W^u_β at $\omega = 0.72$ and (a) $\beta = 0.6$, (b) $\beta = 0.2$.

Figure 2.4: Variation of amplitude A of the Melnikov function with perturbation frequency ω.

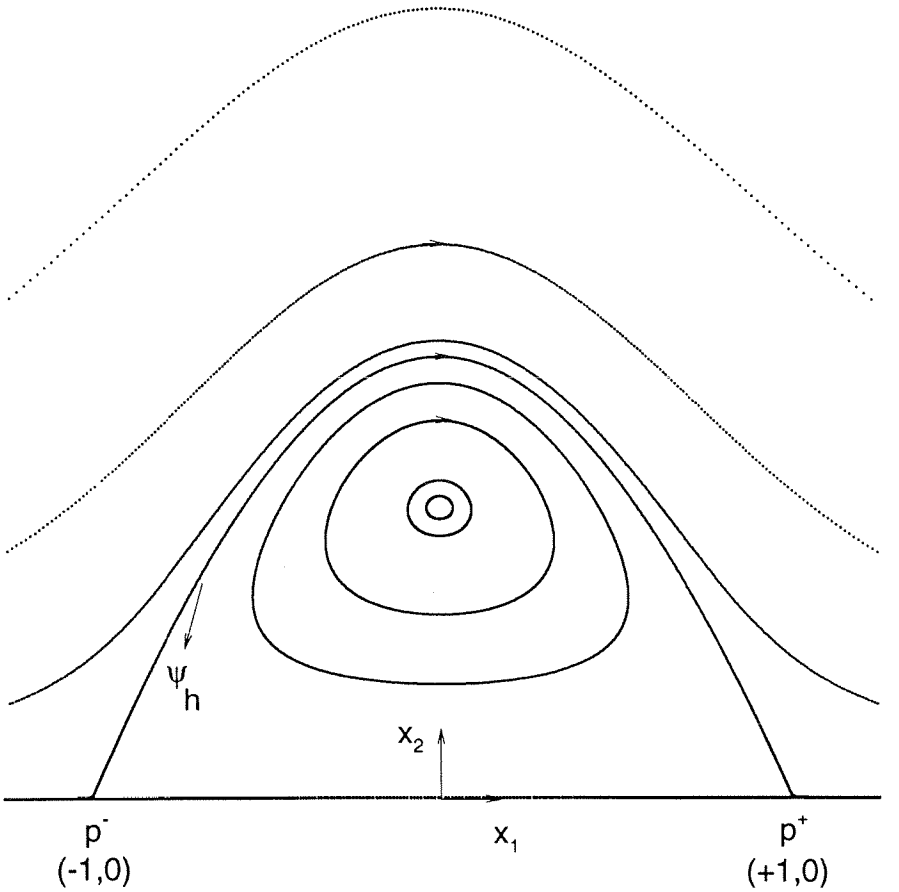

Figure 2.1

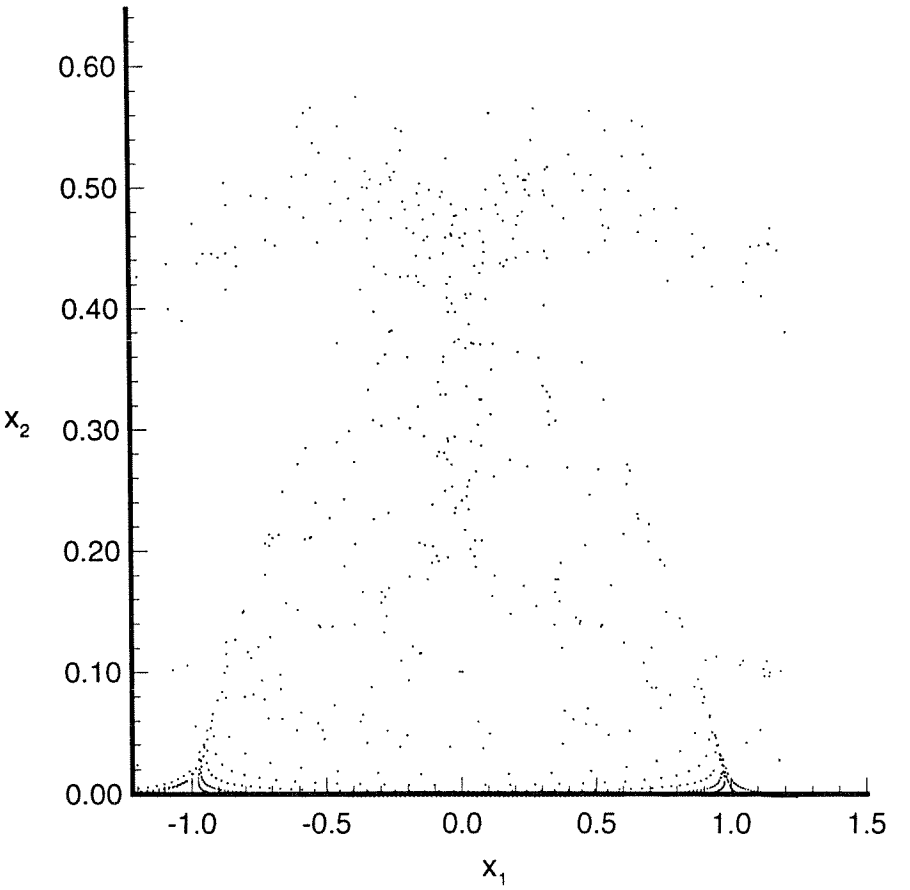

Figure 2.2(a)

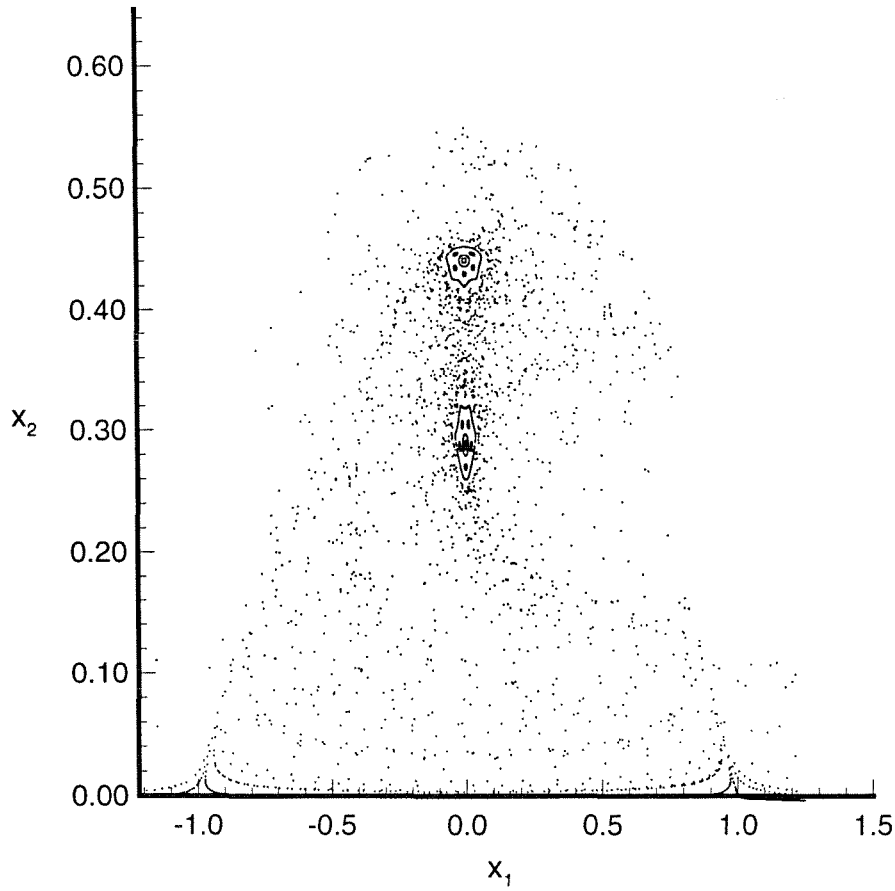

Figure 2.2(b)

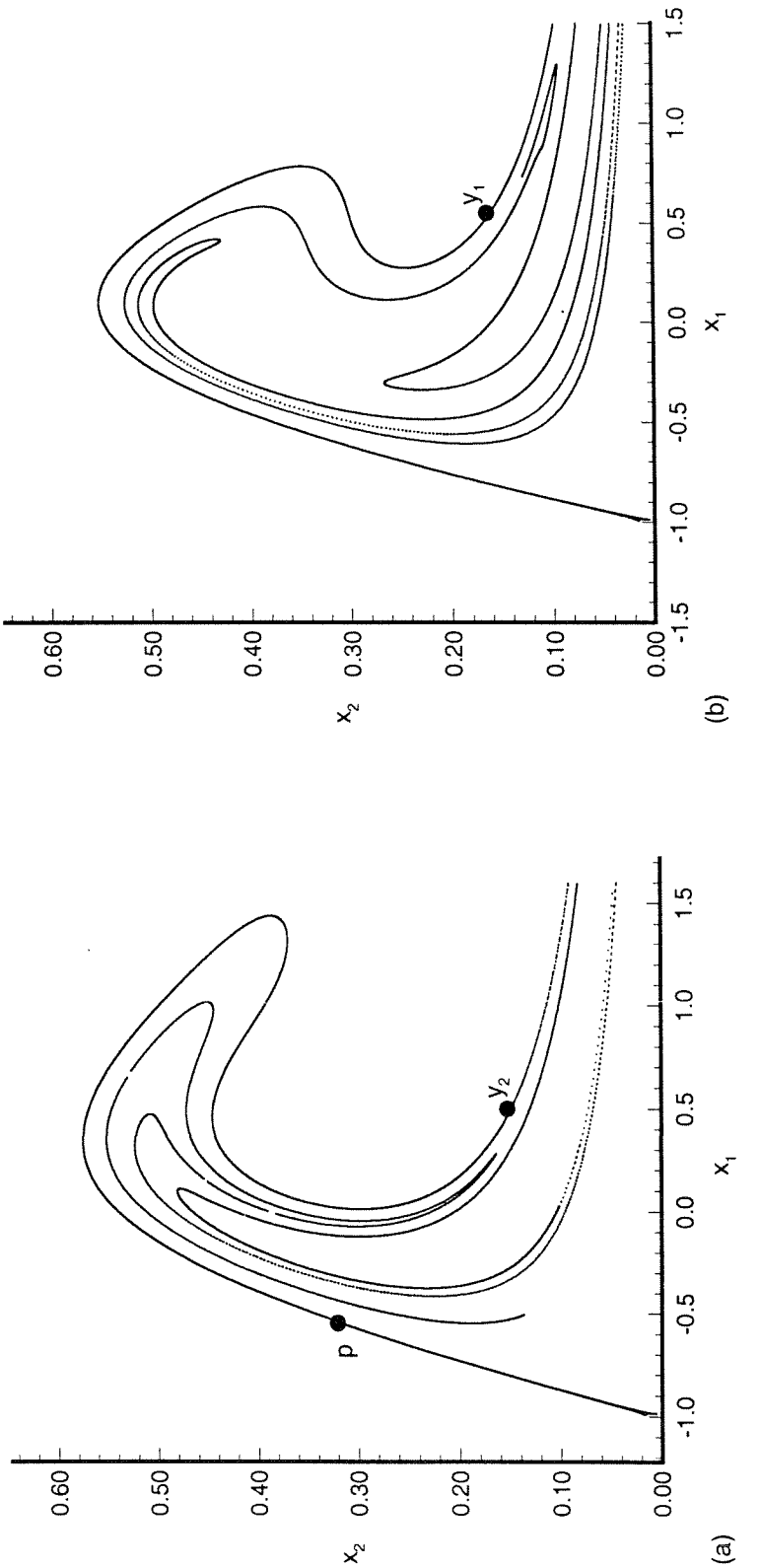
0.60
0.50
0.40
0.30
0.20
0.10
0.00
x_2
-1.5
-1.0
-0.5
0.0
0.5
1.0
1.5
x_1
y_1
(b)
0.60
0.50
0.40
0.30
0.20
0.10
0.00
x_2
-1.0
-0.5
0.0
0.5
1.0
1.5
x_1
p
y_2
(a)

Figure 2.3

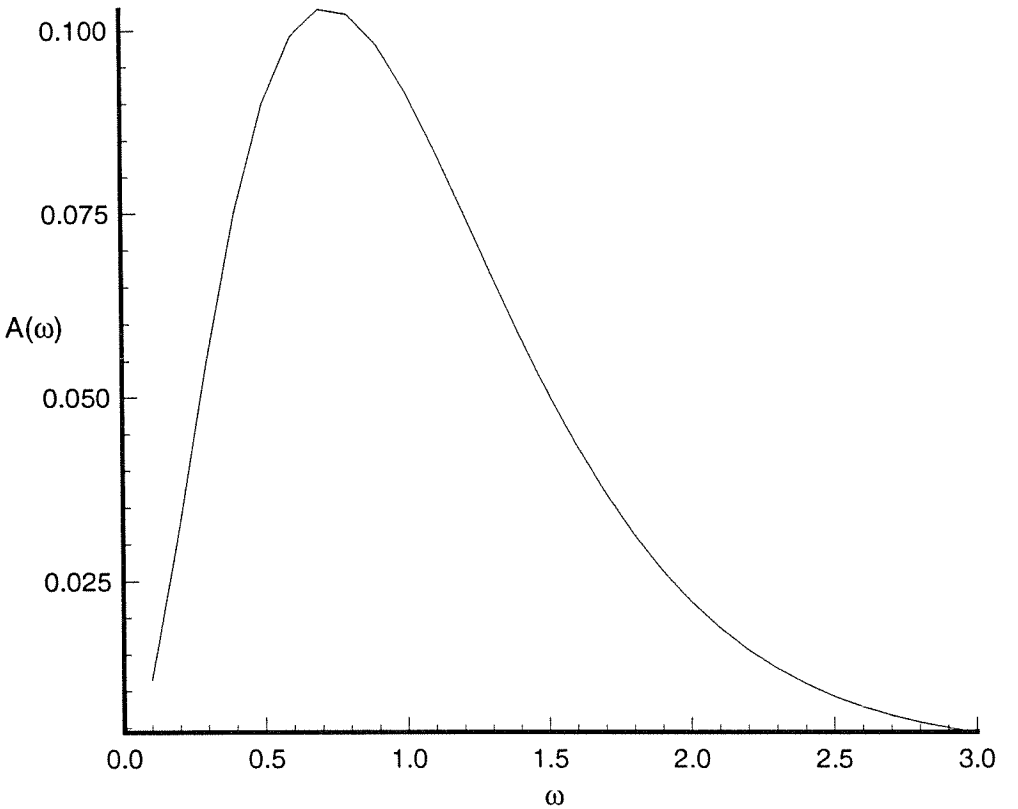

Figure 2.4

Chapter 3

Advection-diffusion of a passive scalar at small diffusivity or large Peclet number

A localized portion of the plane no-slip boundary is considered as an active surface. In the case of heat transfer, the active surface can be considered as a local "hot spot" at the wall and is modeled as a local step change in temperature with the step placed symmetrically about the unperturbed bubble. At time $t = 0$ the temperature has a dimensionless value of unity at the wall over the dimensionless interval $x_1 \in [-1.5, 1.5]$ and is zero everywhere else on the wall and in the fluid. The temperature distribution at the wall is maintained externally and serves as a time-independent boundary condition as heat diffuses from the wall and into the fluid. Non-dimensionalising time t using the advection time-scale $1/Kx_s^2$ gives the familiar evolution equation for the advection-diffusion of a scalar field $\theta(x,t)$, which can be considered as temperature,

$$\frac{\partial \theta}{\partial t} + u \cdot \nabla \theta = \frac{1}{Pe} \nabla^2 \theta, \tag{3.1}$$

where the Peclet number $Pe = Kx_s^4/D$, with D the scalar diffusivity. The advecting two-dimensional velocity field $u(x,t)$ is given by (2.9). The following initial and

boundary conditions

$$\theta(x_1, x_2 > 0, t = 0) = 0,$$

$$\theta(x_1, x_2 = 0, t) = 1 - H(|x_1| - 1.5),$$

$$\theta(|x_1| \to \infty, x_2 > 0, t) = 0,$$

$$\theta(x_1, x_2 \to \infty, t) = 0,$$

with $(x_1, x_2) \in \mathbb{R}^1 \times \mathbb{R}^1$, completely specifies the advection-diffusion problem. $H(\cdot)$ is the Heaviside step function. In the absence of scalar diffusion the deterministic Lagrangian motion of a passive scalar is described by the velocity field. Two-dimensional time-periodic flows have been studied extensively using a dynamical systems approach (e.g., see Wiggins 1992) and the geometrical structures that arise naturally in the domain of the flow, such as invariant manifolds, homoclinic/heteroclinic tangles, invariant hyperbolic sets and KAM tori are well known. However, it is still far from clear how these structures influence the transport and distribution of a passive scalar in the presence of scalar diffusion. Our model problem provides a convenient framework for understanding some of the transport issues that arise naturally in such flows. The domain of interest is the flow region immediately above the active portion of the wall and since we will be making frequent reference to this region, we loosely term it as the "bubble-region."

Rom-Kedar *et al.* (1990) considered the transport of a passive scalar in the absence of scalar diffusion in a similar problem and found the unstable manifold, i.e., $W^u_\beta(\bar{\phi})$, as the dominant organizing structure. They considered the evolution of an arbitrary blob of fluid under several iterations of the Poincaré map and showed that the unstable manifold behaves in some sense as an attractor since neighborhoods of $W^u_\beta(\bar{\phi})$ are stretched along $W^u_\beta(\bar{\phi})$ and flattened in a complementary direction under forward iterations of $P^{\bar{\phi}}_\beta$. Of course, because of the area preserving property of $P^{\bar{\phi}}_\beta$ that derives from the incompressibility of the fluid, $W^u_\beta(\bar{\phi})$ is not an attractor in the

usual sense. *Our main goal in this section is to motivate the following : for scalar transport with small scalar diffusivity, the unstable manifold $W^u_\beta(\bar{\phi})$ continues to be the organizing structure in the distribution of the scalar field and the time evolution of the scalar field for the $\beta \neq 0$ case can be understood in terms of the structure of $W^u_\beta(\bar{\phi})$.* Additionally, there are other important considerations, some of which have been outlined in the Introduction : for example the role of hyperbolicity and the strong stretching and folding properties characteristic of chaotic flows, the role of non-hyperbolicity at the wall, the asymptotic state of the scalar distribution, etc., and to what extent they contribute to our understanding of the advection-diffusion process and its interplay with the geometrical structures in the flow. As a first step towards investigating these issues, finite-time distributions of the scalar field are obtained by solving (3.1) numerically. We confine our attention entirely to the case of small scalar diffusivity, or large Peclet number; large scalar diffusivity would result in a diffusively dominant advection-diffusion process, in which case the role of the geometrical structures in the flow can be expected to be less prominent.

3.1 A random-walk scheme for solving the advection-diffusion equation

The singular limit of large Peclet number is not easily tackled by any numerical scheme that embraces the Eulerian approach and tries to solve the partial differential equation of (3.1) directly. At large Pe, a thermal boundary-layer will form in the vicinity of the active surface of thickness proportional to $Pe^{-1/3}$ (see §3.4), which places severe constraints on the spatial resolution obtainable in the boundary-layer in a finite-difference solution of (3.1) at large Pe. In contrast, a random-walk solution uses a Lagrangian approach based on the stochastic differential corresponding to the scalar advection-diffusion equation. Saffman (1959) used

a random-walk approach to study the effects of molecular diffusion on the transport of a passive scalar in flow through porous media. Chorin (1973) extended the random-walk approach to numerical solutions of the vorticity diffusion equation corresponding to the Navier-Stokes equations for incompressible flow in two space dimensions at large Reynolds numbers, where the problem is complicated by the fact that the vorticity is not a passive scalar. Since we require solutions to (3.1) at Peclet numbers so large that finite-difference methods are difficult to apply, a random-walk or Brownian motion scheme is developed below for solving the scalar advection-diffusion problem.

The active boundary is imagined to be a constant temperature bath. The physical process of diffusion of passive scalar from the active portion of the plane boundary into the flow is imitated by numerically simulating a constant temperature bath. The bath has width identical to the extent of the active surface and depth chosen according to the Peclet number. At $t = 0$, N points are randomly distributed in the bath at locations $r_i^0 = (x_{1i}^0, x_{2i}^0)$, $i = 1, ..., N$, N large, each of mass $1/N_d$ where $N_d = N/A_{bath}$ is the number density of the randomly distributed points, and A_{bath} is the area of the constant temperature bath. The evolution of temperature in the bath is governed by the simple transient diffusion equation

$$\frac{\partial \theta}{\partial t} = \frac{1}{Pe} \nabla^2 \theta, \tag{3.2}$$

with initial data $\theta(x, t = 0) = 1$ and adiabatic boundary conditions, which of course has solution $\theta(x, t) = 1$. The probabilistic interpretation of the transient diffusion equation with given initial data is well known (Chandrasekhar 1943). For a brief survey with view to applications in numerical schemes based on random-walk methods, see Chorin & Marsden (1979). The stochastic differential corresponding to (3.2) is simply

$$dx = (2/Pe)^{1/2} dW_t,$$

where W_t is a two-dimensional Wiener process (Arnold 1974). Hence, in every time-step Δt, the points may be advanced according to

$$x_{1_i}^{n+1} = x_{1_i}^{n} + \eta, \; x_{2_i}^{n+1} = x_{2_i}^{n} + \xi, \; n = 0, 1, \ldots \; ,$$

where η, ξ are Gaussianly distributed random variables, each with mean zero and variance $2\Delta t/Pe$, and $x_{1_i}^{n} \equiv x_{1\,i}(n\Delta t)$, $x_{2_i}^{n} \equiv x_{2\,i}(n\Delta t)$. Except for the boundary that coincides with the wall, the remaining three boundaries of the constant temperature bath behave as adiabatic surfaces and are therefore treated as perfectly reflecting boundaries (Chandrasekhar 1943). As for the wall, when a point jumps across the wall and into the domain of the flow, a new point of identical mass is created at the reflection point inside the bath. To ensure that the reflection point is almost always – i.e., with probability arbitrarily close to unity – inside the bath, it is sufficient to choose the depth of the bath as 10σ where σ is the standard deviation of the Gaussian "jumps." In every time-step, a constant number density N_d of randomly distributed points of masses $1/N_d$ is maintained inside the bath and it therefore simulates a constant temperature bath. Points that jump across the wall, from the bath and into the domain of the flow, have trajectories generated by the stochastic differential corresponding to (3.1)

$$dx = u dt + (2/Pe)^{1/2} dW_t. \tag{3.3}$$

A point in the domain of the flow , i.e., at location $r^0 = (x_1^0, x_2^0)$ with $x_2^0 > 0$, is therefore advanced according to

$$x_1^{n+1} = x_1^n + \Delta x_1^n + \eta, \; x_2^{n+1} = x_2^n + \Delta x_2^n + \xi, \tag{3.4}$$

where

$$x_1^n = x_1(n\Delta t), \; x_2^n = x_2(n\Delta t), \; \Delta x_1^n = \int_{n\Delta t}^{(n+1)\Delta t} u_1 dt, \; \Delta x_2^n = \int_{n\Delta t}^{(n+1)\Delta t} u_2 dt,$$

and η, ξ are Gaussianly distributed random variables as before; the velocity field is integrated using fourth-order Runge-Kutta. The Gaussianly distributed random variables η and ξ are obtained from uniformly distributed computer-generated pseudo-random numbers using standard algorithms based on the Box-Mueller transformation (e.g., see Press *et al.* 1986). The increment $(\Delta x_1^n, \Delta x_2^n)$ is the deterministic jump in a time-step Δt arising from the continuum velocity of a fluid particle, while (η, ξ) is a random component describing the Brownian motion of the molecules. For the advection-diffusion process in the domain of the flow, the wall specifies a constant temperature boundary condition and can therefore be treated as a perfectly absorbing boundary (Chandrasekhar 1943). Hence, trajectories generated by (3.3) that cross the wall, which is signalled by $x_2^n \leq 0$, are terminated. After n steps, the expected distribution of mass on the upper half-plane, $x_2 > 0$, gives the temperature field at time $t = n\Delta t$. Therefore the temperature at time t at a point (x_1, x_2), $x_2 > 0$, is given by

$$\theta(x_1, x_2, t) = \lim_{N \to \infty} \frac{\text{number of points contained in } I_1(x_1) \times I_2(x_2) \text{ at time } t}{N_d A_{box}}, \tag{3.5}$$

where $I_1(x_1) = [x_1 - \frac{\Delta x_1}{2}, x_1 + \frac{\Delta x_1}{2}]$, $I_2(x_2) = [x_2 - \frac{\Delta x_2}{2}, x_2 + \frac{\Delta x_2}{2}]$, $I_1(x_1) \times I_2(x_2)$ is the Cartesian product of the two closed intervals, and $A_{box} = \Delta x_1 \Delta x_2$. The flux across the wall, integrated over the active portion of the wall, is given by the expected rate at which points cross the active portion of the wall (Chandrasekhar 1943). The wall-integrated flux J_w at time $t = n\Delta t$ is simply

$$J_w(t) = \lim_{N \to \infty} \frac{\Delta N(n)}{N_d \Delta t},$$

where $\Delta N(n)$ is the net number of points crossing the active portion of the wall at the n^{th} time-step. Therefore $\Delta N(n)$ is the number of points that jump from the bath and into the flow at the n^{th} time-step minus the number of points in the

domain of the flow that jump across the active surface at the n^{th} time-step and are terminated. We compute the wall-integrated flux averaged over time $T = 2k\Delta t$, which is given by

$$< J_w(t) >_T = \lim_{N\to\infty} \frac{\Delta N(n,k)}{N_d(2k\Delta t)},$$

where $\Delta N(n,k)$ is the net number of points crossing the active surface in $2k$ time-steps, from time $(n-k)\Delta t$ to $(n+k)\Delta t$. Therefore $< J_w(t) >_T$ is in fact:

$$< J_w(t) >_T = \frac{1}{T}\int_{t-\frac{T}{2}}^{t+\frac{T}{2}} \left(\int_{x_1=-1.5}^{x_1=1.5} - \frac{1}{Pe}\frac{\partial\theta}{\partial x_2}(x_1,x_2,s)\Big|_{x_2=0} dx_1 \right) ds.$$

Error estimates, obtained in Appendix B, show the error in the computed scalar field $\theta(x_1,x_2,t)$ is $O((N_d A_{box})^{-1/2})$. The consequent slow convergence, which is typical of random-walk methods, requires that N be very large especially when high spatial resolution, i.e., small $\Delta x_1 \Delta x_2$ or small A_{box}, is desired. In our computations N is $O(10^6)$. However, it is not hard to realize that the random-walk scheme described above is ideally suited for parallel computation and an implementation of the method on a parallel computer like the 512 node Intel Touchstone Delta reduces computation time by several orders of magnitude. In fact, our code can use any number of compute nodes and proceeds in parallel by distributing N equally among the number of available nodes, with an absolute minimum of node interactions. We note that there are alternative random-walk schemes that can be formulated for our advection-diffusion problem, but these were discarded in favour of the scheme described above on account of the ease with which the computations can be rendered parallel.

The random-walk algorithm for whole field computations is tested on a simple heat conduction problem for which there is an analytical solution for the temperature field. The test problem considered is that of heat conduction from a constant temperature boundary into a one-dimensional semi-infinite rod. The test problem

is of course much less complicated than the advection-diffusion problem to which we will eventually apply the random-walk algorithm; firstly, the conduction problem is one-dimensional, and secondly, there is no advection. However, the simple test problem considered here provides an easy verification of the random-walk scheme developed above to deal with the problem of diffusion of heat from a constant temperature boundary into an unbounded medium; in particular, it verifies the scheme of treating a constant temperature boundary as a heat bath populated with a large number of randomly located points with constant number-density. Heat conduction in a one-dimensional semi-infinite rod with one-dimensional coordinate $z \in [0, \infty)$, initial dimensionless temperature $\theta(z, t = 0)$ of unity at $z = 0$, $\theta(0, t = 0) = 1$, and zero elsewhere, $\theta(z > 0, t = 0) = 0$, and time-independent boundary conditions, $\theta(0, t) = 1$ and $\theta(\infty, t) = 0$, has the following well-known (Carslaw & Jaeger 1959) error-function solution:

$$\theta(z,t) = erfc\left(\frac{z}{2\sqrt{Dt}}\right) \equiv 1 - \frac{2}{\sqrt{\pi}} \int_0^{z/2\sqrt{Dt}} e^{-s^2} ds, \tag{3.6}$$

where D is the conductivity of the semi-infinite solid. In figure 3.1, the temperature field obtained from a whole-field-random-walk computation, for $D = 0.001$ and at time $t = 5$, is compared against the analytical solution of above. The match is evidently satisfactory. The instantaneous flux of heat at the boundary $z = 0$ is given by the following analytical solution

$$J_w(t) \equiv -D \frac{\partial \theta}{\partial z}\bigg|_{z=0} = \left(\frac{D}{\pi t}\right)^{1/2}, \tag{3.7}$$

which is compared against flux computations from the random-walk algorithm, evaluated at several times (see figure 3.2), and the match between the analytical and numerical result is again satisfactory.

3.2 The Wiener bundle method

The results obtained using the random-walk method of above were verified by comparing the solution of the scalar field at several points in the domain of interest against point values computed using an independent numerical scheme also based on the theory of Brownian motion, called the Wiener bundle method. The method has been used previously to study heat conduction problems (Haji-Sheikh & Sparrow 1967), to treat the advection-diffusion of magnetic field in magneto-hydrodynamics (Molchanov, Ruzmaikin & Sokolov 1985, Klapper 1992b), and in the study of chaotic advection of scalars (Klapper 1992a). While the Wiener bundle method is generally inefficient for whole field computations, it has the unique advantage of allowing calculation of the scalar value at a single point without calculating the whole field. Therefore, when only a few point values are desired the method offers a distinct advantage over other numerical schemes. The Wiener bundle method will also be used in Chapter 5 to gain useful insights into the the small diffusivity scalar advection-diffusion problem, and we therefore outline it briefly. The method is also called a pseudo-Lagrangian method since it is a generalization of the Lagrangian solution for zero diffusivity. At $Pe = \infty$, i.e., for the case of zero-diffusivity, (3.1) is solved by considering θ as constant along pathlines in the flow. Hence $\theta(x(x^0,t),t) = \theta(x^0,t_0)$, $t > t_0$, where $x(x^0,t)$ is the Lagrangian variable defined by $dx = udt$, $x(x^0,t_0) = x^0$. The zero-diffusivity Lagrangian solution can be generalized to the case of non-zero diffusivity, i.e., finite Pe, by averaging over a bundle of random (Wiener) trajectories. A Wiener trajectory is generated using the stochastic differential of (3.3). Therefore, starting at a point x at time t and integrating backwards in time using (3.3) yields a "bundle" of Wiener trajectories, each of which starts from a random point x^0 at initial time t_0 and reaches x at time t. Each Wiener trajectory "carries" with it the scalar value θ of the point

from which it originates, just as in the zero-diffusivity Lagrangian solution, and an expectation taken over the bundle of Wiener trajectories determines $\theta(x,t)$. The Wiener bundle solution of (3.1) is given by

$$\theta(x,t) = < \theta(x^0, t_0) >, \tag{3.8}$$

where the average is taken over all Wiener trajectories starting at a random point x^0 and ending at a given non-random point x in time $t - t_0$. It is easy to verify that (3.8) is indeed a solution of (3.1). We give a non-rigorous argument: since a diffusion process is Markovian,

$$\theta(x, t + \Delta t) =< \theta(x^0(t), t) >_{x^0(t)},$$

where $x^0(t) = x - (u\Delta t + (2/Pe)^{1/2}\Delta W_t)$. Therefore, expanding about x,

$$\begin{aligned}
\theta(x, t + \Delta t) &= \Big\langle \theta(x,t) + \frac{\partial \theta}{\partial x_i}(x^0(t) - x)_i \\
&\quad + \frac{1}{2}\frac{\partial^2 \theta}{\partial x_i \partial x_j}(x^0(t) - x)_i (x^0(t) - x)_j + O(3) \Big\rangle, \\
&= \Big\langle \theta(x,t) - \frac{\partial \theta}{\partial x_i}(u_i \Delta t + (2/Pe)^{1/2}\Delta W_{t_i}) \\
&\quad + \frac{1}{2}\frac{\partial^2 \theta}{\partial x_i \partial x_j}(u_i \Delta t + (2/Pe)^{1/2}\Delta W_{t_i})(u_j \Delta t + (2/Pe)^{1/2}\Delta W_{t_j}) \\
&\quad + O(3) \Big\rangle, \\
&= \theta(x,t) - \frac{\partial \theta}{\partial x_i} u_i \Delta t + \frac{1}{Pe}\frac{\partial^2 \theta}{\partial x_i \partial x_j}\delta_{ij}\Delta t + O(\Delta t^2),
\end{aligned}$$

where use was made of the fact that W_t is a standard two-dimensional Wiener process with Gaussianly distributed increments satisfying $< \Delta W_t >= 0$ and $< \Delta W_{t_i} \Delta W_{t_j} >= \delta_{ij}\Delta t$. Dividing by Δt and taking the limit as $\Delta t \to 0$ yields (3.1). For a rigorous proof, see McKean (1969).

3.3 Scalar distributions - numerical simulation results

Finite-time distributions of the scalar field at $Pe = 2.5 \times 10^4$ are obtained numerically on the 512 node Intel Delta using the random-walk method for whole field computations described earlier. The scalar field is computed at several times that are integral multiples of the perturbation period at again $\beta = 0.2,\ 0.6$, and these are displayed in figures 3.3(a-d), 3.4(a-d). The time-evolution of the scalar field is also obtained for $\beta = 0$, i.e., for the steady bubble, at the same Pe for the sake of comparison and is shown in figure 3.5(a-d). For the steady bubble the asymptotic or long-time scalar field distribution is expected to be uniform in the circulation or core-region of the bubble (Batchelor 1956, Pan & Acrivos 1968), while there will be boundary-layers along the wall and straddling the separatrix, ψ_h. The diffusive time-scale, being of the order of the Peclet number, is very large and since the asymptotic distribution is attained over the diffusion time-scale (Rhines & Young 1983) it would take a prohibitively long-time computation to reproduce the expected asymptotic distribution. However, it is clear from figure 3.5(a-d) that the distribution of the scalar field for the case of steady ($\beta = 0$) advection is tending to the expected asymptotic distribution as t increases. Comparing figures 3.3, 3.4 with figure 3.5, it is clearly evident that the evolution of the scalar field for the $\beta \neq 0$ case is markedly different from the $\beta = 0$ case. Comparisons of figure 3.3(a-d) with figure 2.3(a), and figure 3.4(a-d) with figure 2.3(b) shows the dominating role of W^u_β in the time-evolution of the scalar field. We note that for the parameter values considered here the size of KAM islands is negligible and, as far as the distribution of the scalar field is concerned, $W^u_\beta(\bar{\phi})$ is the main organizing structure over the entire domain of the flow with the exception of a narrow near-wall boundary-layer, as is evident from figures 3.3, 3.4. Notice further that the distribution of the scalar field is more uniform and widespread for the near-integrable system (figure 3.4) in contrast to

the case with larger β (figure 3.3). Comparing figure 3.3 with figure 3.4, it is also evident that at larger β an asymptotic distribution is attained in shorter time. To further pursue this point, the perturbation amplitude in the chaotic advection field is pushed higher to $\beta = 0.8$ while retaining $\omega = 0.72$, and the scalar field is displayed in figure 3.6(a-d). The scalar field is almost entirely localized around the unstable manifold of p^- and an asymptotic distribution is attained in even shorter time. Final confirmation of these features is obtained from scalar distributions at $\beta = 1.0$ (ω and Pe unchanged), displayed in figure 3.7(a-d). We make a few remarks: chaotic advection is usually associated with improved stirring (Aref 1984, Khakhar & Ottino 1986) and, consequently, improved mixing (Jones 1991). For chaotic advection in bounded domains this results in rapid homogenization of the scalar field, irrespective of the initial distribution; the asymptotic distribution is uniform and the time-scale for homogenization goes as the logarithm (Jones 1991) of the Peclet number, in contrast to the case when particle trajectories are regular and the time-scale of homogenization is linear (Rhines & Young 1983) in Pe. However, because of the unbounded nature of the flow being considered here, the scalar distribution of course never attains a homogenized state. Indeed, as the chaotic particle motion becomes more widespread (i.e., at larger β) the scalar distribution becomes more localized and non-uniform. Therefore, while the time-scale of homogenization is a useful measure of efficiency of mixing in bounded domains, in unbounded flows there is no analogous physical basis for defining an efficiency of mixing. Below is considered the case with surviving KAM tori enclosing the core-region of the bubble.

Increasing the frequency ω of the perturbation dramatically changes the structure of the unstable manifold W^u_β, which now does not sweep out the entire bubble-region. Appearing in the core-region of the bubble are KAM tori and island bands which are impenetrable by the unstable manifold, and W^u_β is no longer the dominant

organizing structure in the time-evolution of the scalar field, though it does influence the scalar distribution in regions swept by W^u_β. In figure 3.8, a Poincaré map of the time-periodic chaotic advection field is obtained at $\beta = 0.2$, $\omega = 2.0$, showing the structure of the KAM tori and island bands. In figure 3.9, the scalar field is computed at $\beta = 0.2$ and perturbation frequency increased to $\omega = 2.0$, while Pe is again taken to be 2.5×10^4; to compare with previous results, the time-dependent distribution is obtained at the same times as before. Notice that the scalar field is no longer evaluated at times that are integral multiples of the perturbation period *corresponding* to $\omega = 2.0$, and therefore the t's in figure 3.9 correspond to *different* cross-sections $\bar{\phi}$; as $\bar{\phi}$ changes, so does the geometrical structure of $W^u_\beta(\bar{\phi})$, which in turn influences the distribution of the passive scalar in regions swept by $W^u_\beta(\bar{\phi})$. In figure 3.10(a,b) the unstable manifold $W^u_\beta(\bar{\phi})$ is computed at $\beta = 0.2$, $\omega = 2.0$ and cross-sections $\bar{\phi}$ corresponding to the t's in figure 3.9. Comparing figure 3.10(a,b) with figure 3.9(a,b) shows how the dependence of the unstable manifold $W^u_\beta(\bar{\phi})$ on the cross-section $\bar{\phi}$ of the Poincaré map $P^{\bar{\phi}}_\beta$ is manifested in the scalar distribution. Notice that for both values of $\bar{\phi}$ considered in figure 3.10, $W^u_\beta(\bar{\phi})$ does not sweep out the core-region of the bubble, and in this region the evolution of the scalar field is influenced by the surviving KAM tori evident in figure 3.8. Further, in the core-region of the bubble the KAM tori play a role not unlike closed streamlines in the steady bubble as transport across a KAM torus is possible by scalar diffusion only, and the time-evolution of the scalar field in this core-region resembles closely that in the steady-bubble-case. Nothing can be said though about the nature of the asymptotic distribution in this case.

We conclude this section with a verification of the results obtained from the whole field computations, using the Wiener bundle method. Centerline profiles of the scalar field along $(x_1 = 0, x_2 > 0)$ were extracted from figure 3.3(a,d), and

these are plotted as solid lines in figure 3.11. Point values of the scalar field were obtained at the same t's using the Wiener bundle method and these are also displayed in figure 3.11. The scalar value at a point on the centerline is obtained by integrating backwards in time a collection N of "particles" that are located at the given $x \equiv (x_1 = 0, x_2 > 0)$ at time t, using the stochastic differential of (3.3). As was mentioned earlier, the wall can be treated as a perfectly absorbing boundary for a Brownian particle and Wiener trajectories are terminated on reaching the wall in backward time. The scalar value $\theta(x,t)$ at $x \equiv (x_1, x_2 > 0)$ at time t is given by

$$\theta = \frac{1}{N} \sum_{i=1}^{N} \delta_{wi}, \tag{3.9}$$

where $\delta_{wi} = 1$ if the i^{th} particle reaches the active portion of the wall before time t, and $\delta_{wi} = 0$ otherwise. Equation (3.9) is therefore an expectation over the scalar values "carried" by the Wiener trajectories that arrive at the point x in time t. Error estimates, obtained in Appendix B, show the error is $O(N^{-1/2})$; N was taken to be 2×10^4 in our computations. From figure 3.11 it is evident that the match between the results obtained using the two independent random-walk schemes is quite satisfactory.

3.4. Flux of passive scalar from the local active surface into the thermal boundary-layer

The flux at the wall, integrated over the active portion of the wall and averaged over time $T = 2\pi/\omega$, is evaluated at every $t = m\frac{T}{2}$, m an odd integer, for β's equal to 0, 0.2, and 0.6, and $\omega = 0.72$, and the results are displayed in figure 3.12(a). It is evident that the time-averaged wall-integrated flux approaches an asymptotic value over a time-scale that appears to be unrelated to the time-scales over which the scalar field attains an asymptotic distribution away from the wall.

Moreover, the chaotic particle motion increases the asymptotic flux at the wall only marginally over the steady-advection-case ($\beta = 0$). The asymptotic value of the time-averaged wall-integrated flux is evaluated at several perturbation amplitudes, β ranging from zero to unity (keeping ω and Pe fixed), and these are displayed in figure 3.12(b). It is clear that there is little or no enhancement over the $\beta = 0$ case. Both observations are closely related to the fact that the dynamics of particle motion in a near-wall region as well as the boundary-layer distribution of the scalar field are largely insensitive to the chaotic advection-diffusion process away from the wall. It is also observed that the asymptotic value of $< J_w(t) >_T$ appears to be independent of the averaging period T, though averaging over shorter times does increase the scatter in the data, which is only to be expected in a random-walk computation.

These observations can be explained by considering the relative contributions of the various terms in the advection-diffusion equation of (3.1) in the near-wall thermal boundary-layer, once the initial transients have died down and the scalar field has settled into an asymptotic state. With the exception of a small neighborhood of the separation point p^-, $x_1 = O(1)$ and $x_2 < O(1)$ in the near-wall thermal boundary-layer. Substituting (2.9) in (3.1), it is easily determined that the advective contribution $u \cdot \nabla\theta$ to (3.1) in this region is to dominant order $O(x_2)$, while the diffusive contribution $(1/Pe)\nabla^2\theta$ is to dominant order from diffusion transverse to the wall and is $O(Pe^{-1}x_2^{-2})$. Further, time-series obtained at a point in this region using the Wiener bundle method, displayed in figure 3.13(a), indicates that the scalar value has very small time-dependent fluctuations about the asymptotic mean value. It is then reasonable to expect that the advective and diffusive contributions to (3.1) are in balance; this immediately implies that the scalar field in the

near-wall thermal boundary-layer (away from p^-) is of the form

$$\theta(x_1, x_2, t) = \theta_0(x_1, x_2) + \bar{\epsilon}\theta_1(x_1, x_2, t) + \cdots, \tag{3.10}$$

where $\bar{\epsilon} << 1$, i.e., θ is time-independent to dominant order. This is in agreement with figure 3.13(a), where the fluctuations are now interpreted as a second-order effect, i.e., they are $O(\bar{\epsilon})$. We note that the small parameter $\bar{\epsilon}$ need not scale with the Peclet number; indeed, the size of the fluctuations about the asymptotic mean value shows little variation with Pe. How $\bar{\epsilon}$ scales with the perturbation parameters β and ω remains an unresolved question. We mention in passing that the dominant balance argument of course does not apply away from the wall and the asymptotic scalar distribution is not necessarily time-independent, even to dominant order. Time-series obtained at a point in the bubble-region away from the wall (see figure 3.13b) shows large $O(1)$ time-periodic fluctuations about the asymptotic mean value, in sharp contrast to figure 3.13(a), indicating the presence of a time-periodic asymptotic state.

The above dominant balance argument has several important consequences that are easily cross-checked against numerical observations. Firstly, if $O(x_2)$ and $O(Pe^{-1}x_2^{-2})$ are to be in balance, x_2 cannot scale with respect to β, ω, and is simply $O(Pe^{-1/3})$. That is, the boundary-layer thickness cannot scale with respect to perturbation amplitude β. Verification is provided by Wiener bundle computations of asymptotic centerline profiles along $(x_1 = 0, x_2 > 0)$ at several β, shown in figure 3.14.

Secondly, to dominant order the instantaneous wall-integrated flux is given by

$$J_w(t) = Pe^{-2/3} \int_{-1.5}^{1.5} \frac{\partial \theta}{\partial \hat{x}_2}\Big|_{\hat{x}_2 \to 0} dx_1,$$

where $\hat{x}_2 = Pe^{1/3}x_2$ is the properly scaled coordinate in the boundary-layer. It can be shown (see Part II) that the contribution to the instantaneous wall-integrated flux

from the thermal boundary-layer region in the vicinity of the separation point p^- can be ignored to dominant order, and therefore does not appear in the expression above. Substituting (3.10) above gives

$$J_w(t) = Pe^{-2/3} \int_{-1.5}^{1.5} \frac{\partial \theta_0}{\partial \hat{x}_2}\Big|_{\hat{x}_2 \to 0} \, dx_1 + \bar{\epsilon} Pe^{-2/3} \int_{-1.5}^{1.5} \frac{\partial \theta_1}{\partial \hat{x}_2}\Big|_{\hat{x}_2 \to 0} \, dx_1 .$$

The flux $J_w(t)$ (as well as $< J_w(t) >_T$) is therefore $O(Pe^{-2/3})$, identical to the $\beta = 0$ case. Flux enhancement due to chaotic advection is therefore expected to be minimal as β appears only in second-order effects. These conclusions are in agreement with the numerical results of figure 3.12(b). Moreover, $J_w(t)$ is time-independent to dominant order and has a weak $O(\bar{\epsilon} Pe^{-2/3})$ time-dependence owing to second-order effects. This accounts for the observed feature that the time-averaged wall-integrated flux $< J_w(t) >_T$ is fairly insensitive to the averaging period T.

3.5 Case with oscillating points of zero shear-stress

Results obtained by Shariff, Pulliam & Ottino (1991) show that for two-dimensional time-periodic incompressible flows adjacent to a plane no-slip boundary, the necessary condition for a point on the no-slip boundary $(x_1^*, 0)$ to have a one-dimensional stable/unstable manifold for the corresponding Poincaré map, with the manifold emanating with non-zero slope, is the following:

$$\int_0^T \frac{\partial u_1}{\partial x_2}(x_1 = x_1^*, x_2 = 0) dt = 0, \tag{3.11}$$

where x_1 is the coordinate along the boundary, x_2 is the coordinate normal to the boundary, and u_1 is the x_1-component of the velocity field, i.e., the time-averaged shear-stress must vanish at the manifold emanation points. In Appendix C the result is extended to include stable/unstable manifolds that are analytic at the emanation point and emanate with arbitrary slope. Here we point out it's consequences on the scalar distribution in the context of our advection-diffusion problem.

To this end, we first set-up a chaotic advection field which has oscillating points of zero shear-stress on the no-slip boundary. The time-periodic velocity field of (2.9) has two points of zero shear-stress on the no-slip boundary at all times, given by $x_1 = \pm 1$, i.e., the points of zero shear-stress are independent of time t. The point $(-1, 0)$ corresponds to the separation point p^-, while $(+1, 0)$ corresponds to the attachment point p^+. For the corresponding Poincaré map $P_\beta^{\bar{\phi}}$, p^- and p^+ are the only points on the no-slip boundary having one-dimensional unstable/stable manifolds, irrespective of the cross-section $\bar{\phi}$. Consider now a time-periodic perturbation of (2.6) that not only generates chaotic particle trajectories in the bubble-region but also creates two points of zero shear-stress on the no-slip boundary that are not time-independent, but instead oscillate periodically about $x_1 = \pm 1$. This is achieved easily by adding an appropriate perturbation term to (2.3); the boundary vorticity in the time-dependent flow is made to vary according to the equation:

$$w(x_2 = 0) \equiv -\frac{\partial u_1}{\partial x_2}\bigg|_{x_2=0} = -K(x_1^2 - x_s^2 + \beta x_1 x_s \sin(\omega t)).$$

The appropriately non-dimensionalised velocity field, truncated again to third-order, is given by

$$\begin{aligned} u_1 &= -x_2 + 3x_2^2 + x_1^2 x_2 - \frac{2}{3}x_2^3 + \beta x_1 x_2 \sin(\omega t), \\ u_2 &= -x_1 x_2^2 - \frac{\beta}{2} x_2^2 \sin(\omega t), \end{aligned} \tag{3.12}$$

which is again an asymptotically exact solution of the Navier-Stokes and continuity equations close to the origin of the expansion. The points of zero shear-stress on the no-slip boundary $(x_1, 0)$ are now given by

$$x_1 = \pm 1 - \frac{\beta}{2}\sin(\omega t) + O(\beta^2).$$

However, applying Shariff *et al.*'s result of (3.11), for the Poincaré map $P_\beta^{\bar{\phi}}$ corresponding to the velocity field of (3.12) the only points on the no-slip boundary

$(x_1^*, 0)$ having a one-dimensional stable/unstable manifold are located at $x_1^* = \pm 1$. Notice that the necessary condition of (3.11) is independent of the cross-section or phase $\bar{\phi}$ of the Poincaré map $P_\beta^{\bar{\phi}}$, which implies that though the points of zero-shear stress on the no-slip boundary oscillate in a time-periodic manner, the manifold emanation points are time-independent and remain the same for every $P_\beta^{\bar{\phi}}$, irrespective of $\bar{\phi}$. Therefore, while the unstable manifold $W_\beta^u(\bar{\phi})$ changes structure with $\bar{\phi}$, the manifold emanation point or separation point remains stationary at the wall. This property becomes transparent from numerical simulation results of figure 3.15(a-c) for the scalar distribution computed at times that are *not* integral multiples of the period $T = 2\pi/\omega$ of the time-periodic velocity field of (3.12) and therefore correspond to *different* cross-sections $\bar{\phi}$. Thus, despite the fact that (3.12) and (2.9) are very different chaotic advection fields, the scalar distributions for the associated advection-diffusion problem at large Peclet numbers share the same qualitative features owing to the similarity in the underlying geometrical structures in the two cases. This further reinforces the importance of the underlying geometrical structures in determining the scalar distribution in chaotic advection fields.

The asymptotic time-averaged wall-integrated flux $< J_w(t) >_T$ again shows weak enhancement over the steady-advection-case, which is not surprising following our discussion in §3.4. Temperature time-series in the thermal boundary-layer indicates weak time-dependence as before, and is attributed to the absence of time-dependent structures in the near-wall region in the sense of oscillating manifold emanation points. Moreover, it should be clear from equation (3.11) that regardless of the order of the expansion, every time-periodic velocity field will have time-independent manifold emanation points at the no-slip boundary. Finally, we note that it might be possible to generate time-dependent structures in the near-wall region for two-dimensional chaotic advection fields with more complicated time-

dependences, in particular quasi-periodic time-dependence.

3.6 Impact of changing bubble-size

The size of the steady separation bubble can be varied by varying the coefficient A_{122} in the time-independent velocity field of (2.5); A_{122} must lie within the appropriate limits given in §2.1. Introducing a time-periodic perturbation as in (2.7) and truncating the series expansion to third-order gives a chaotic advection field identical to (2.9) with time-independent component $f^u(x)$, expressed now in terms of the unspecified coefficient A_{122},

$$f^u \equiv (f_1^u, f_2^u) = (-x_2 + \frac{A_{122}}{Kx_s}x_2^2 + x_1^2 x_2 - \frac{2}{3}x_2^3, -x_1 x_2^2). \tag{3.13}$$

We consider here the effect of variations in the coefficient A_{122} on the chaotic advection field above and, consequently, on the scalar distribution in the associated advection-diffusion problem.

Thus far we have presented numerical simulation results for $A_{122} = 3Kx_s$. Time-dependent scalar distributions are now computed at two different values of the coefficient A_{122}: in figure 3.16(a,b), scalar distributions are obtained for $A_{122} = 4.5Kx_s$, while in figure 3.17(a,b) the scalar distributions are obtained for $A_{122} = 2Kx_s$, with the perturbation parameters β, ω and the Peclet number Pe identical in the two cases. The perturbation parameters β, ω were chosen in a manner such that for both values of A_{122} considered here, the corresponding Poincaré maps have no KAM tori enclosing the core-region of the bubble. In fact, the surviving KAM tori are of negligible size in both cases. Further, the value of $\omega = 0.5$ turns out to be close to the values of the perturbation frequency at which the amplitude $A(\omega)$ of the Melnikov function is maximum in either case; the value of ω at which $A(\omega)$ is maximum is of course different for different A_{122}, but are fortunately not widely separated for the two A_{122}'s considered here. This is evident from figures 3.18(a)

and (b), where $A(\omega)$ is computed at several ω for $A_{122} = 4.5Kx_s$ and $A_{122} = 2Kx_s$, respectively.

Evidently, there is a sharp qualitative difference in the scalar distributions for the two cases. It is observed that at smaller A_{122}, the unstable manifold $W^u_{\bar{\phi}}(\bar{\phi})$ plays a more dominant organizing role in the distribution of the passive scalar. This can be verified by comparing figures 3.16 and 3.17 with figures 3.19 and 3.20 respectively; in figure 3.19 the unstable manifold $W^u_{\bar{\phi}}$ is computed for β, ω and A_{122} identical to that in figure 3.16, while in figure 3.20, $W^u_{\bar{\phi}}$ is computed for β, ω and A_{122} identical to that in figure 3.17. Large advection velocities make resolution of $W^u_{\bar{\phi}}$ difficult in figure 3.20, but is sufficient to establish its role in the scalar distribution of figure 3.17. Moreover, the distributions are more localized and non-uniform at smaller A_{122}. Following our arguments in §3.4, it is not surprising that the wall-integrated flux is observed to be largely insensitive to variations in A_{122}, as long as A_{122} is not too large.

While for $\beta = 0$, i.e., for steady advection, the value of A_{122} determines the size of the separation bubble, for $\beta \neq 0$ but β small, A_{122} determines the location of the *heteroclinic tangle* formed by the intersections of the stable and unstable manifolds, $W^s_{\bar{\phi}}(\bar{\phi})$ and $W^u_{\bar{\phi}}(\bar{\phi})$ respectively, of the Poincaré map $P^{\bar{\phi}}_{\bar{\phi}}$ corresponding to the time-periodic chaotic advection field. In fact, it is a simple consequence of Gronwall's lemma (e.g., see Wiggins 1990) that trajectories under $P^{\bar{\phi}}_{\bar{\phi}}$ with initial position on $W^u_{\bar{\phi}}(\bar{\phi})$ in the vicinity of the separation point p^-, must remain $O(\beta)$ close to the unperturbed separatrix ψ_h for small β, until they enter a small neighborhood of the attachment point p^+. Then, since A_{122} determines the shape of the separatrix ψ_h, it strongly influences the shape of the unstable manifold $W^u_{\bar{\phi}}(\bar{\phi})$. Moreover, variations in A_{122} cause sharp variations in the stretching properties of the chaotic advection field, evidence of which will be presented later; lower the value of A_{122} ($A_{122} >$

$(8/3)^{\frac{1}{2}} K x_s$), the greater the *stretching* and *contraction* rates - precise definitions are given in Chapter 5 - in the chaotic bubble-region. These two factors account for vastly different scalar distributions at different A_{122}. To what extent these advection-diffusion phenomena at small scalar diffusivity can be understood in terms of the dynamics under (2.9) is the content of the following sections.

FIGURES

Figure 3.1: Crosses represent temperature field for heat conduction in semi-infinite solid, obtained from a whole-field-random-walk computation, for $D = 0.001$ at time $t = 5$. The solid line represents the analytical solution of (3.6) at the same D and t.

Figure 3.2: Triangles represent instantaneous flux $J_w(t)$ at the boundary $z = 0$, obtained from a whole-field-random-walk computation, for $D = 0.001$ at several t. The solid line represents the analytical solution of (3.7) at the same D.

Figure 3.3: Scalar field for $\beta = 0.6$, $\omega = 0.72$, $Pe = 2.5 \times 10^4$, at (a) $t = 5T$, (b) $t = 10T$, (c) $t = 20T$, (d) $t = 30T$, $T = 2\pi/\omega$.

Figure 3.4: Scalar field for $\beta = 0.2$, $\omega = 0.72$, $Pe = 2.5 \times 10^4$, at (a) $t = 5T$, (b) $t = 10T$, (c) $t = 20T$, (d) $t = 30T$, $T = 2\pi/\omega$.

Figure 3.5: Scalar field for the steady separation bubble, for $Pe = 2.5 \times 10^4$, at (a) $t = 5T$, (b) $t = 10T$, (c) $t = 20T$, (d) $t = 60T$, T same as in figures 3.3, 3.4.

Figure 3.6: Scalar field for $\beta = 0.8$, $\omega = 0.72$, $Pe = 2.5 \times 10^4$, at (a) $t = 5T$, (b) $t = 10T$, (c) $t = 20T$, (d) $t = 30T$, $T = 2\pi/\omega$.

Figure 3.7: Scalar field for $\beta = 1.0$, $\omega = 0.72$, $Pe = 2.5 \times 10^4$, at (a) $t = 5T$, (b) $t = 10T$, (c) $t = 20T$, (d) $t = 30T$, $T = 2\pi/\omega$.

Figure 3.8: A Poincaré map of the bubble-region for $\beta = 0.2$, $\omega = 2.0$.

Figure 3.9: Scalar field for $\beta = 0.2$, $\omega = 2.0$, $Pe = 2.5 \times 10^4$, at (a) $t = 10T$, (b) $t = 20T$, where T is same as in figures 3.3-3.6, i.e., $T = 2\pi/0.72$.

Figure 3.10: The unstable manifold $W^u_\beta(\bar{\phi})$, at $\beta = 0.2$, $\omega = 2.0$, and cross-section $\bar{\phi}$ corresponding to (a) $t = 10T$, (b) $t = 20T$, where T is same as in figures 3.3-3.6, i.e., $T = 2\pi/0.72$.

Figure 3.11: Distribution of the scalar field along the centerline ($x_1 = 0, x_2 > 0$), extracted from figure 3.3, at (a) $t = 5T$, (b) $t = 30T$, shown in solid lines; T same as in figure 3.3. Dots represent Wiener bundle solutions at $\beta = 0.6$, $\omega = 0.72$, $Pe = 2.5 \times 10^4$.

Figure 3.12(a): Time-averaged wall-integrated flux $< J_w(t) >_T$ for $\beta = 0$, 0.2 and 0.6, with $\omega = 0.72$, $Pe = 2.5 \times 10^4$, and $T = 2\pi/\omega$.

Figure 3.12(b): Asymptotic $< J_w(t) >_T$ at several $\beta \in [0, 1]$, for $\omega = 0.72$, $Pe = 2.5 \times 10^4$, and $T = 2\pi/\omega$.

Figure 3.13: Time-series using the Wiener bundle method, at (a) $(x_1, x_2) = (0, 0.04)$, (b) $(x_1, x_2) = (-0.547, 0.321) \in W^u_\beta$, for $\beta = 0.6$, $\omega = 0.72$, and $Pe = 2.5 \times 10^4$.

Figure 3.14: Wiener bundle solutions of the scalar field along the centerline ($x_1 = 0, x_2 > 0$) at $t = 20T$ for several $\beta \in (0, 1]$, with $\omega = 0.72$, $Pe = 2.5 \times 10^4$, and $T = 2\pi/\omega$.

Figure 3.15: Scalar field corresponding to the chaotic advection field of (3.12), for $\beta = 0.4$, $\omega = 0.65$, $Pe = 2.5 \times 10^4$, at (a) $t = 5.25T$, (b) $t = 5.75T$, (c) $t = 6T$, $T = 2\pi/\omega$.

Figure 3.16: Scalar field corresponding to the chaotic advection field of (2.9), but with time-independent component (3.13), for $A_{122} = 4.5Kx_s$, with $\beta = 0.5, \omega = 0.5$, $Pe = 2.5 \times 10^4$, at (a) $t = 10T$, (b) $t = 20T$, $T = 2\pi/\omega$.

Figure 3.17: Scalar field corresponding to the chaotic advection field of (2.9), but with time-independent component (3.13), for $A_{122} = 2Kx_s$, with $\beta = 0.5$, $\omega = 0.5$, $Pe = 2.5 \times 10^4$, at (a) $t = 10T$, (b) $t = 20T$, $T = 2\pi/\omega$.

Figure 3.18: The amplitude $A(\omega)$ of the Melnikov function for the chaotic advection field of (2.9), but with time-independent component f^u given by (3.13), is plotted versus ω for (a) $A_{122} = 4.5Kx_s$ (b) $A_{122} = 2Kx_s$.

Figure 3.19: The unstable manifold W^u_β for $A_{122} = 4.5Kx_s$; β, ω same as in figure 3.17.

Figure 3.20: The unstable manifold W^u_β for $A_{122} = 2Kx_s$; β, ω same as in figure 3.18.

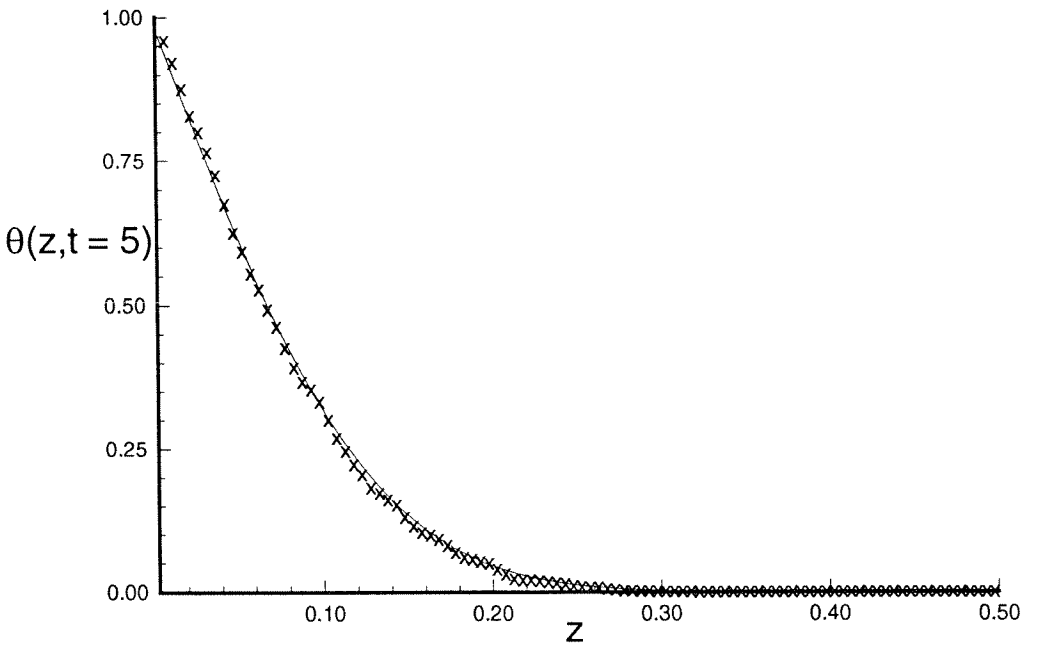

Figure 3.1

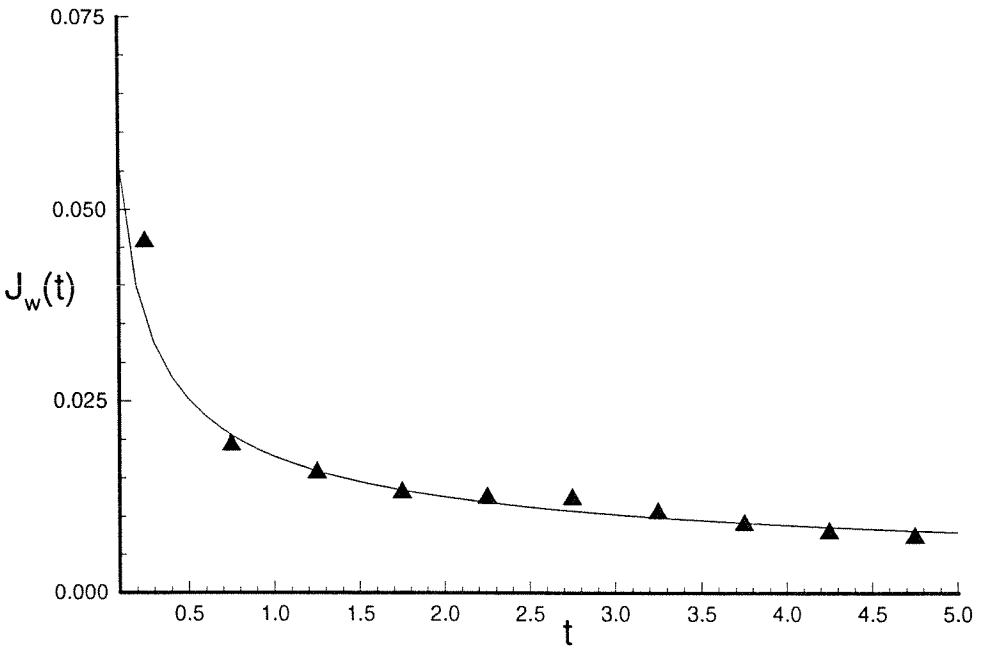

Figure 3.2

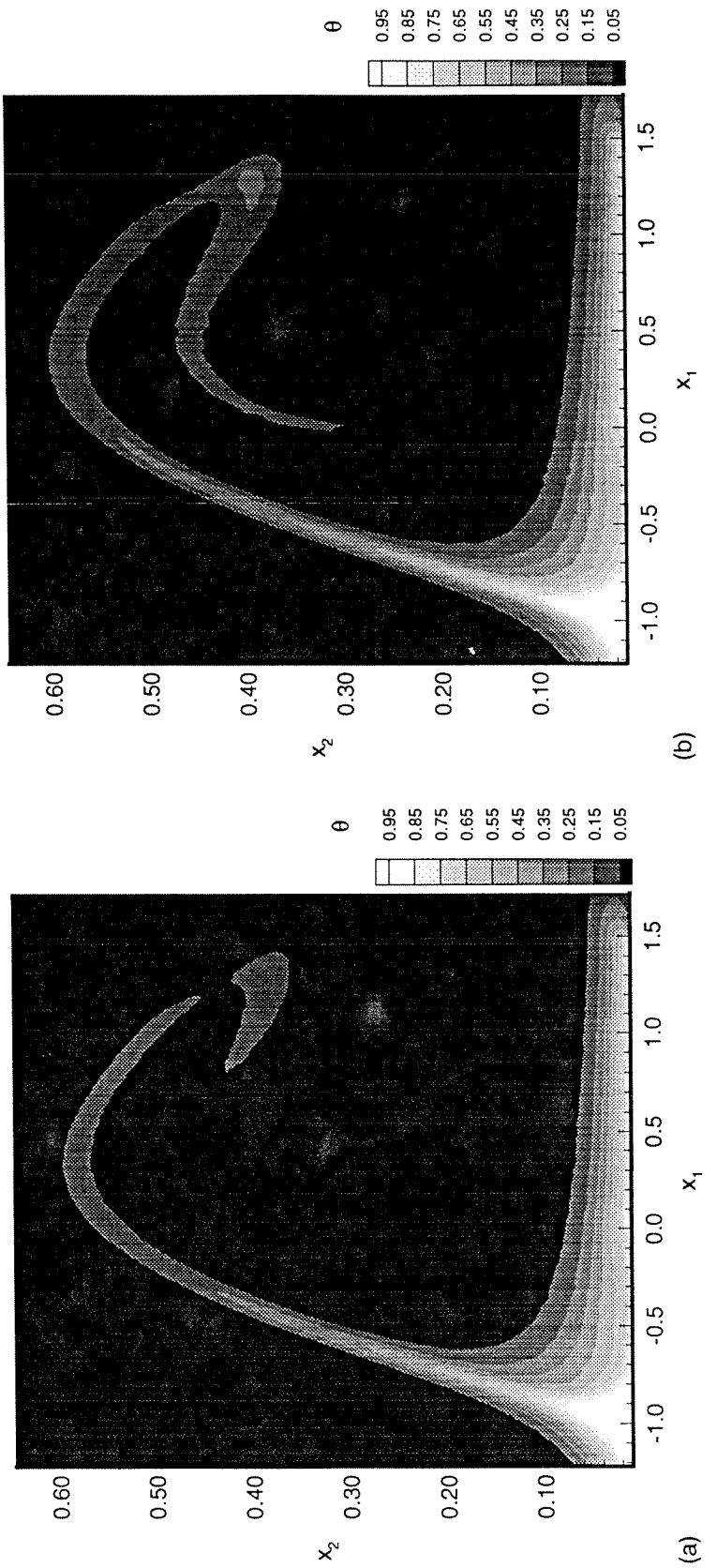
θ
0.95
0.85
0.75
0.65
0.55
0.45
0.35
0.25
0.15
0.05
0.60
0.50
0.40
0.30
0.20
0.10
x_2
-1.0
-0.5
0.0
0.5
1.0
1.5
x_1
(a)
(b)

Figure 3.3(a,b)

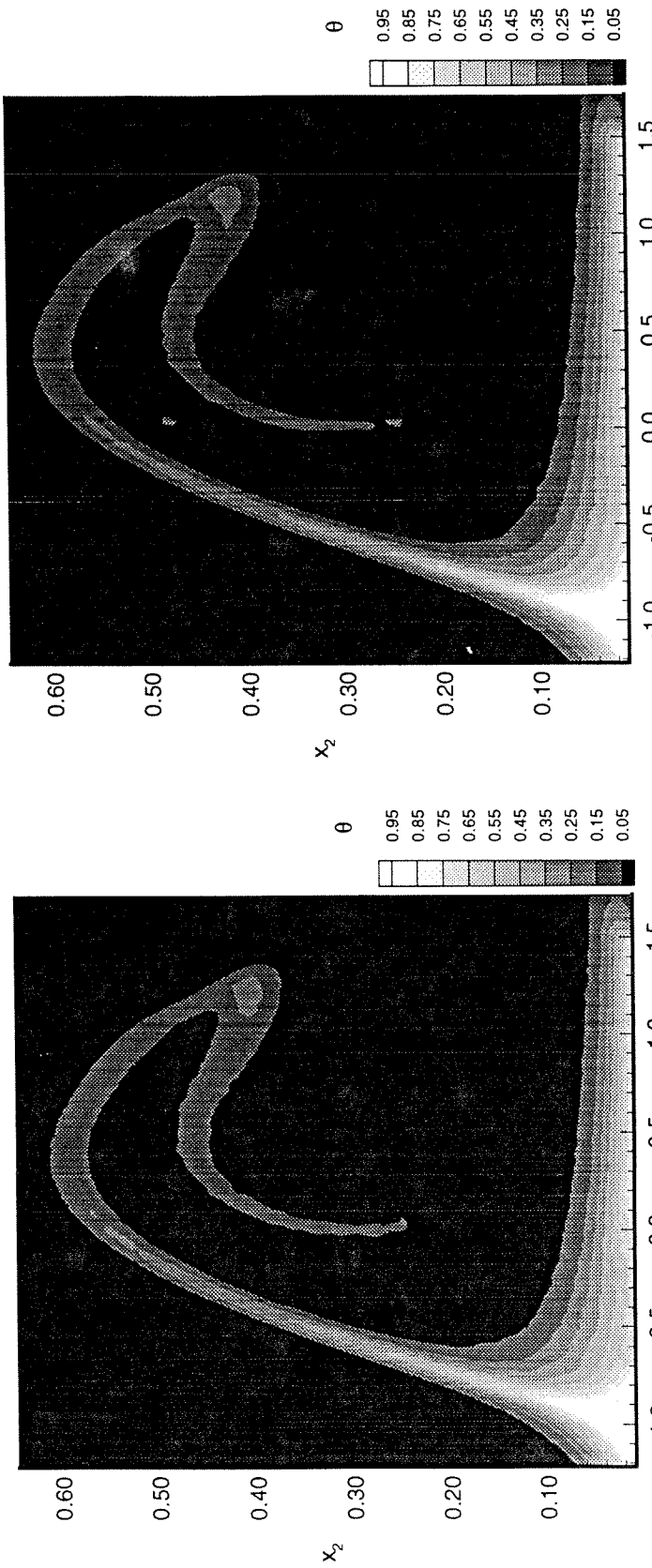
θ
0.95
0.85
0.75
0.65
0.55
0.45
0.35
0.25
0.15
0.05
0.60
0.50
0.40
0.30
0.20
0.10
x_2
-1.0
-0.5
0.0
0.5
1.0
1.5
x_1
(a)
(b)

Figure 3.3(c,d)

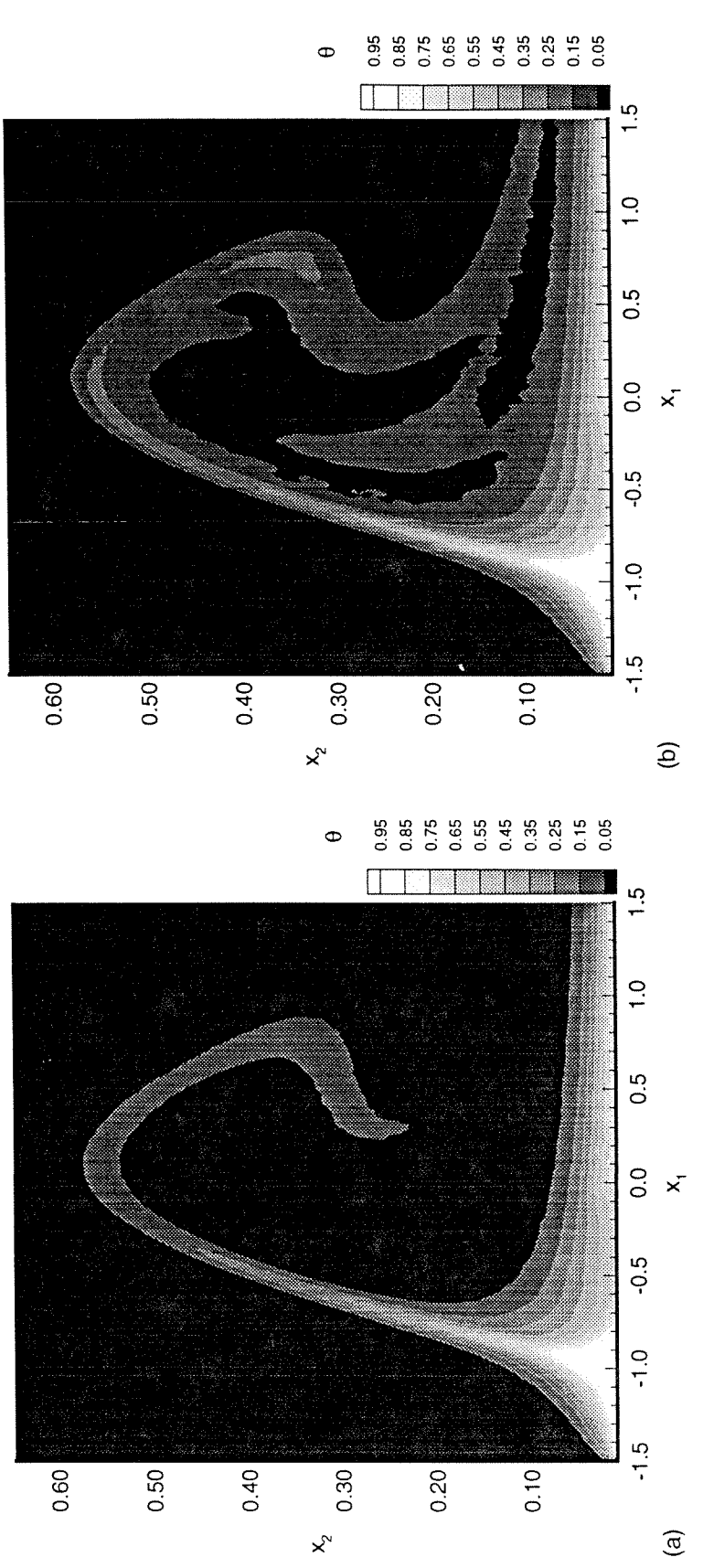
θ
0.95
0.85
0.75
0.65
0.55
0.45
0.35
0.25
0.15
0.05
0.60
0.50
0.40
0.30
0.20
0.10
x_2
-1.5
-1.0
-0.5
0.0
0.5
1.0
1.5
x_1
(a)
(b)

Figure 3.4(a,b)

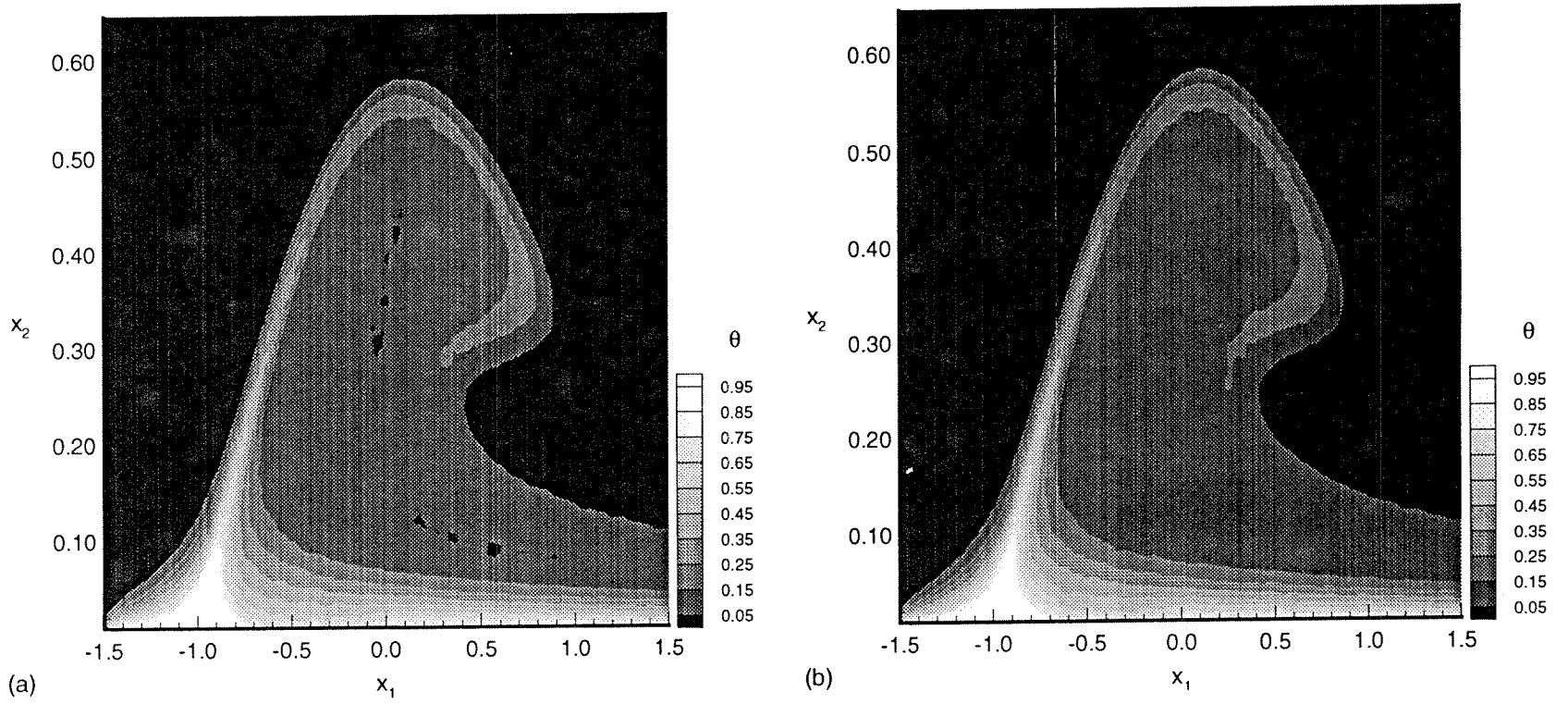
0.60
0.50
0.40
0.30
0.20
0.10
x_2
θ
0.95
0.85
0.75
0.65
0.55
0.45
0.35
0.25
0.15
0.05
-1.5
-1.0
-0.5
0.0
0.5
1.0
1.5
x_1
(a)
(b)

Figure 3.4(c,d)

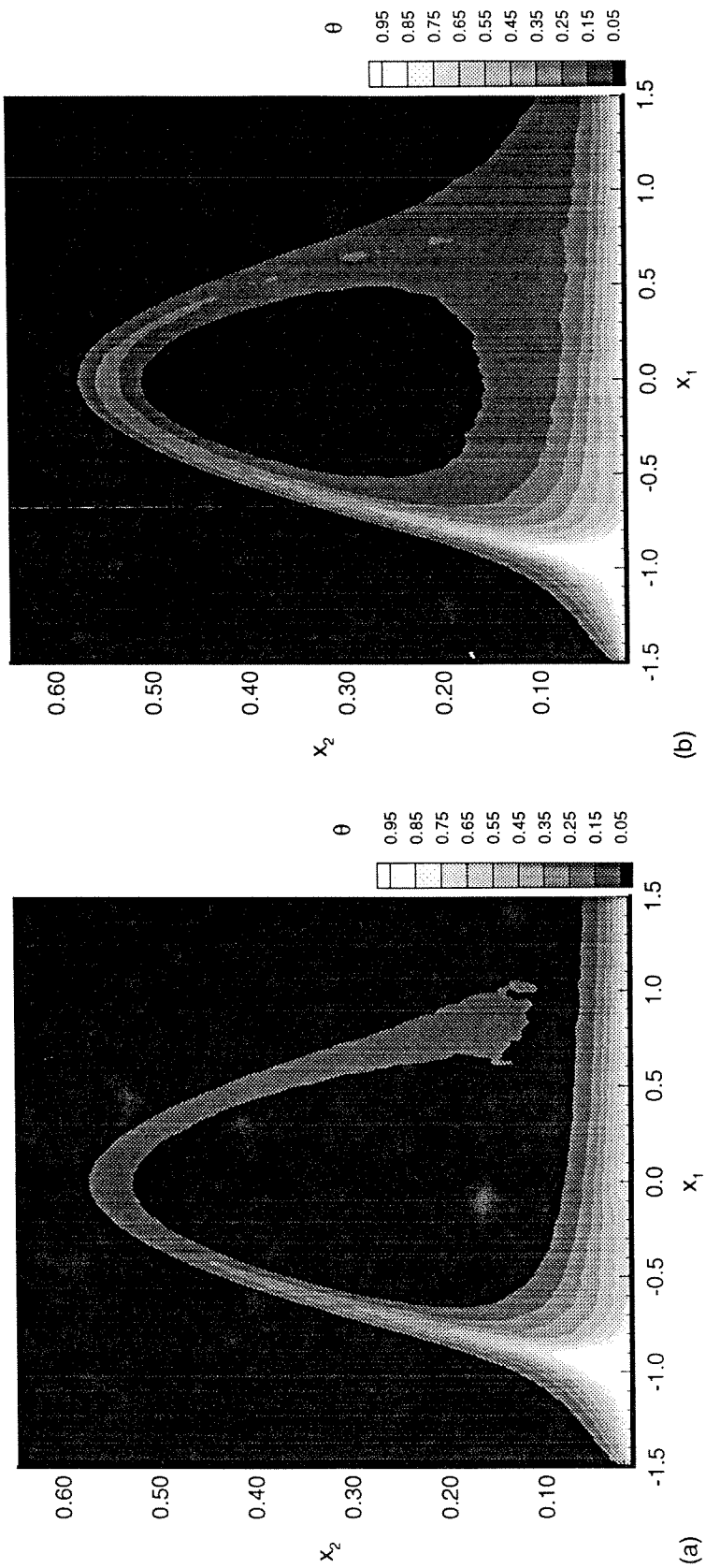
θ
0.95
0.85
0.75
0.65
0.55
0.45
0.35
0.25
0.15
0.05
0.60
0.50
0.40
0.30
0.20
0.10
x_2
-1.5
-1.0
-0.5
0.0
0.5
1.0
1.5
x_1
(a)
(b)

Figure 3.5(a,b)

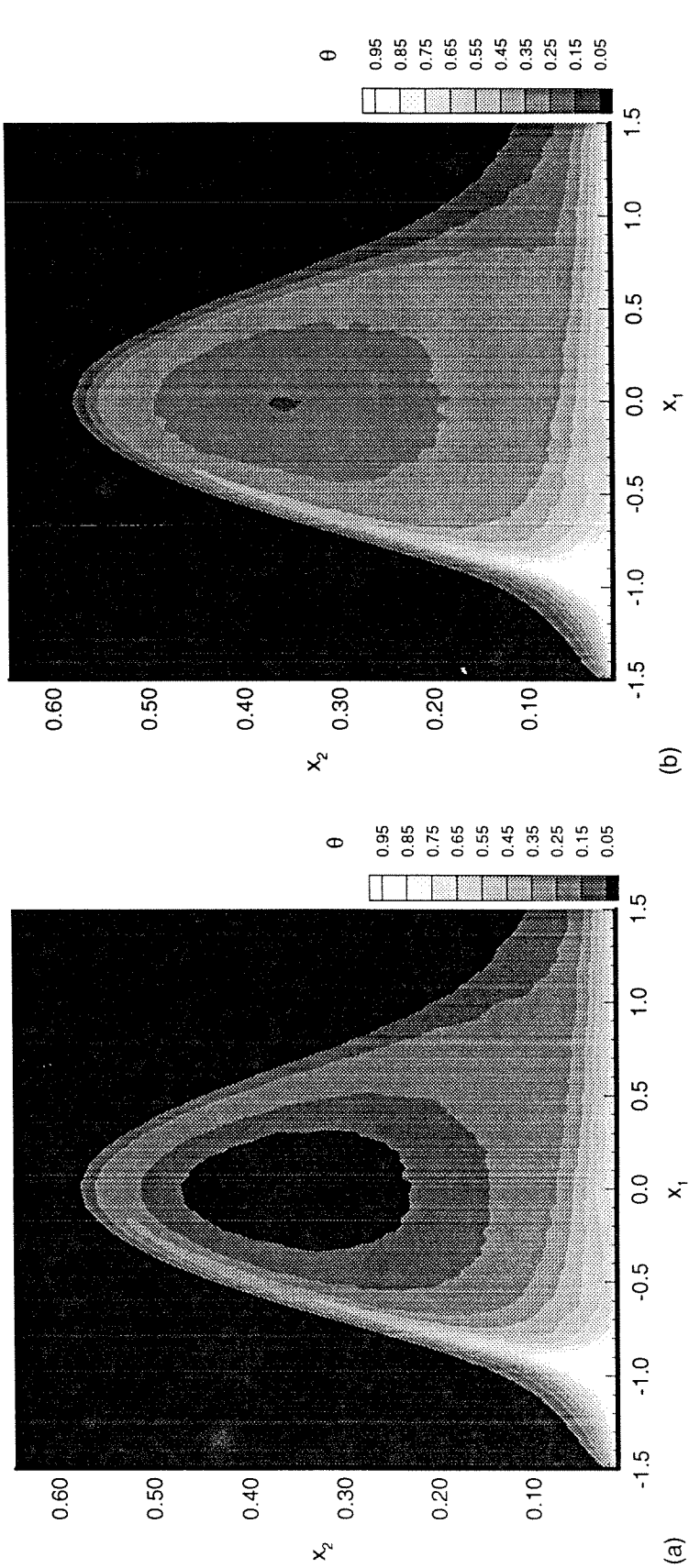
θ
0.95
0.85
0.75
0.65
0.55
0.45
0.35
0.25
0.15
0.05
0.60
0.50
0.40
0.30
0.20
0.10
x_2
-1.5
-1.0
-0.5
0.0
0.5
1.0
1.5
x_1
(a)
(b)

Figure 3.5(c,d)

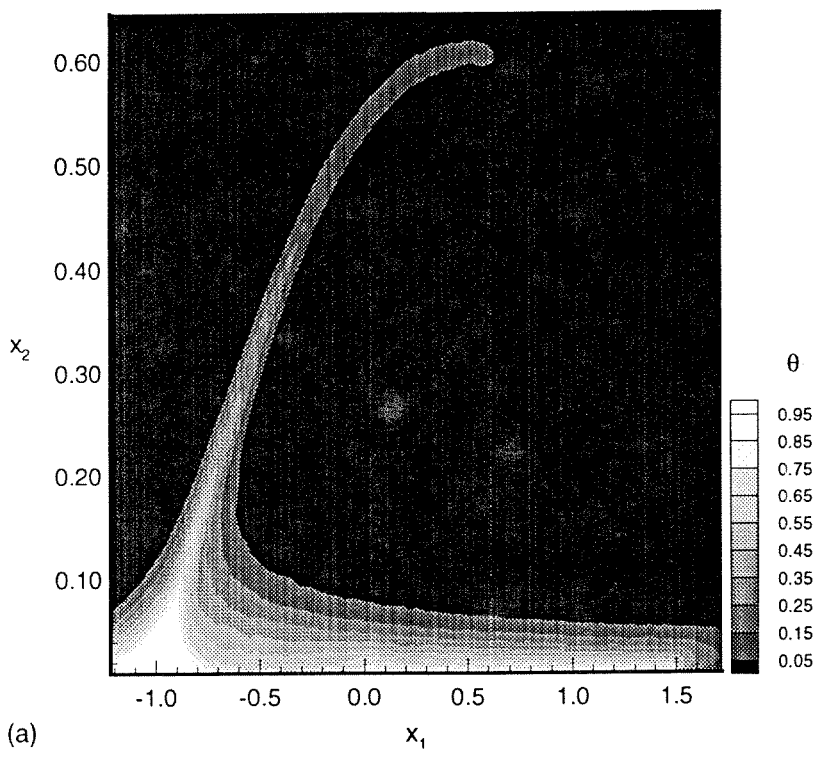
0.60
0.50
0.40
0.30
0.20
0.10
x_2
θ
0.95
0.85
0.75
0.65
0.55
0.45
0.35
0.25
0.15
0.05
-1.0
-0.5
0.0
0.5
1.0
1.5
x_1
(a)

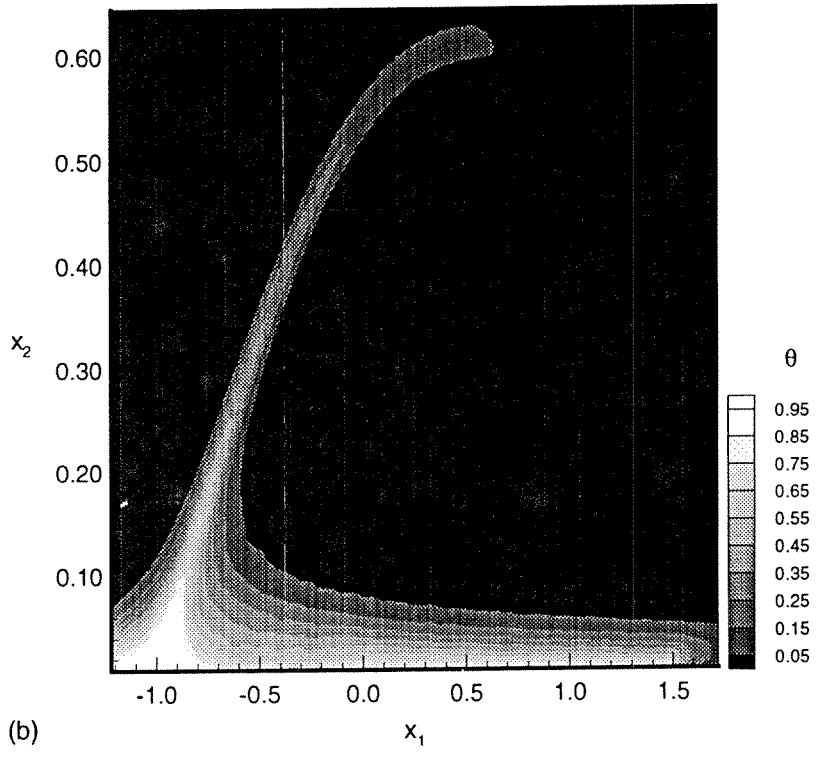
0.60
0.50
0.40
0.30
0.20
0.10
x_2
θ
0.95
0.85
0.75
0.65
0.55
0.45
0.35
0.25
0.15
0.05
-1.0
-0.5
0.0
0.5
1.0
1.5
x_1
(b)

Figure 3.6(a,b)

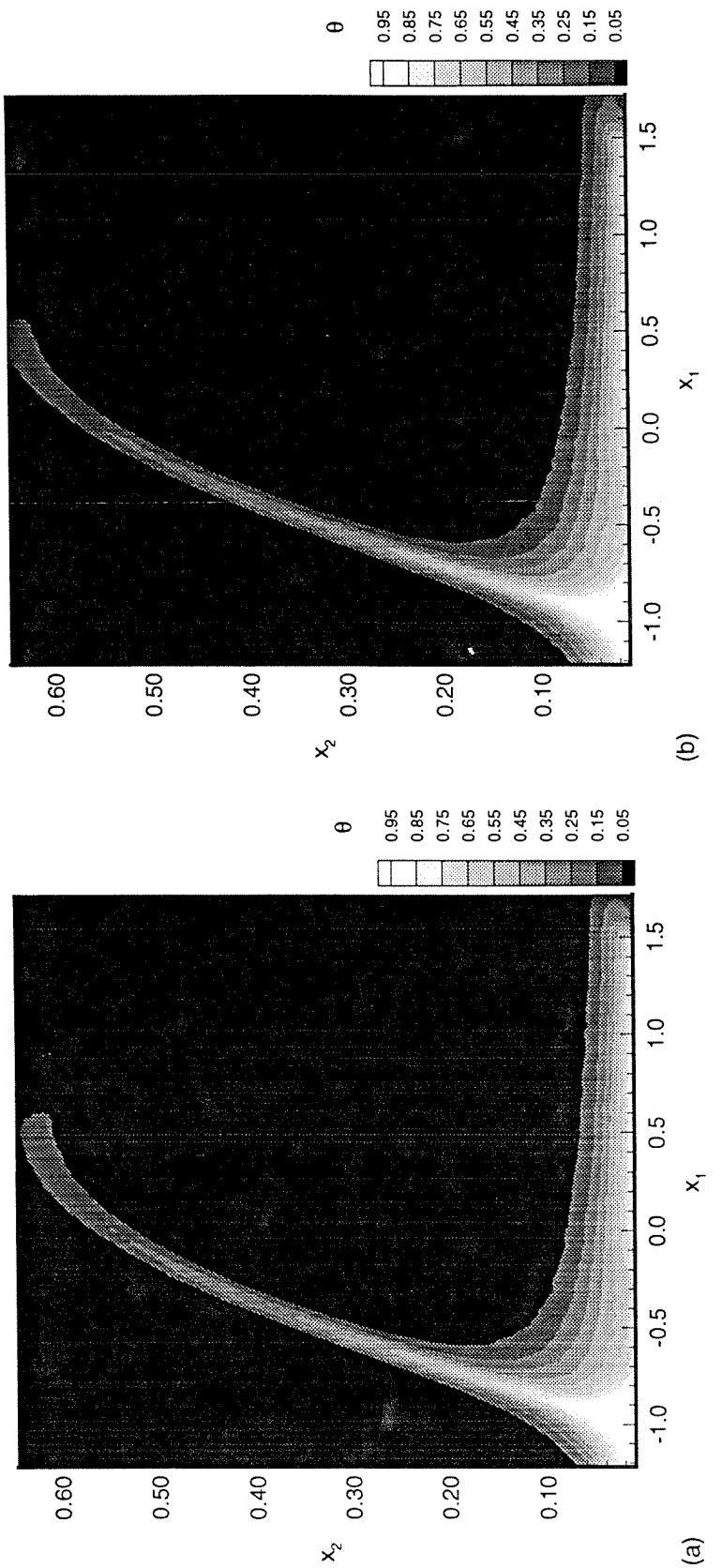
θ
0.95
0.85
0.75
0.65
0.55
0.45
0.35
0.25
0.15
0.05
0.60
0.50
0.40
0.30
0.20
0.10
x_2
-1.0
-0.5
0.0
0.5
1.0
1.5
x_1
(a)
(b)

Figure 3.6(c,d)

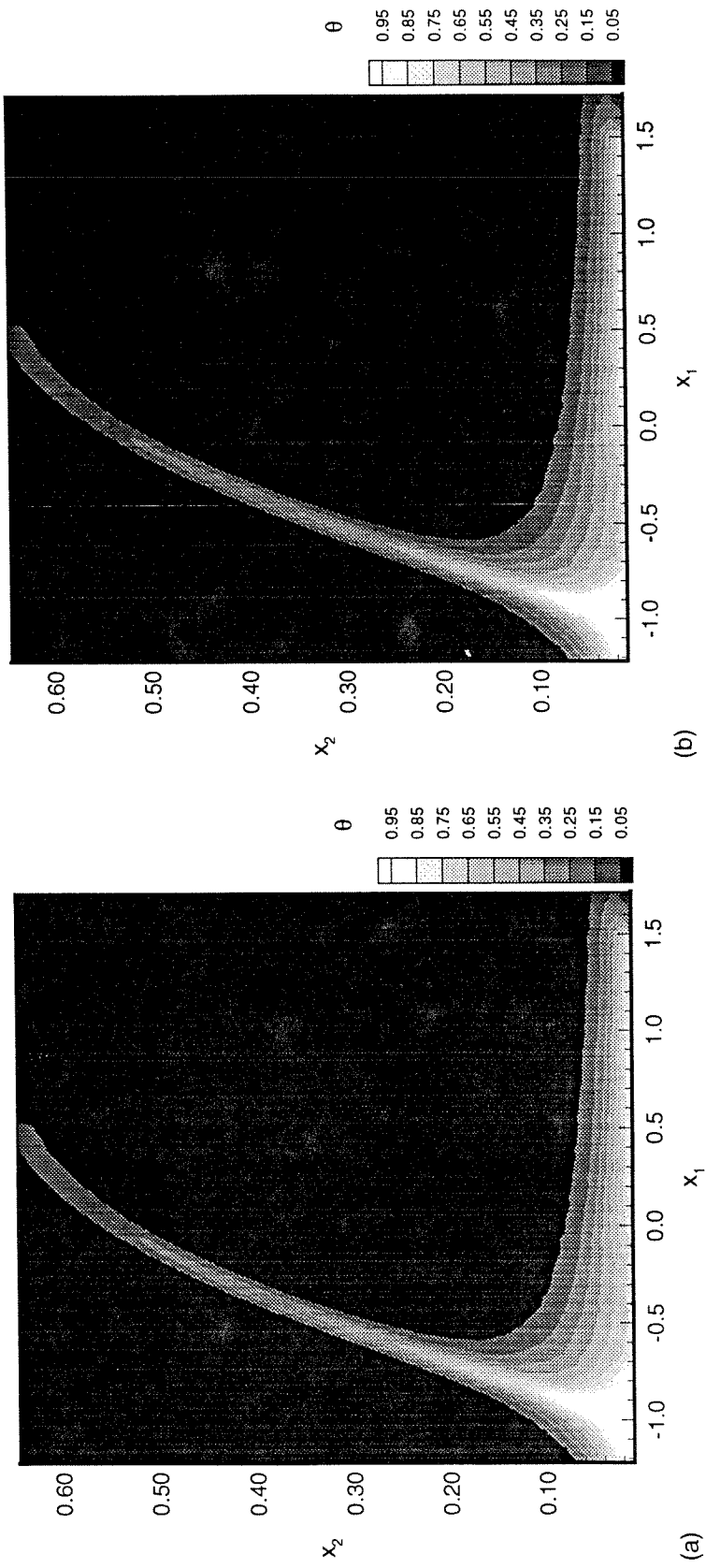
θ
0.95
0.85
0.75
0.65
0.55
0.45
0.35
0.25
0.15
0.05
0.60
0.50
0.40
0.30
0.20
0.10
x_2
-1.0
-0.5
0.0
0.5
1.0
1.5
x_1
(a)
(b)

Figure 3.7(a,b)

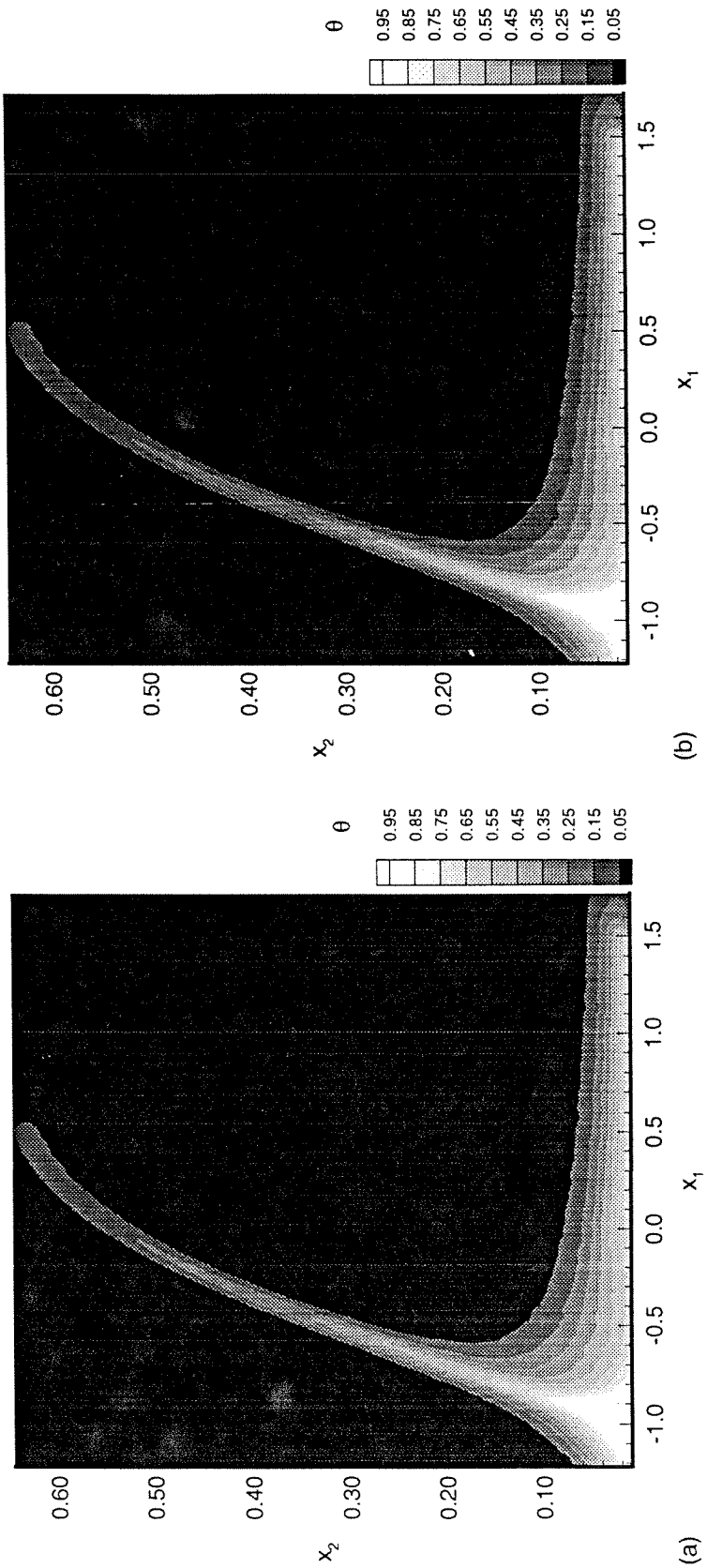
θ
0.95
0.85
0.75
0.65
0.55
0.45
0.35
0.25
0.15
0.05
0.60
0.50
0.40
0.30
0.20
0.10
x_2
-1.0
-0.5
0.0
0.5
1.0
1.5
x_1
(a)
(b)

Figure 3.7(c,d)

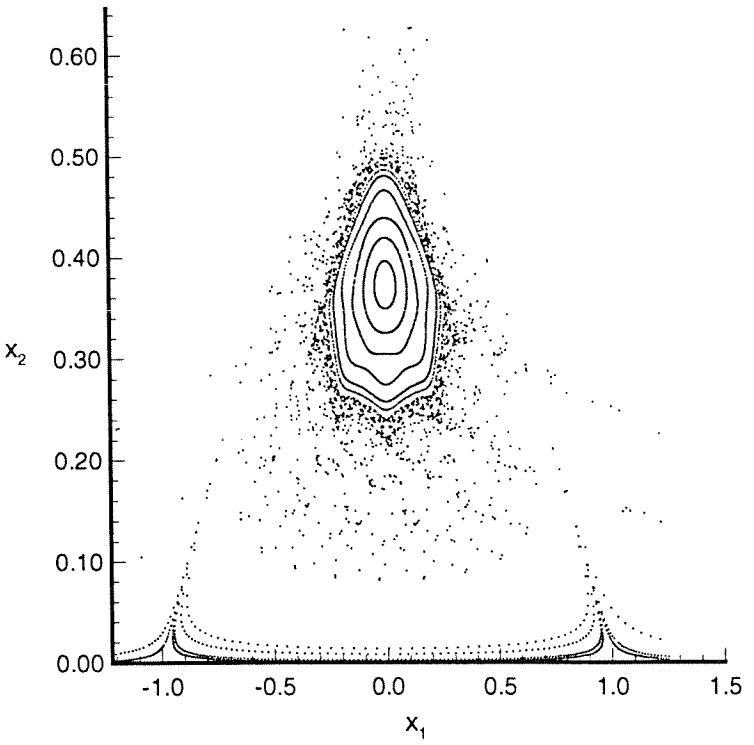

Figure 3.8

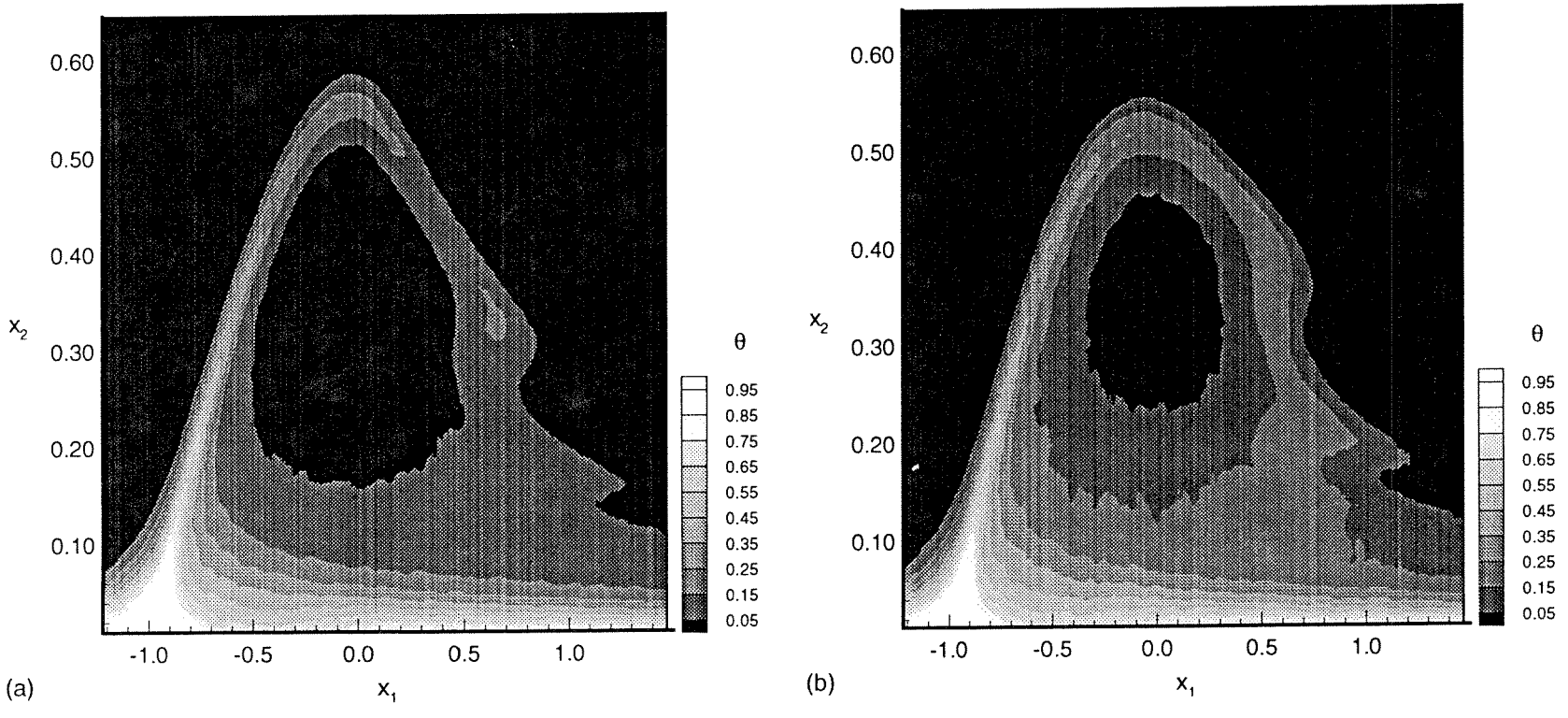
0.60
0.50
0.40
0.30
0.20
0.10
x_2
θ
0.95
0.85
0.75
0.65
0.55
0.45
0.35
0.25
0.15
0.05
-1.0
-0.5
0.0
0.5
1.0
x_1
(a)
(b)

Figure 3.9(a,b)

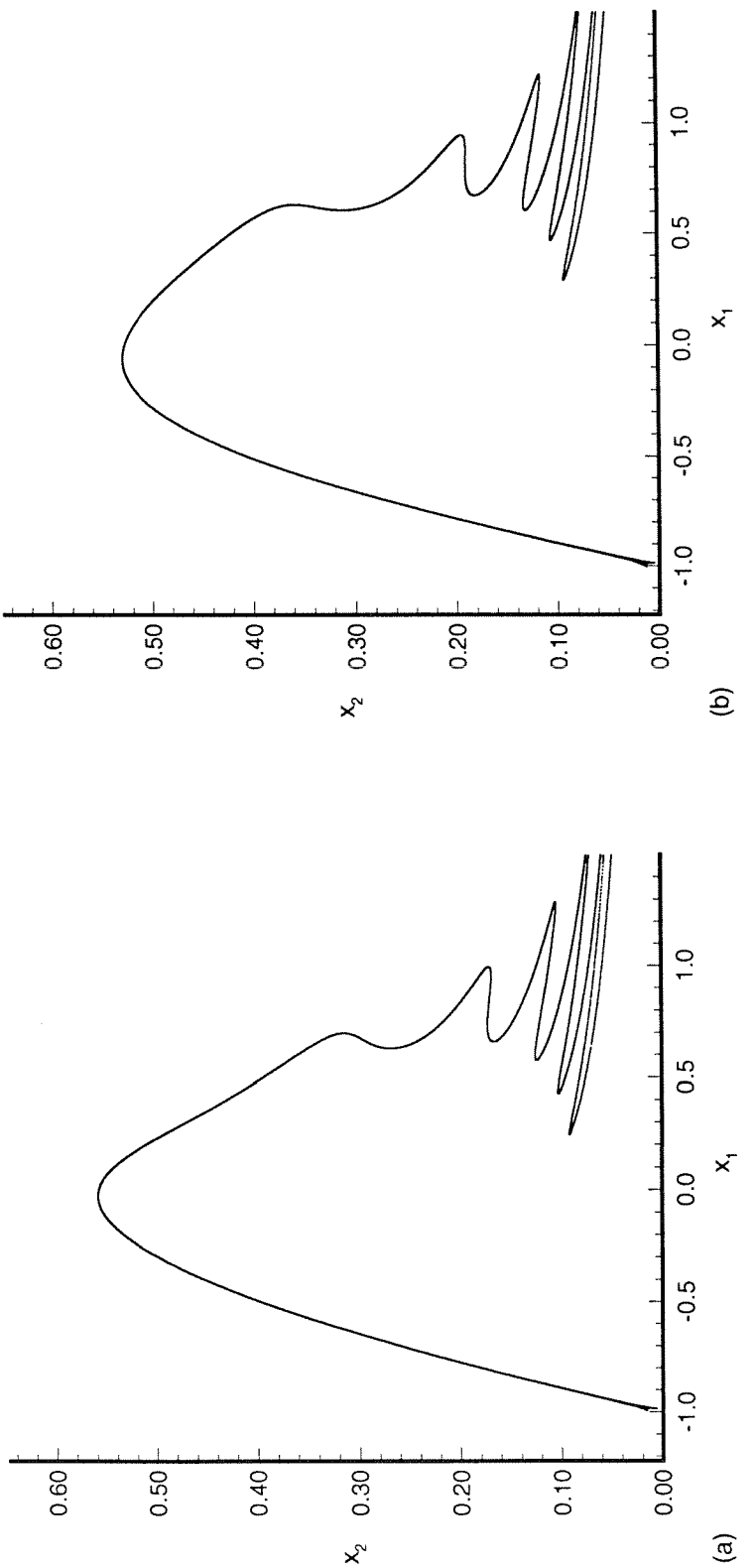

Figure 3.10(a,b)

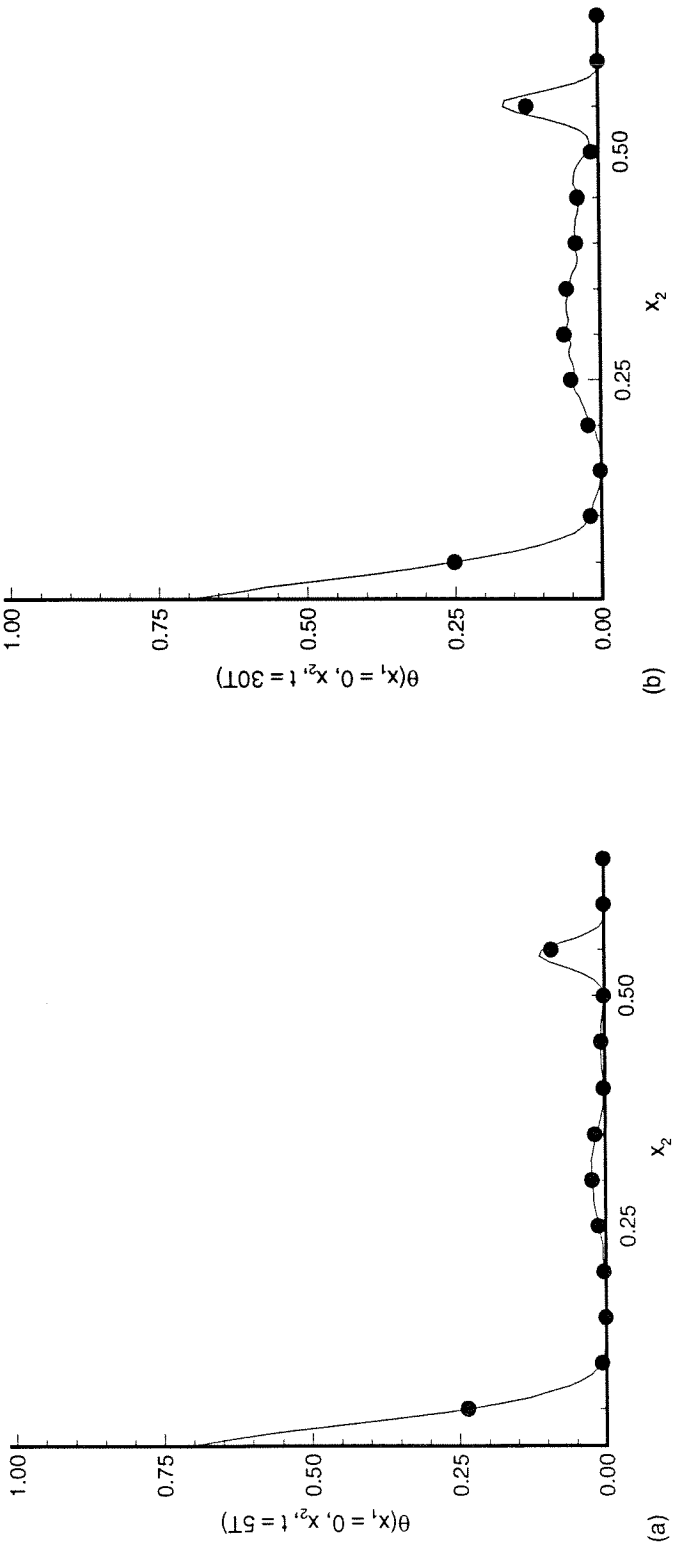

Figure 3.11(a,b)

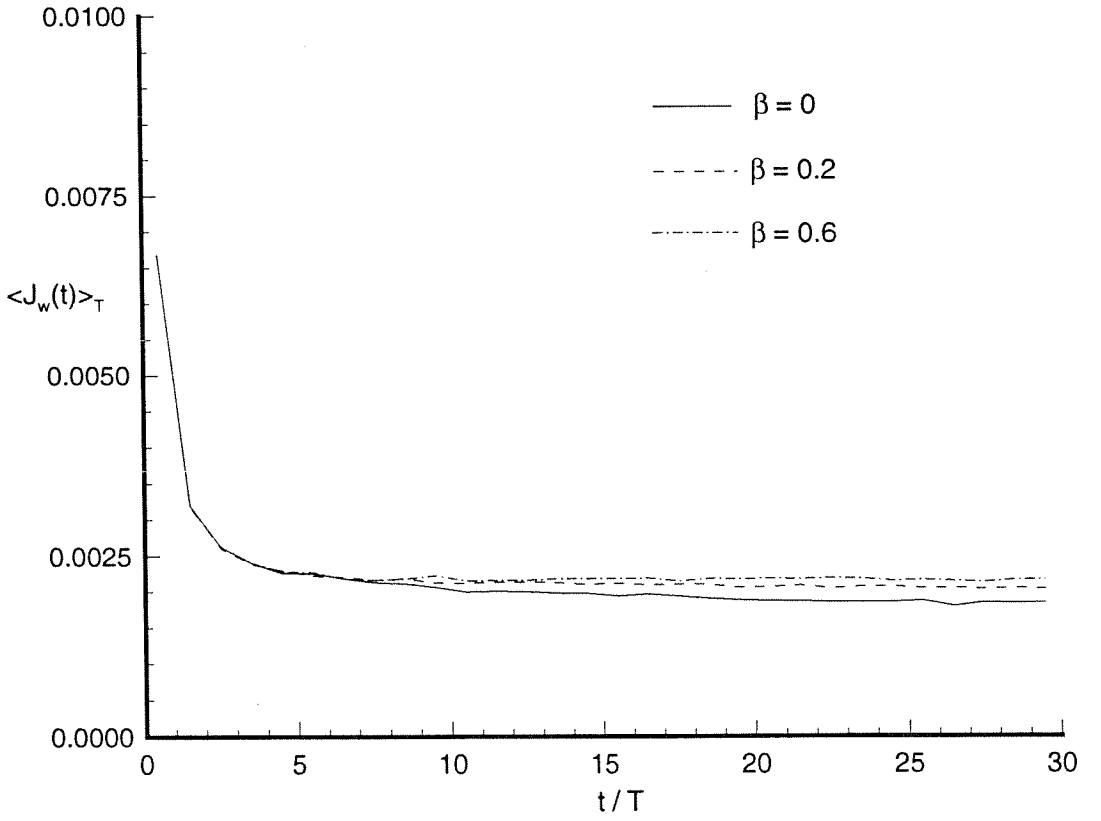
0.0100
0.0075
0.0050
0.0025
0.0000
<J_w(t)>_T
β = 0
β = 0.2
β = 0.6
0
5
10
15
20
25
30
t / T

Figure 3.12(a)

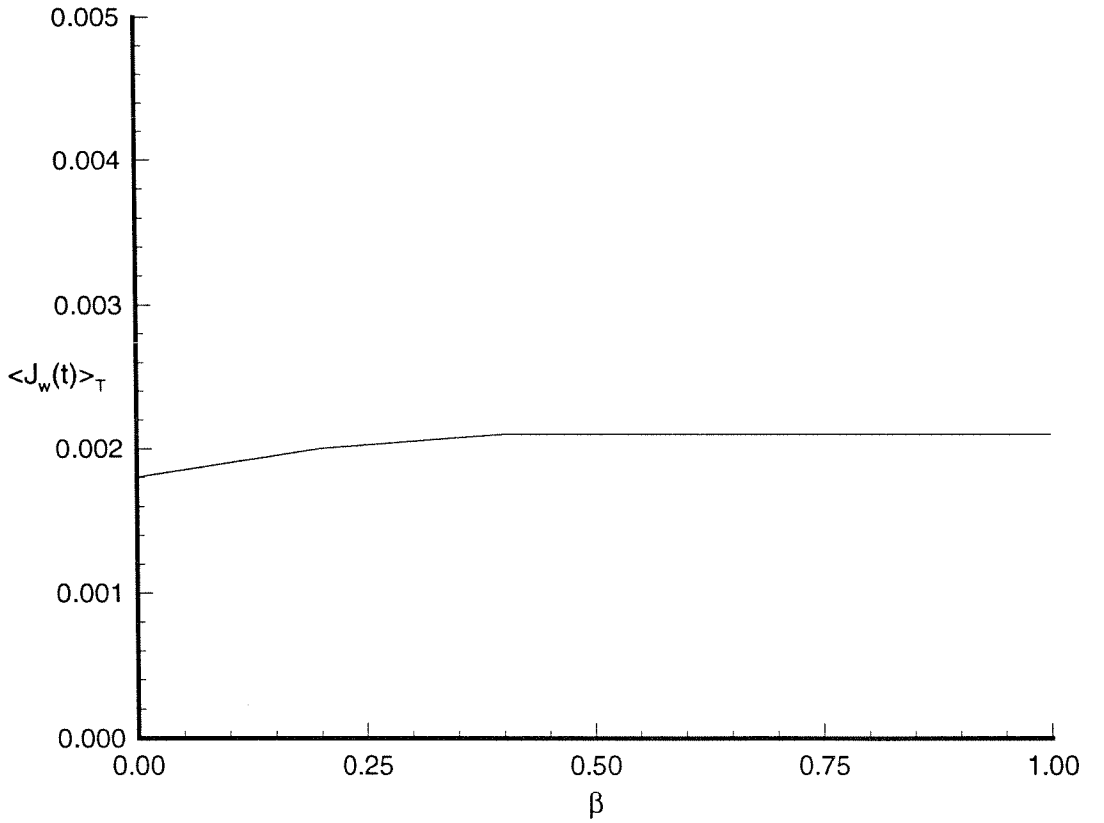

Figure 3.12(b)

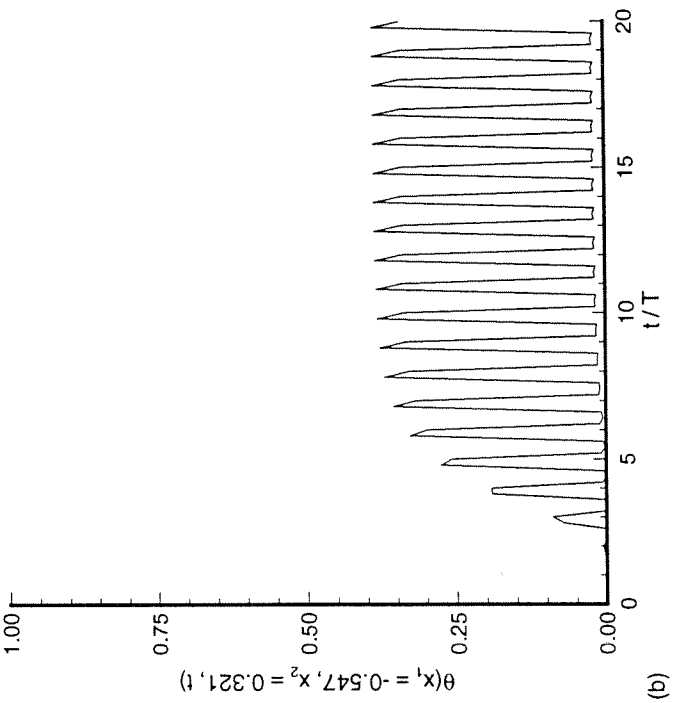

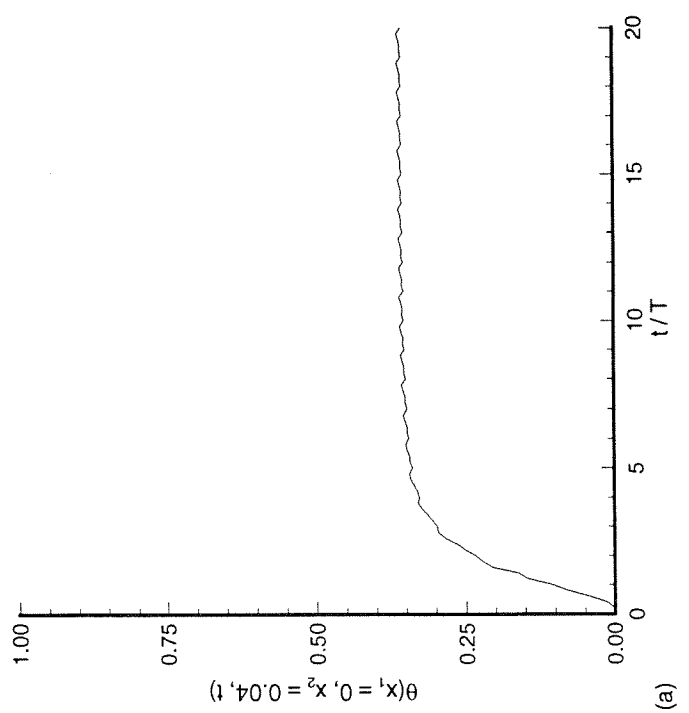

Figure 3.13(a,b)

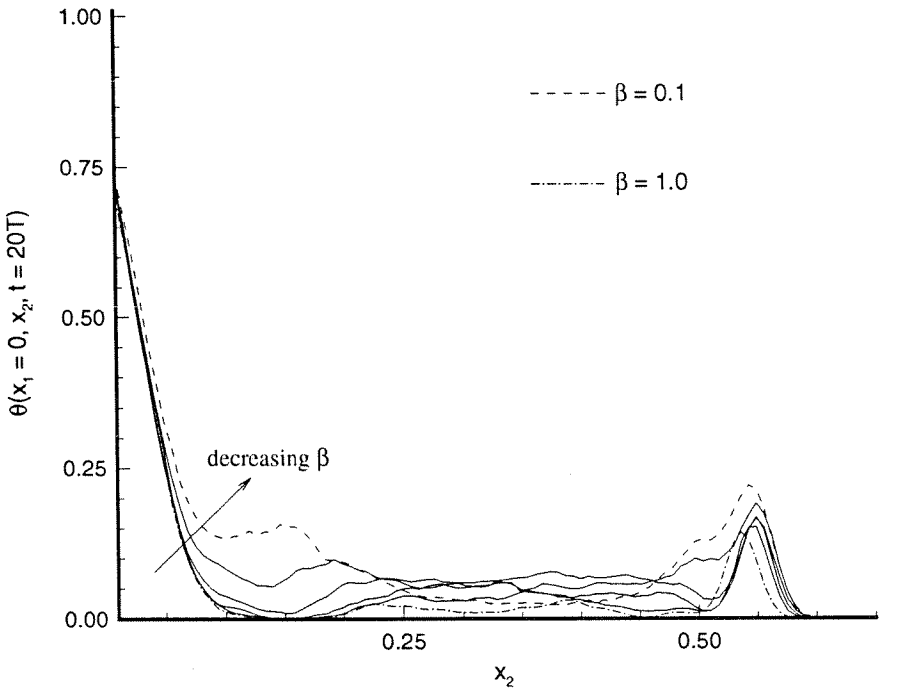
1.00
0.75
0.50
0.25
0.00
θ(x1 = 0, x2, t = 20T)
β = 0.1
β = 1.0
decreasing β
0.25
0.50
x2

Figure 3.14

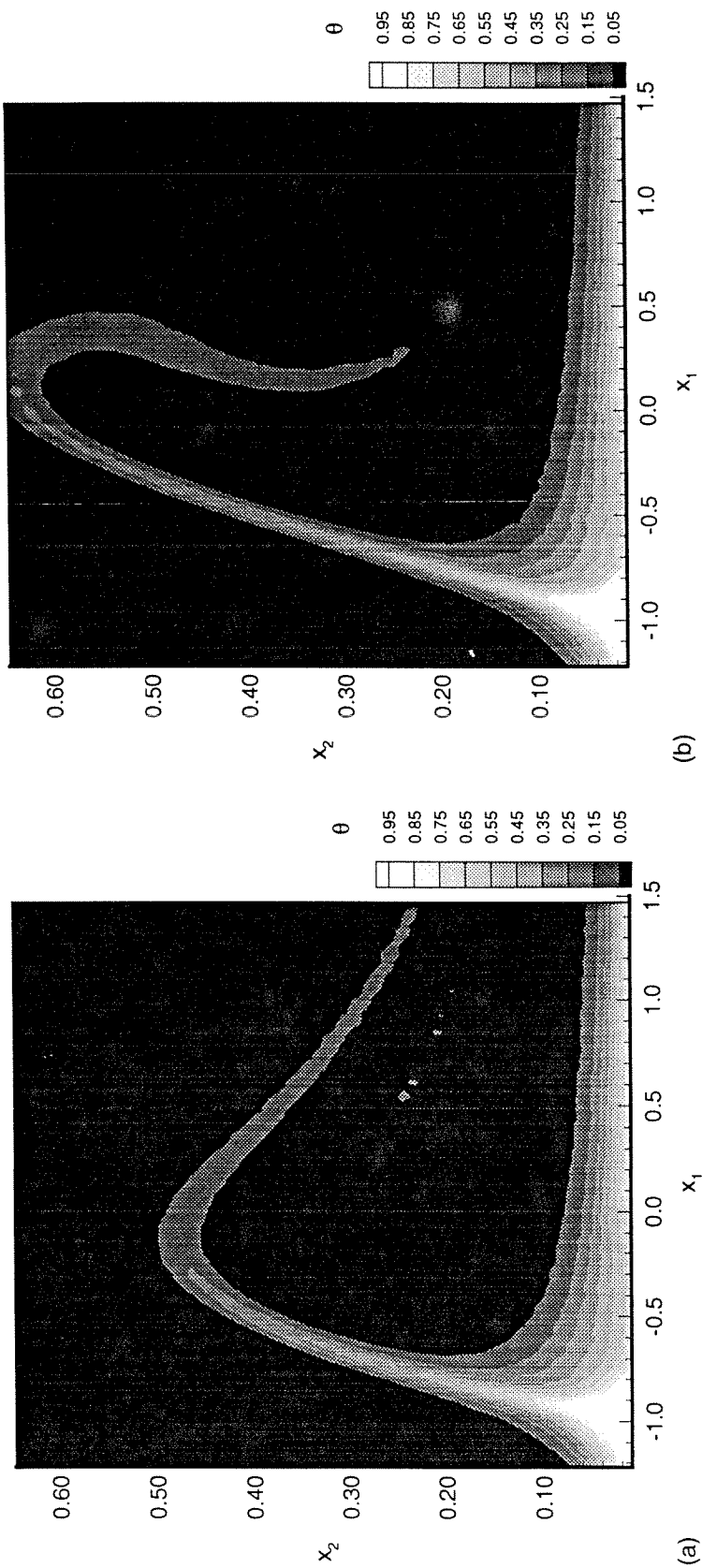

Figure 3.15(a,b)

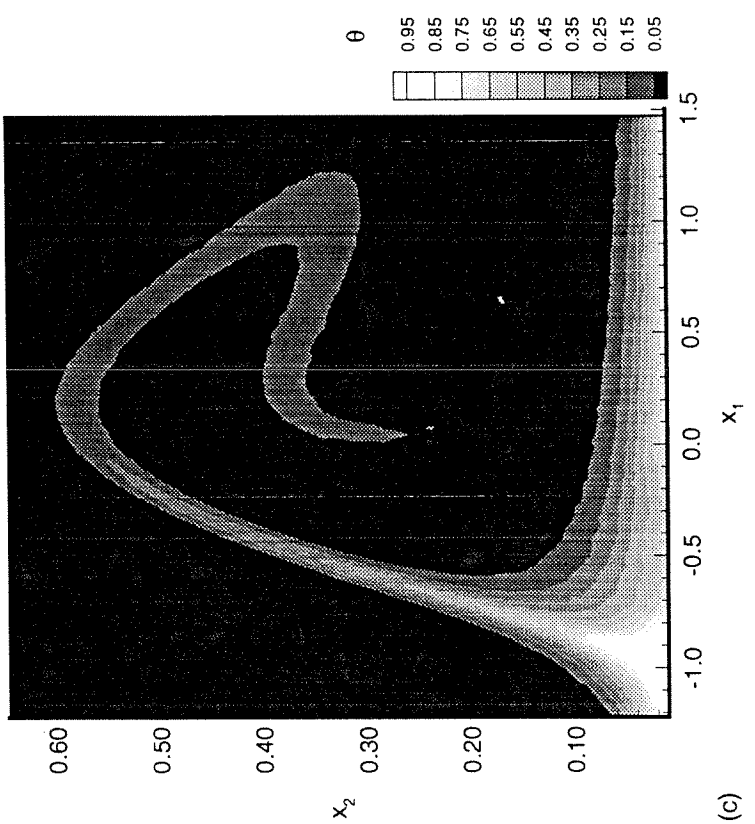
θ
0.95
0.85
0.75
0.65
0.55
0.45
0.35
0.25
0.15
0.05
0.60
0.50
0.40
0.30
0.20
0.10
x_2
-1.0
-0.5
0.0
0.5
1.0
1.5
x_1
(c)

Figure 3.15(c)

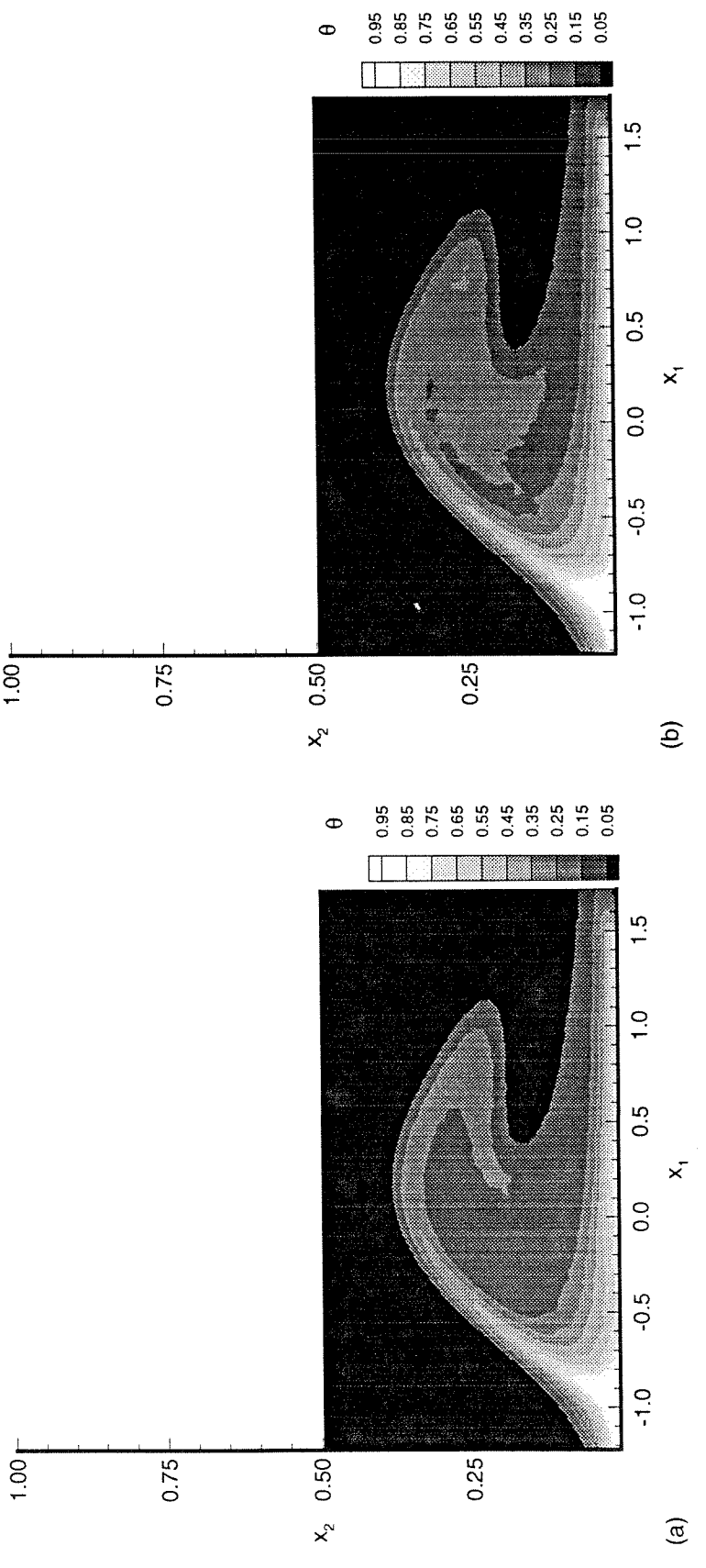

Figure 3.16(a,b)

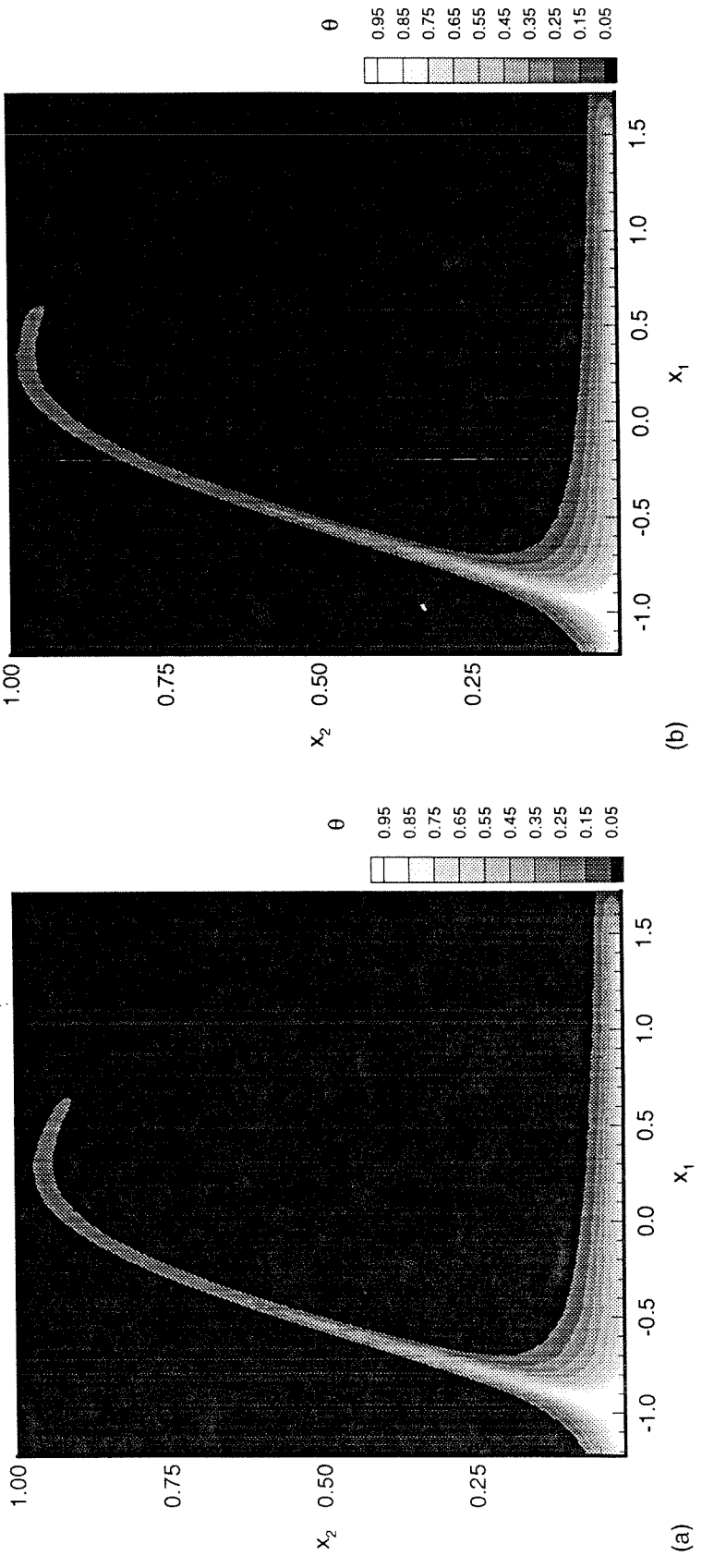

Figure 3.17(a,b)

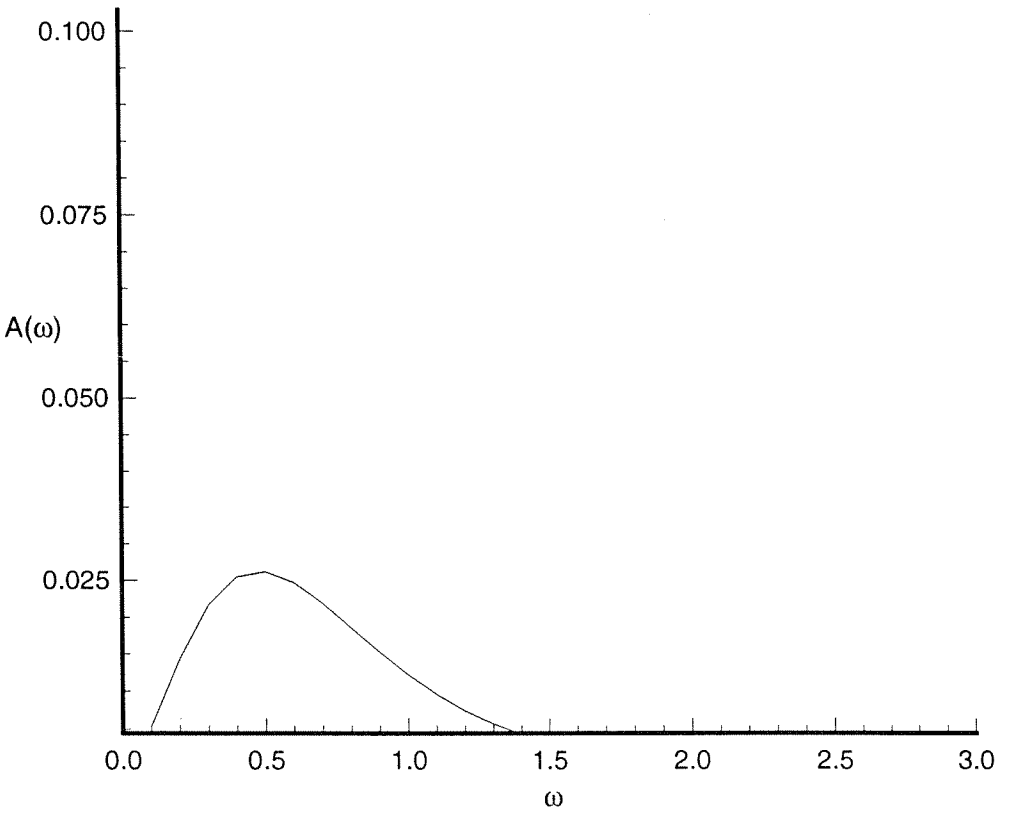

Figure 3.18(a)

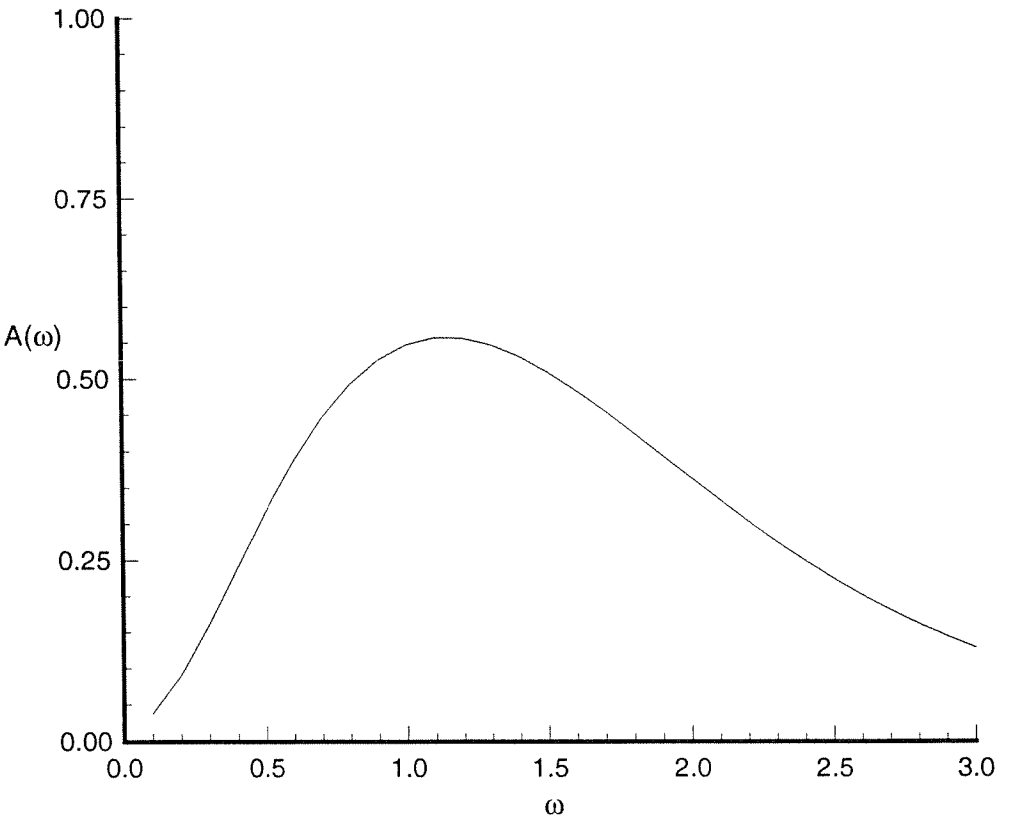

Figure 3.18(b)

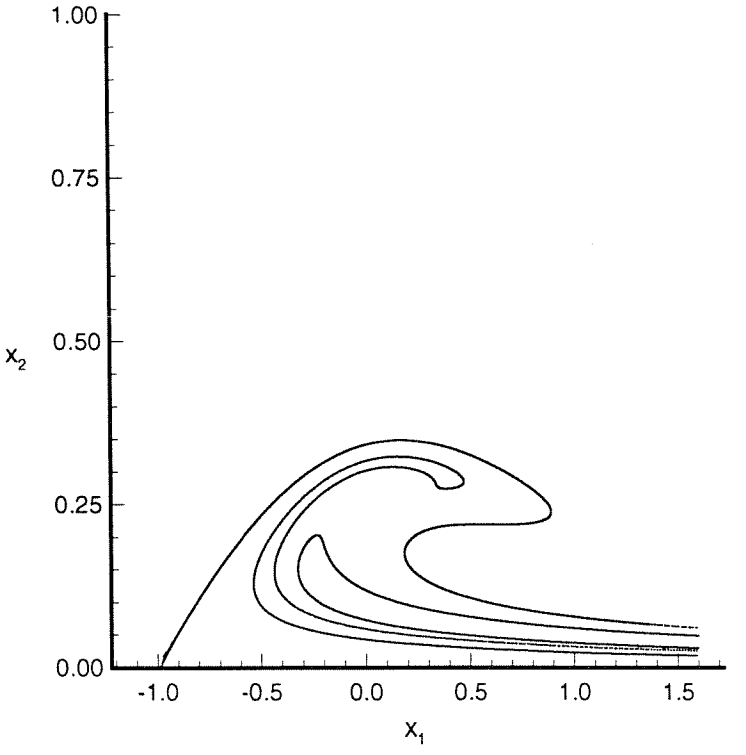

Figure 3.19

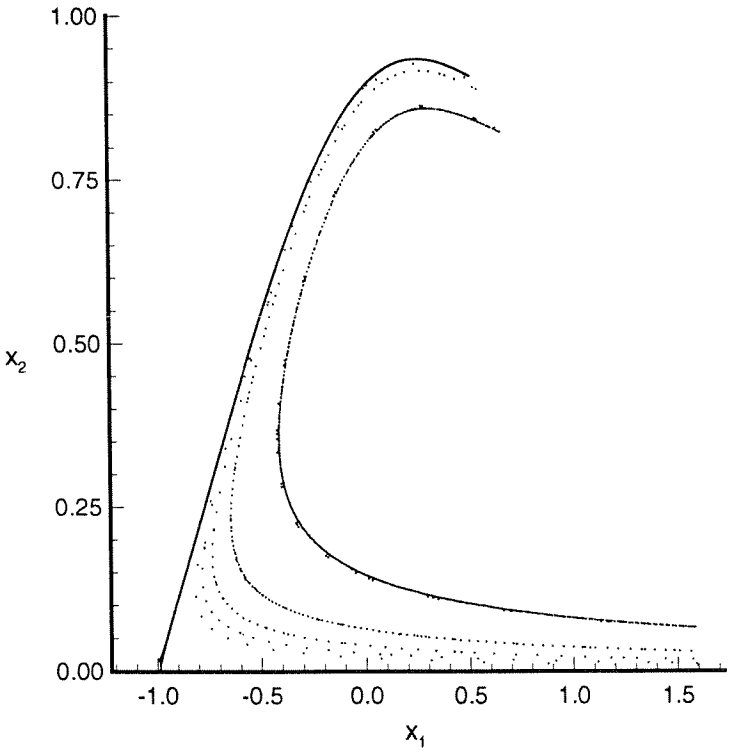

Figure 3.20

Chapter 4

The zero-diffusivity solution and its relation to the solution at small scalar diffusivity

Given some initial distribution of a scalar field one can construct a zero-diffusivity solution, also called the frozen-field solution, at any $t > 0$ by treating θ as a material invariant. It might be expected that the effect of small scalar diffusion is to smooth out any fine-scale structure in the zero-diffusivity solution. Recent work of Klapper (1992a) has contributed strongly towards this description. If small scalar diffusion does no more than smooth out the fine-variations in the zero-diffusivity solution, the distribution of the scalar field at small scalar diffusivity should retain the gross features of the zero-diffusivity solution. However, our problem is complicated by the fact that the zero-diffusivity solution, i.e., the solution of (3.1) at $Pe = \infty$, is trivially zero over the entire domain of the flow. We therefore interpret the zero-diffusivity solution in the following sense : for $Pe \to \infty$, Pe however large, there is always a boundary-layer near the active portion of the wall which is diffusively dominant and where diffusion may not be ignored. For $t = t_0$ sufficiently small, a solution in the boundary-layer is easily obtained, which is used as an "initial profile," $\theta(x, t = t_0)$, to obtain a "zero-diffusivity" solution in the rest of the

domain at $t > t_0$ by setting the scalar diffusivity to be exactly zero and treating θ as a material invariant for all $t > t_0$. The construction is artificial, but it proves to be a useful artifice in understanding not only the role of the unstable manifold as a organizing structure but also the role of small scalar diffusion as a local smoothing of fine-scale structure in the frozen field.

In the boundary-layer at the wall, for t sufficiently small the normal coordinate $x_2 < O(1)$ for all x_1. If the lateral coordinate x_1 is $O(1)$, the advective term in (3.1), $u.\nabla\theta$, is $O(x_2)$, and therefore there is a time t sufficiently small such that the advective term cannot match $\partial\theta/\partial t$ and will not contribute to dominant order. Moreover, for $x_2 << x_1$, diffusion in the normal direction dominates over diffusion parallel to the wall. Hence, at small t the dominant balance argument is straightforward : the transient term $\partial\theta/\partial t$ must be balanced by diffusion normal to the wall. In physical terms, for small t, in particular t so small that advection is negligible in comparison to transverse diffusion over a narrow boundary-layer at the wall, the advection-diffusion equation in the boundary-layer must reduce to a simple transient diffusion equation with solution $\theta(x_1, x_2, t)$ independent of the lateral coordinate x_1. We rescale time, $t \rightarrow Pe^{-\alpha}t$, $\alpha > 0$. Balancing appropriate terms in (3.1) gives $x_2 = O(Pe^{-(\alpha+1)/2})$. Rescaling the normal coordinate in the near-wall boundary-layer, $x_2 \rightarrow Pe^{-(\alpha+1)/2}x_2$ gives a simple transient diffusion equation, to dominant order :

$$\frac{\partial\theta}{\partial t} = \frac{\partial^2\theta}{\partial x_2^2},$$

with initial and boundary conditions

$$\theta(t \rightarrow 0) = 0,$$

$$\theta(x_2 \rightarrow 0) = 1,$$

$$\theta(x_2 \rightarrow \infty) = 0,$$

which has the familiar error function solution, expressed now in the unscaled coor-

dinates

$$\theta(x_1, x_2, t) = 1 - \frac{2}{\sqrt{\pi}} \int_0^{\frac{Pe^{1/2} x_2}{2\sqrt{t}}} e^{-s^2} ds. \tag{4.1}$$

The exact scaling factor α remains undetermined. The dominant balance argument is not expected to hold near the separation point p^- where advection is not dominantly parallel to the wall. But, for large Pe, this advection-diffusion regime will be of negligible size and may be ignored. Comparison with the exact Wiener bundle solution for $\beta = 0.6$, $\omega = 0.72$, and $Pe = 2.5 \times 10^4$ along the centerline ($x_1 = 0, x_2 > 0$) at several t (see figure 4.1) shows the error function solution of (4.1) tracks the time-evolution of the scalar field in the boundary-layer all the way up to about $t \approx 10$, but deteriorates rapidly at larger times.

Using the error function solution of (4.1) for $Pe = 2.5 \times 10^4$ and $t = t_0$ sufficiently small as the "initial distribution" $\theta(x, t = t_0)$, the "zero-diffusivity" solution is obtained at several $t > t_0$, excluding of course the thin near-wall boundary-layer-region (see figures 4.2, 4.3). Henceforth, it will be understood that by "zero-diffusivity" solution we mean $\theta(x, t > t_0)$ obtained using the "initial distribution" described above. It is evident from figures 4.2 and 4.3 that the initial distribution, which is confined to the near-wall region, is wrapped around $W^u_\beta(\bar{\phi})$ as time progresses; as usual the numerical results are obtained at $t = NT$ for several N, i.e., at times that are integral multiples of the period T of the velocity field, so that $\bar{\phi} = 0$ and comparisons can be made with W^u_β of figure 2.3. This result can be understood in simple terms by examining the dynamics of points in the near-wall region under forward iterations of the Poincaré map P_β. Consider the heteroclinic tangle formed by the intersections of W^s_β and W^u_β. If they intersect once, they must intersect a countably infinite number of times since their intersection points, called heteroclinic points (see Wiggins 1992), asymptote to the attachment point p^+ in forward time and to the separation point p^- in backward time, and therefore constitute a doubly

asymptotic set. Moreover, if they intersect transversely, there exists a countable infinity of transverse heteroclinic points. This is due to the fact that transversal intersections are preserved under diffeomorphisms and P_β, being the time-T map derived from a smooth flow, is a diffeomorphism. Hence the presence of the plane wall and the accumulation of transverse heteroclinic points close to p^-, in terms of arclength along W^u_β, forces segments of W^s_β to accumulate at the wall, giving rise to the familiar *trellis*-type structure studied originally by Poincaré (e.g., see Easton 1986). This is demonstrated by the heteroclinic tangle over the wall, obtained in figure 4.4 for $\beta = 0.6$, $\omega = 0.72$. Integration errors near the no-slip boundary makes resolution of the tangle difficult, but the afore-mentioned trellis-type structure of the tangle is clearly evident. Moreover, figure 4.4 provides numerical verification of transversal intersections of W^s_β and W^u_β, predicted analytically using the Melnikov function of (2.12). Now consider the countable infinity of transverse heteroclinic points p_i, $i \in Z$, that accumulate on p^- in the sense described above. As segments of W^s_β densely fill out the near-wall region $R_w \equiv (-1.5, 1-\epsilon_1) \times (0, \epsilon_2)$, $0 < \epsilon_1,\ \epsilon_2 << 1$, $\epsilon_1 \to 0$ as $\epsilon_2 \to 0$, every open neighborhood of any point in R_w has points lying on a segment of W^s_β or on the stable manifold through some p_i, where the stable manifold through p_i is the set of points that converge asymptotically to the trajectory of p_i under forward iterations of P_β. Since points on W^s_β converge asymptotically in forward time, and p_i's are mapped to transverse heteroclinic points under P_β, points in R_w are swept into a thin neighborhood of W^u_β under forward iterations of P_β, which accounts for the nature of the zero-diffusivity solution observed in figures 4.2, 4.3. Moreover, because of the asymptotic convergence of points on W^s_β, the zero-diffusivity solution will have a steep gradient in the *local stable direction* which, for a transverse heteroclinic point, is the direction of the tangent to W^s_β at that point and is complementary to the tangent direction of W^u_β

at that point. This is verified by extracting from figure 4.3 the scalar distribution in directions tangent and normal to W^u_β at a point $p \in W^u_\beta$, i.e. along $T_p(W^u_\beta)$ and $N_p(W^u_\beta)$, which are displayed in figure 4.5.

Thus the zero-diffusivity solution at $t > t_0$ pulls the boundary-layer distribution at $t = t_0$ into a narrow distribution along the unstable manifold of p^-, $W^u_\beta(\bar{\phi})$, where the variation of the scalar field along $W^u_\beta(\bar{\phi})$ is much smaller than in transverse directions. The physical picture arising from comparing figures 4.2(a,b), 4.3(a,b) with figures 3.3(a,b), 3.4(a,b) respectively is that the zero-diffusivity solution creates fine-scale structure that is confined to the vicinity of $W^u_\beta(\bar{\phi})$ and small scalar diffusion only smooths out the fine variations, thus allowing the unstable manifold to continue to be the dominant organizing structure everywhere except in a narrow diffusively-dominant near-wall boundary-layer. In the following section we develop an understanding of this qualitative picture using recent results (Klapper 1992a) based on the shadowing theory of chaotic hyperbolic sets.

FIGURES

Figure 4.1: Wiener bundle solutions at several points along the centerline ($x_1 = 0, x_2 > 0$) at several times and for $\beta = 0.6$, $\omega = 0.72$, $Pe = 2.5 \times 10^4$, are compared against the small-time analytical solution of (4.1) at the same Pe. Again, $T = 2\pi/\omega$ in figure.

Figure 4.2: The "zero-diffusivity" solution for $\beta = 0.6$, $\omega = 0.72$, using an "initial distribution" obtained at $Pe = 2.5 \times 10^4$, at (a) $t = 5T$, (b) $t = 10T$, $T = 2\pi/\omega$.

Figure 4.3: The "zero-diffusivity" solution for $\beta = 0.2$, $\omega = 0.72$, using an "initial distribution" obtained at $Pe = 2.5 \times 10^4$, at (a) $t = 5T$, (b) $t = 10T$, $T = 2\pi/\omega$.

Figure 4.4: Heteroclinic tangle near the wall for $\beta = 0.6$, $\omega = 0.72$.

Figure 4.5: Distribution of the scalar field at $t = 10T$ in the zero-diffusivity solution of figure 4.2 along (a) $T_p(W^u_\beta)$, (b) $N_p(W^u_\beta)$, $p = (-0.547, 0.321) \in W^u_\beta$. The point p is plotted in figure 2.3(a).

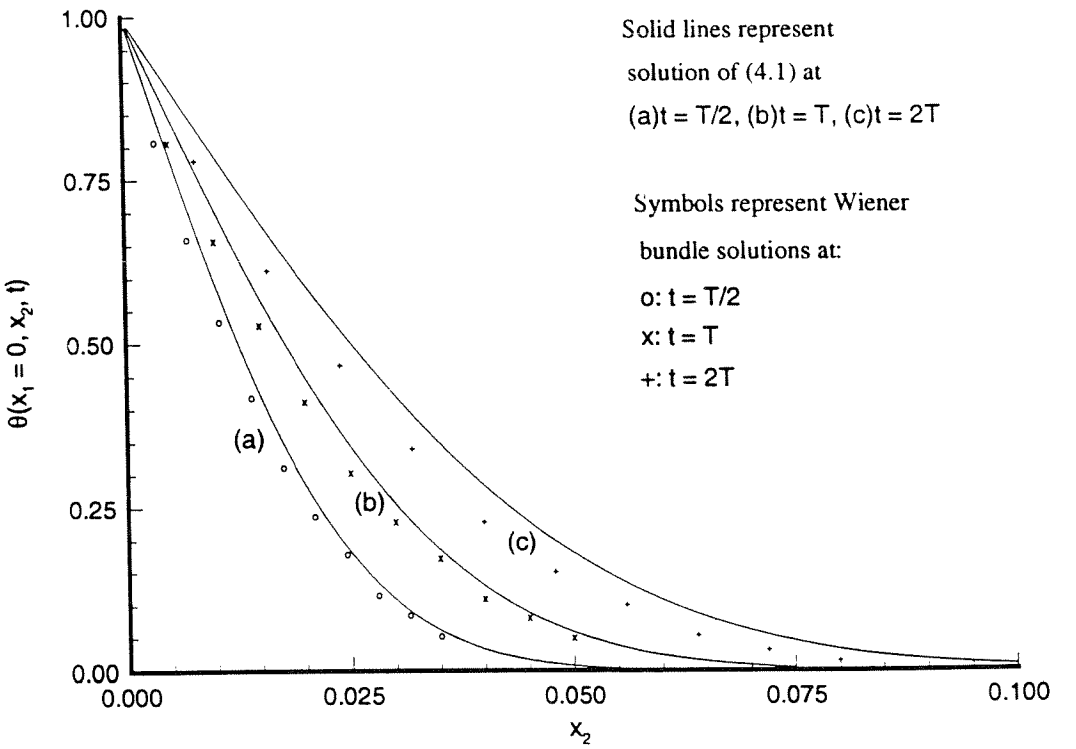
1.00
0.75
0.50
0.25
0.00
0.000
0.025
0.050
0.075
0.100
$\theta(x_1 = 0, x_2, t)$
x_2
(a)
(b)
(c)
Solid lines represent
solution of (4.1) at
(a)t = T/2, (b)t = T, (c)t = 2T
Symbols represent Wiener
bundle solutions at:
o: t = T/2
x: t = T
+: t = 2T

Figure 4.1

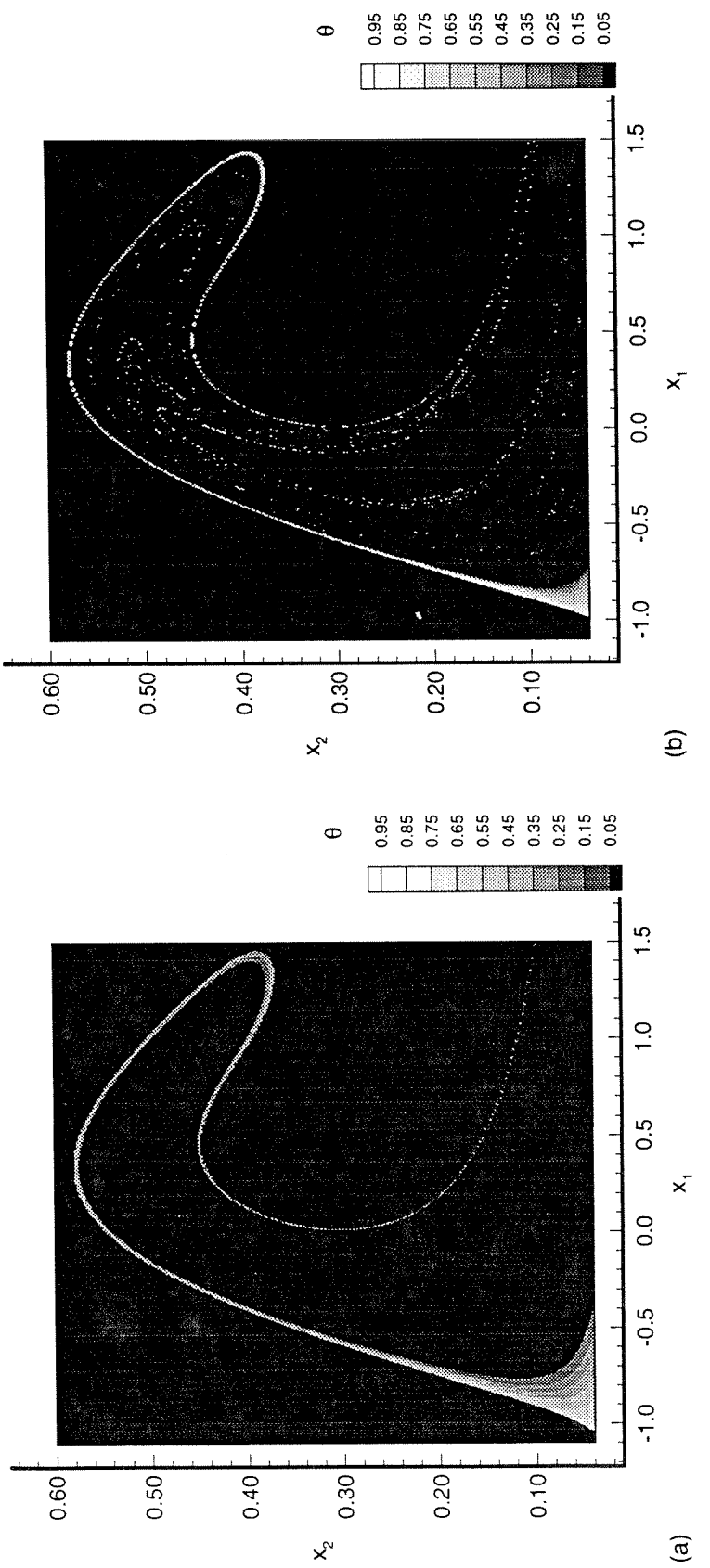
θ
0.95
0.85
0.75
0.65
0.55
0.45
0.35
0.25
0.15
0.05
0.60
0.50
0.40
0.30
0.20
0.10
x_2
-1.0
-0.5
0.0
0.5
1.0
1.5
x_1
(a)
(b)

Figure 4.2(a,b)

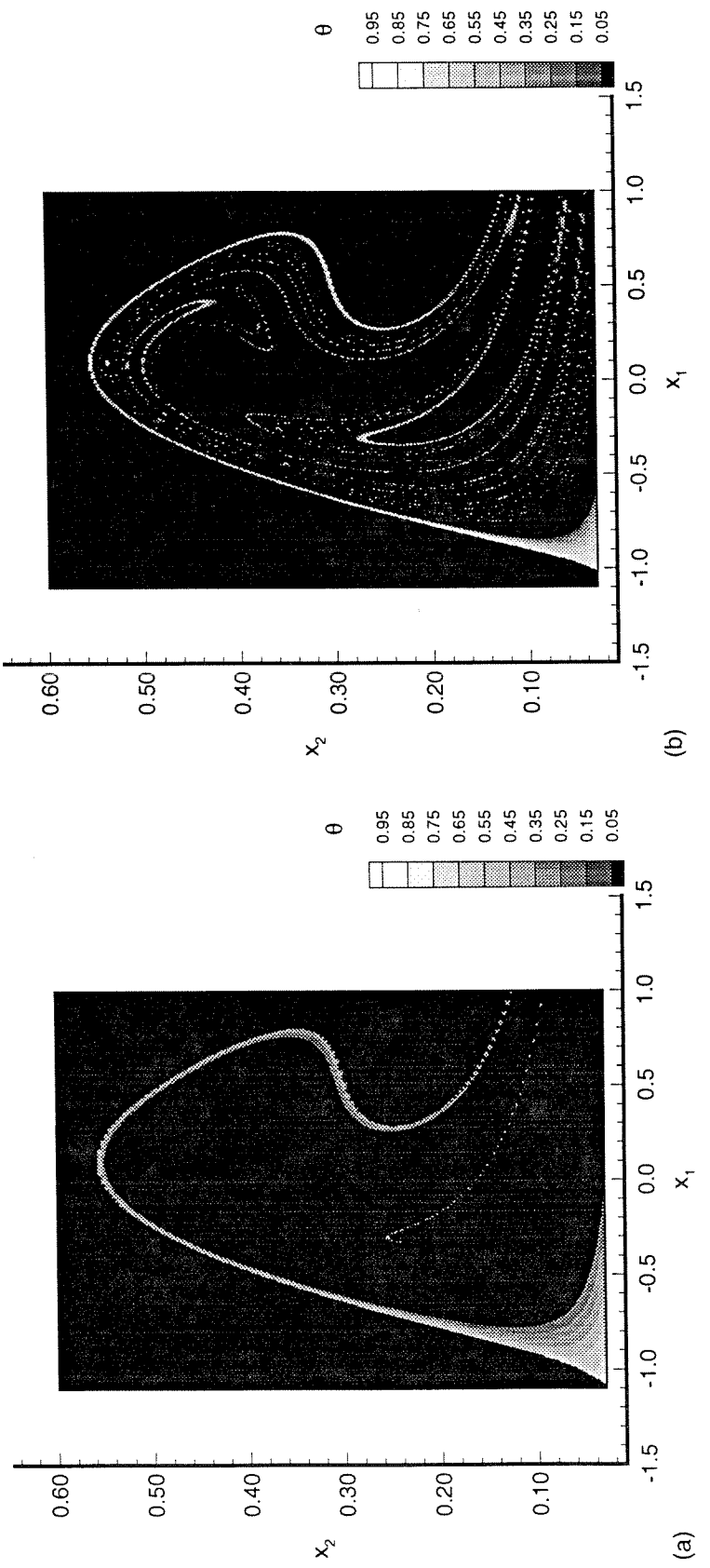
θ
0.95
0.85
0.75
0.65
0.55
0.45
0.35
0.25
0.15
0.05
0.60
0.50
0.40
0.30
0.20
0.10
x_2
-1.5
-1.0
-0.5
0.0
0.5
1.0
1.5
x_1
(a)
(b)

Figure 4.3(a,b)

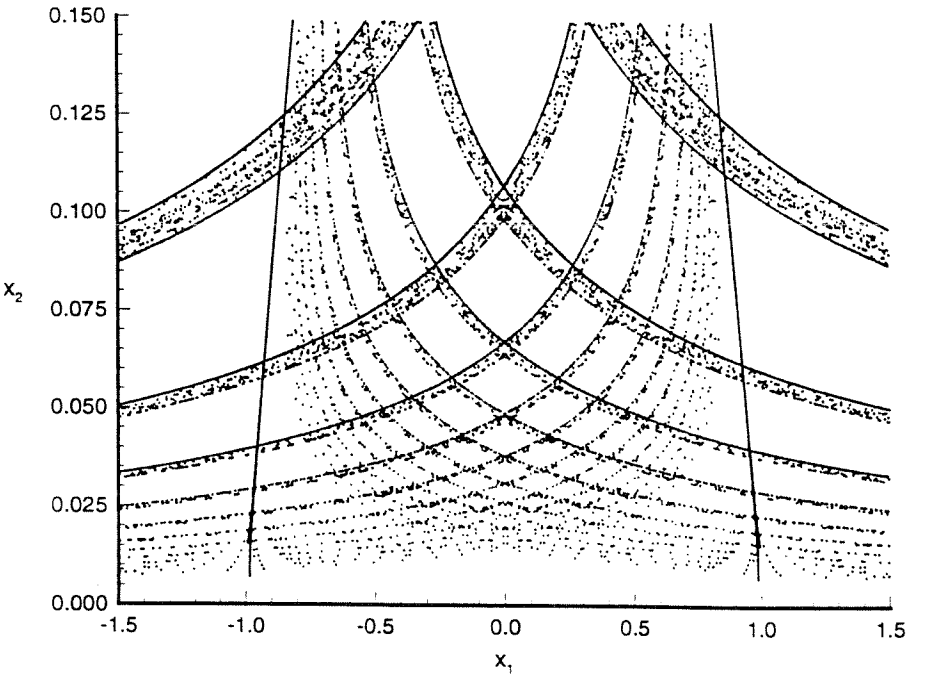

Figure 4.4

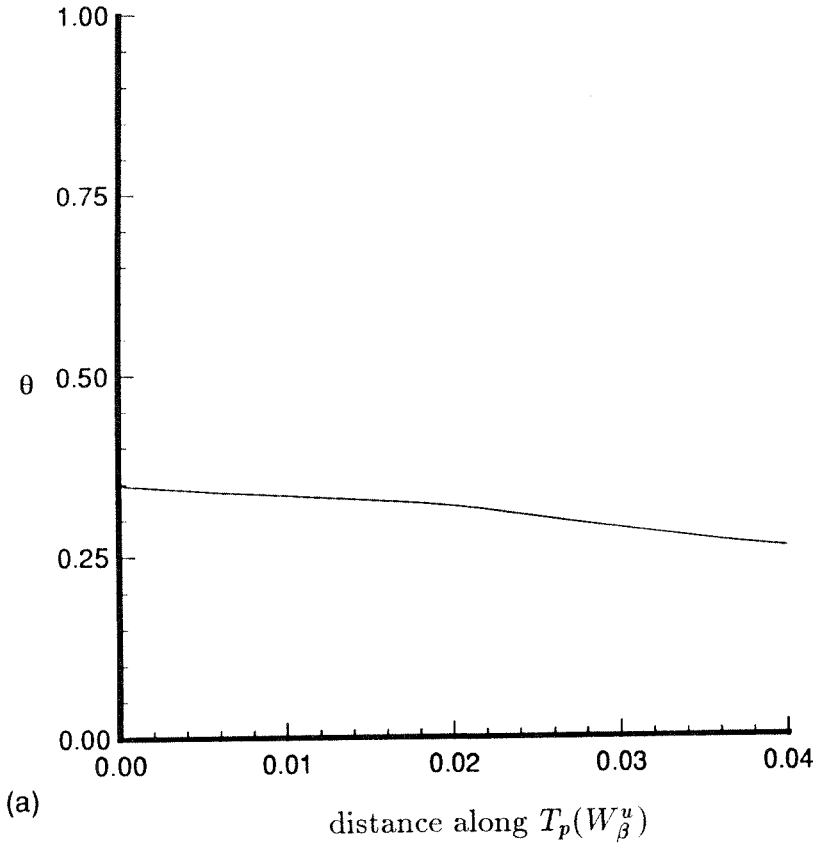
1.00
0.75
θ 0.50
0.25
0.00
0.00
0.01
0.02
0.03
0.04
(a)
distance along $T_p(W^u_\beta)$

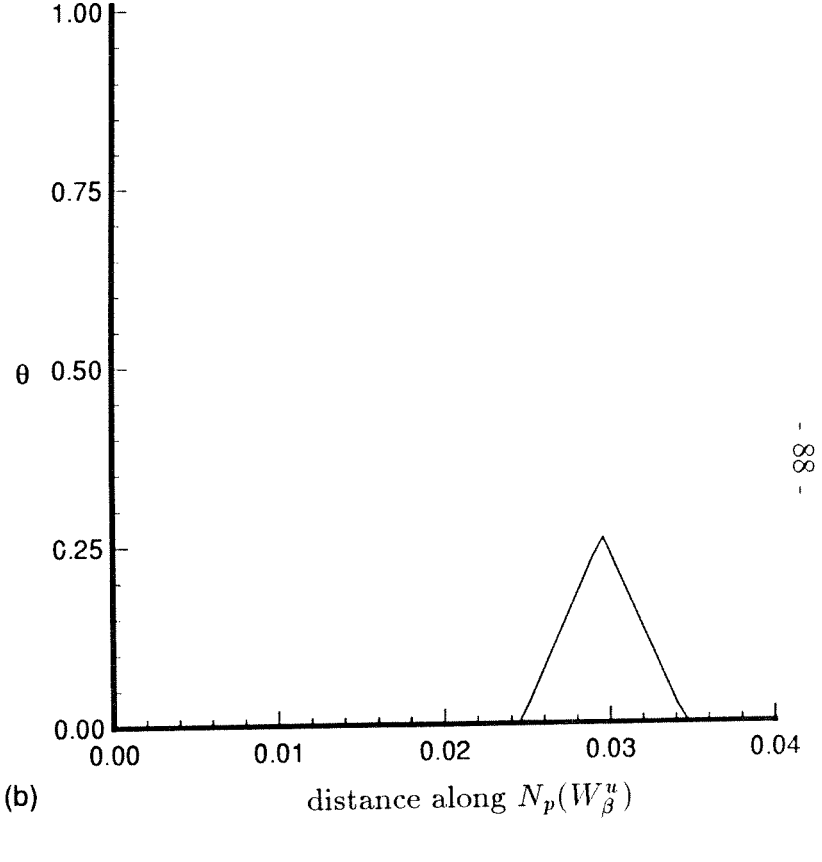
1.00
0.75
θ 0.50
0.25
0.00
0.00
0.01
0.02
0.03
0.04
(b)
distance along $N_p(W^u_\beta)$

Figure 4.5(a,b)

Chapter 5

Application of shadowing theory to the small diffusivity problem

Shadowing (Anosov 1967, Bowen 1975) is one of the fundamental properties of hyperbolic sets of C^r ($r \geq 1$) diffeomorphisms. For a two-dimensional diffeomorphism $f : \mathbb{R}^2 \to \mathbb{R}^2$, a compact invariant subset $\Lambda \subset \mathbb{R}^2$ is a hyperbolic set or is said to have a hyperbolic structure if every $p \in \Lambda$ has a stable and unstable direction with the angle between them uniformly bounded away from zero, such that a point that is away from p by an infinitesimal displacement in the stable direction will converge exponentially fast to the trajectory through p in forward time, or forward iterations under f; the same holds in backward time for a point that is away from p by an infinitesimal displacement in the unstable direction. Moreover, the local stable and unstable directions vary continuously with $p \in \Lambda$. Thus, every $p \in \Lambda$ has a stable and unstable manifold, where the stable manifold is the set of points that converge exponentially as time goes to infinity, and the unstable manifold is the set of points that converge exponentially as time goes to negative infinity. Formally, the hyperbolic set Λ can be defined in terms of an invariant continuous splitting of the tangent bundle of $\mathbb{R}^2$ restricted to Λ, under the global derivative map Df, into

contracting and expanding sub-bundles; for precise definition and terminology, see Smale (1967). The shadowing lemma (Bowen 1975) states that for each $\delta > 0$ there is an $\epsilon > 0$, such that every trajectory $\{x^i\}_{i=n}^{m}$ in Λ satisfying $|x^{i+1} - f(x^i)| < \epsilon$ for all $n \leq i \leq m$ (called an ϵ-pseudo-orbit) is δ-traced by an exact trajectory $\{y^i\}_{i=n}^{m}$ in Λ (called the shadowing trajectory), i.e., $y^{i+1} = f(y^i)$ and $|x^i - y^i| \leq \delta$ for all $n \leq i \leq m$, where $n = -\infty$ and $m = +\infty$ is permitted. For $\Lambda \subset \mathbb{R}^2$, $|\cdot|$ can be taken to be the standard Euclidean norm on the plane. The result would appear to be useful only in the special case of uniformly hyperbolic or everywhere hyperbolic (Farmer & Sidorowich 1991) dynamical systems, also called Anosov dynamical systems, in which at each point the dynamics can be factored into local stable and unstable directions and the stable and unstable manifolds always intersect transversely, i.e., there are no *homoclinic tangencies* (Farmer & Sidorowich 1991). However, work of Klapper (1992a) has indicated that making the assumption that shadowing property holds in non-uniformly hyperbolic systems such as ours can lead to useful insights into the small-diffusivity scalar advection-diffusion problem. To what extent such an assumption is reasonable is discussed below.

It is now well known that the transversal intersection of stable and unstable manifolds of a hyperbolic fixed point for a $C^r (r \geq 2)$ diffeomorphism $f : \mathbb{R}^2 \to \mathbb{R}^2$ implies the existence of Smale horseshoes, which are invariant hyperbolic sets on which the dynamics is chaotic. This is a consequence of the Smale-Birkhoff homoclinic theorem (e.g., see Wiggins 1992). For heteroclinic orbits, if the heteroclinic points and their stable and unstable manifolds form a heteroclinic cycle (Wiggins 1992) then the Smale-Birkhoff homoclinic theorem applies directly, implying the existence of horseshoe-like dynamics. These conditions are not met in our problem because of the non-hyperbolic character of points on the no-slip boundary; consequently, the existence of chaotic hyperbolic sets cannot be concluded directly from

existing theorems. While Poincaré maps of the time-periodic velocity field of (2.9) do indicate highly irregular particle motion in the bubble-region, it does not amount to a mathematical justification of chaotic dynamics of the Smale-horseshoe type, which seems difficult at this time. But even in flow systems in which a horseshoe construction is explicit, since the invariant hyperbolic sets associated with Smale horseshoes occupy regions of measure zero, the shadowing lemma, which applies strictly to orbits on the hyperbolic set, would appear to be of very limited use in applications. However, there is reason to believe that nearby orbits also share some of the hyperbolic character since there is fair amount of numerical evidence that chaotic processes, which generically have homoclinic tangencies and are therefore not uniformly hyperbolic, do have the shadowing property (Hammel *et al.* 1987, 1988, Grebogi *et al.* 1990). In our system we therefore expect the shadowing property to hold in regions of the flow where there is chaotic particle motion which, for even moderately large perturbation amplitude β, includes most of the bubble-region except a thin near-wall region where the dynamics is regular at even large β.

Shadowing theory was originally (Anosov 1967, Bowen 1975) developed for diffeomorphisms, and to apply the theory to our continuous-time advection-diffusion process the problem is cast in a diffeomorphism-framework. We consider a discrete-time formulation in which instantaneous advection, given by the Poincaré map $P_\beta^{\bar{\phi}}$, is alternated with pulses of diffusion over time T. Therefore, a diffusive tracer located at x^0 at initial time t_0 is advanced according to

$$x^{n+1} = f(x^n) + \rho_T, \ n = 0, 1, \ldots \quad , \tag{5.1}$$

with $\rho_T \equiv (\eta_T, \xi_T)$, where η_T, ξ_T are Gaussianly distributed random variables, each with mean zero and variance $2T/Pe$, diffeomorphism $f \equiv P_\beta^{\bar{\phi}}$, and the cross-section $\bar{\phi}$ is determined by $\bar{\phi} = \omega t_0 \pmod{2\pi}$. Since the kinematics of a diffusive tracer is governed by the stochastic differential of (3.3), the justification for using (5.1) is

not immediately obvious, particularly because the period T of the velocity field is not necessarily small. First, however, we address the motivation for using (5.1). In a discrete random-walk approximation of (3.3), a diffusive tracer located at x^0 at initial time t_0 is advanced according to

$$x^{n+1} = g_{n+1}(x^n) + \rho, \ n = 0, 1, \ldots \ , \tag{5.2}$$

with $\rho = (\eta, \xi)$, where η, ξ are Gaussianly distributed random variables as in (3.4), and the g_n's are obtained by noting the position of particles in the flow at every infinitesimally small time-step Δt; for $t_0 = 0$, (5.2) is identical to (3.4) with $g_{n+1} = (x_1^n + \Delta x_1^n, x_2^n + \Delta x_2^n)$. Notice that in the smooth time-dependent flow $u(x,t)$ a perfect or non-diffusive tracer is mapped according to $x^{n+1} = g_{n+1}(x^n)$, and though the g_n's are C^∞ diffeomorphisms, a deterministic orbit is now given by a *sequence* of discrete maps. By choosing $\Delta t = T$, the deterministic "jumps" are given by the C^∞ diffeomorphism f instead of a sequence of diffeomorphisms and (4.2) is replaced by (4.1), which puts the advection-diffusion problem in a more convenient framework. In Appendix D, we show that in the limit of infinite Pe or zero scalar diffusivity, the discrete random processes generated by (5.1) and (5.2) converge in the mean-square sense (at every $t = nT + t_0$), and thus (5.2) can be replaced by (5.1) at small diffusivities with asymptotically small error, which justifies the discrete formulation of (5.1). We note that Chow, Lin & Palmer (1989) have extended the proof of the shadowing lemma to hyperbolic sets of sequences of C^1 maps that are even not necessarily diffeomorphisms. We could therefore just as well work with the discrete formulation of (5.2) instead of (5.1), but it complicates both the notation and the computations without adding any new physical insight to the problem. Supporting numerical evidence to this end is also presented at the beginning of §5.2. In what follows, we proceed with the more convenient formulation of (5.1).

5.1 Scalar advection-diffusion in an uniformly hyperbolic system

In what follows, we assume that the dynamics at every point can indeed be factored into a stable and unstable direction. Consider then a diffusive tracer located at x^N and traveling backwards under (5.1), i.e.,

$$x^{n-1} = f^{-1}(x^n) + \rho_T, \quad n \in [1, N]. \tag{5.3}$$

Therefore (5.3) generates a bundle or cloud of Wiener trajectories, each of which starts at a random "Wiener initial point" x^0 at iteration zero or $t = t_0$ and arrives at the fixed non-random point x^N in N forward iterations. Now, every Wiener trajectory generated by (5.3) has a noisy deviate ρ_T at each iterate which is typically $O((T/Pe)^{1/2})$. Because of the Gaussian tail, ρ_T can become unbounded in some realizations, but the probability of such an event can be made arbitrarily small for any finite number of realizations by taking Pe large enough and thus forcing the variance of the noisy deviates to be as small as desired. More precisely, given an $\epsilon > 0$, choosing Pe sufficiently large ensures that the sample paths of (5.3), with probability arbitrarily close to unity, have noisy deviates that are bounded from above by ϵ at every time-step over finite time-intervals. Therefore, at large Pe *almost all* Wiener trajectories $\{x^n\}_{n=N}^0$ generated by (5.3) are ϵ-pseudo-orbits, and these will be shadowed as long as the trajectory is confined to regions of the flow where the shadowing property holds. Notice the difficulty in extending the argument to infinite times : as $N \to \infty$, every Wiener trajectory will, with probability one, experience a large noise event even at arbitrarily large Pe and cannot be shadowed. However, it is irrelevant to our problem since we are interested in only finite-time results. Recall from (3.8) that computing the Wiener bundle solution for the scalar value at the point x^N at time t requires taking an expectation over this bundle of

Wiener trajectories. Since the exact distribution of Wiener trajectories is difficult to obtain in an arbitrary flow, the method might seem to offer little additional insight. However, chaotic flows with the shadowing property and the associated hyperbolic structure provide a means of representing the distribution of Wiener trajectories in terms of exact shadow trajectories in a convenient way (Klapper 1992a).

Consider the Wiener trajectory $\{x^n\}_{n=N}^0$ generated using (5.3). The first noisy backward iterate of x^N is $O((T/Pe)^{1/2})$ close to $f^{-1}(x^N)$. In the next backward iterate, the component of x^{N-1} in the local unstable direction of $f^{-1}(x^N)$ is contracted exponentially under f^{-1} and therefore x^{N-2} remains $O((T/Pe)^{1/2})$ close to the stable manifold of $f^{-2}(x^N)$. Continuing in this way, the N^{th} noisy backward iterate of x^N, x^0 is $O((T/Pe)^{1/2})$ close to the stable manifold through $f^{-N}(x^N)$, which is also the N^{th} preimage of the stable manifold through x^N. Denoting the stable manifold through x^N as $W^s(x^N)$, the hyperbolic structure of the dynamics pulls the cloud of Wiener trajectories released at x^N into a $O((T/Pe)^{1/2})$ neighborhood (which can be imagined as a tube or sausage of thickness $O((T/Pe)^{1/2})$) of $f^{-N}(W^s(x^N))$ in N backward time-steps. The observation is crucial and was first made by A.D. Gilbert (see Klapper 1992b). From (3.8), the Wiener bundle solution at x^N at time $t = NT + t_0$ is therefore an appropriately weighted average of the initial field distribution $\theta(x, t_0)$ in a $O((T/Pe)^{1/2})$ neighborhood of the N^{th} preimage of the stable manifold through x^N. If $\theta(x, t_0)$ is continuous, assuming all Wiener initial points, i.e., the x^0's, lie on $f^{-N}(W^s(x^N))$ causes an error of $O((T/Pe)^{1/2})$ in $\theta(x^N, t = NT + t_0)$, and can be ignored. Thus the assumed hyperbolic structure of the dynamics leads to an important dimensional reduction in the problem, since obtaining the Wiener bundle average of (3.8) now requires computing the distribution of Wiener initial points in terms of arclength along the one-dimensional manifold $f^{-N}(W^s(x^N))$. Note, however, that the variance of this distribution can be $O(1)$;

due to the fast (asymptotically exponential) convergence of points on the stable manifold in forward time, the noisy *backward* iterates x^{N-n} can quickly move an $O(1)$ distance away from $f^{-n}(x^N)$ in terms of arclength along $f^{-n}(W^s(x^N))$, even for very large Pe. Therefore, the averaging might have to be carried out over a $O(1)$ length of $f^{-N}(W^s(x^N))$. But, since $f^{-N}(W^s(x^N))$ is not an embedding in $\mathbb{R}^2$ it is not a submanifold of $\mathbb{R}^2$ and can be a very complicated geometric object, in which case no major simplification is achieved. The shadowing property offers a way around this problem. From the shadowing lemma and our discussion above, almost every Wiener trajectory is δ-shadowed by an exact trajectory and δ can be chosen arbitrarily small provided Pe is sufficiently large. A Wiener trajectory $\{x^n\}_{n=N}^0$ and the corresponding exact shadow trajectory $\{y^n\}_{n=N}^0$ will pick up the same scalar value to $O(\delta)$ and therefore the contribution to the Wiener bundle average of (3.8) by $\theta(x^0, t_0)$ can be replaced by $\theta(y^0, t_0)$ with asymptotically small error. It should be clear that the y^0 must lie on $f^{-N}(W^s(x^N))$; otherwise, since the component in the unstable direction is exponentially expanded in forward time, forward iterates of y^0 (under the deterministic map, f) will move quickly away from the preimages of the stable manifold through x^N and cannot remain close to $\{x^n\}_{n=N}^0$. The advantage gained is the following : the distribution of Wiener initial points over $f^{-N}(W^s(x^N))$ can be mapped back to $W^s(x^N)$ under f^N, since the Wiener trajectories can be replaced by exact trajectories of f^N to $O(\delta)$, yielding the appropriate weighting law for averaging the *zero-diffusivity solution* over $W^s(x^N)$. Since points on $f^{-N}(W^s(x^N))$ converge exponentially under f^N as $N \to \infty$, the variance of the distribution over $f^{-N}(W^s(x^N))$ is also asymptotically exponentially contracted under f^N, which is an important simplification since $W^s(x^N)$ can be replaced by a straight line $E^s(x^N)$ in the local stable direction at x^N. Therefore, the Wiener bundle average of the initial field $\theta(x, t_0)$ over a $O((T/Pe)^{1/2})$ neighborhood

of $f^{-N}(W^s(x^N))$ is asymptotically replaced by a properly weighted average of the zero-diffusivity solution over $E^s(x^N)$ in the Wiener bundle solution of (3.8) at x^N at $t = NT + t_0$. Klapper (1992a) showed that the asymptotic ($Pe \to \infty$) weighting law for averaging the zero-diffusivity solution over $E^s(x^N)$ is Gaussian, with zero mean and variance

$$\sigma_N^2 = \frac{2T}{Pe} \sum_{n=1}^{N} \left(\frac{1}{\lambda_n} \right)^2, \tag{5.4}$$

where $\lambda_n > 1$ is the expansion factor of f^{-n} along the local stable direction at x^N. The λ_n's are easily expressed in terms of the local expansion rates at every iterate. Let f_n be the restriction of f^{-1} to $W^s(f^{-n+1}(x^N))$ and introduce $F_n = f_n \circ f_{n-1} \circ \cdots \circ f_1$; F_n maps $W^s(x^N)$ onto $W^s(f^{-n}(x^N))$. Then λ_n is simply

$$\begin{aligned} \lambda_n \equiv dF_n\Big|_{x^N} &= df_n\Big|_{f^{-n+1}(x^N)} \circ df_{n-1}\Big|_{f^{-(n-1)+1}(x^N)} \circ \cdots \circ df_1\Big|_{x^N}, \\ &= \beta_n \circ \beta_{n-1} \circ \cdots \circ \beta_1, \end{aligned}$$

where $\beta_i = df_i\Big|_{f^{-i+1}(x^N)}$ is the expansion factor of f^{-1} in the local stable direction of $f^{-i+1}(x^N)$.

5.2. Shadowing in the chaotic separation bubble

In figure 5.1(a) 10^4 Wiener trajectories starting at $p_1 = (0.25, 0.455)$ are generated using (5.3) by advancing backward in time up to a length of time $5T$, for $\beta = 0.6$, $\omega = 0.72$, and $Pe = 10^6$, to obtain the distribution of Wiener initial points in the domain of interest, which is the bubble-region or the flow region above the active portion of the wall. An equal number of points is distributed uniformly along the stable direction at p_1 up to a length 3σ on either side of p_1, where σ is the standard deviation of the Gaussianly distributed shadowing trajectories, computed for the same parameter values as above, using (5.4). These are integrated backwards up to a length of time $5T$ using the velocity field of (2.9) to obtain the preimage of the stable manifold through p_1,and is shown in figure 5.1(b). It is evident that most

of the mass of the distribution of Wiener initial points is confined to a small neighborhood of the preimage of the stable manifold through p_1. These results illustrate the usefulness of the shadowing property. We check below how this compares with shadowing in the discrete formulation of (5.2).

In figure 5.2(a) 10^4 Wiener trajectories starting again at the point p_1 are generated using

$$x^{n-1} = g_n^{-1}(x^n) + \rho, \tag{5.5}$$

with time-step $\Delta t = 0.2$ and up to a length of time $5T$, for $\beta = 0.6$, $\omega = 0.72$, and $Pe = 10^6$. Both the g_n's and ρ are same as in (5.2) and are now evaluated for time-step $\Delta t = 0.2$. Consider now the Wiener backward trajectory $\{x^n\}_{n=N}^0$ generated using (5.5). Denoting $g_{N-(n-1)}^{-1} \circ \cdots \circ g_N^{-1}$, $n \in [1, N]$, as g^{-n} and using the shadowing property for sequences of diffeomorphisms, it is easily shown using methods very similar to those developed by Klapper (1991) to obtain (5.4), that the Wiener bundle average of the initial field $\theta(x, t_0)$ over a $O((\Delta t/Pe)^{1/2})$ neighborhood of $g^{-N}(W^s(x^N))$ is asymptotically replaced by a properly weighted average of the zero-diffusivity solution over $E^s(x^N)$ in the Wiener bundle solution of (3.8) at x^N at $t = N\Delta t + t_0$. The asymptotic ($Pe \to \infty$) weighting law for averaging the zero-diffusivity solution over $E^s(x^N)$ is Gaussian, with zero mean and variance

$$\sigma_N^2 = \frac{2\Delta t}{Pe} \sum_{n=1}^{N} \left(\frac{1}{\lambda_n}\right)^2, \tag{5.6}$$

where $\lambda_n > 1$ is now the expansion factor of g^{-n} along the local stable direction at x^N. Again, 10^4 points are distributed uniformly along the stable direction at p_1 up to a length 3σ on either side of p_1, where σ is now computed using (5.6) at the same parameter values as in figure 5.2(a) and $\Delta t = 0.2$. These are integrated backwards up to a length of time $5T$ using the velocity field of (2.9) to obtain the preimage of the stable manifold through p_1, and is shown in figure 5.2(b). While

the satisfactory match between figures 5.2(a) and (b) shows shadowing theory can be used even when the advective component in the kinematics of a diffusive tracer is given by a sequence of diffeomorphisms, comparing figure 5.2(a,b) with figure 5.1(a,b) it is clearly evident that there is little difference between the discrete-time formulations of (5.1) and (5.2) at the large Peclet numbers being considered here.

The hyperbolic invariant sets associated with Smale horseshoes have measure zero and since there will be only a countable infinity of them, their union also has measure zero. Here it is assumed that the numerically observed chaotic particle motion in the bubble-region is owing to Smale-horseshoe-type dynamics in the vicinity of heteroclinic points; while this is definitely the case in chaotic dynamical systems with heteroclinic cycles formed by the transversal intersections of stable and unstable manifolds of normally hyperbolic invariant sets, no such precise statements can be made for the dynamical system being considered here due to reasons discussed previously. Thus, with the exception of a set of measure zero, all points are eventually advected to infinity due to the unbounded nature of the flow; this argument of course applies only to the parameter-regime where the KAM islands are of negligible size. In other words, for $N \to \infty$, the exact trajectory through a point x^N in backward time, $\{x^n\}_{n=N}^{0}$, will have $x_0 \to -\infty$ and the set of such x^N has full measure. Therefore backward iterates of points in the bubble-region, under the deterministic map f^{-1}, eventually escape to regular regions of the flow and where the dynamics does not have a hyperbolic structure. However, one can still define the stable manifold through the iterates lying in the regular regions of the flow as the preimage of the stable manifold through x_N, i.e. $f^{-n}(W^s(x^N))$. The $f^{-n}(W^s(x^N))$ can wind back to the bubble-region, as is demonstrated by extending the computations of figure 5.1(b) to a length of time $10T$, shown in figure 5.3(b); the point $p_1 = (0.25, 0.455)$ is advected backwards to $(-114.1, 0.001)$ in $10T$, as

opposed to $(-0.231, 0.503)$ in $5T$. Extending the computation of figure 5.1(a) to a length of time $10T$ and examining the distribution of Wiener initial points in only the bubble-region (see figure 5.3(a)) shows that most of the mass of this distribution is still confined to a small neighborhood of the preimage of the stable manifold through p_1, indicating the possibility of good deterministic shadowing. Wiener trajectories that escape the bubble-region will not be shadowed but, since the initial distribution is zero outside this region, their corresponding Wiener initial points make no contribution to the Wiener bundle average and can be ignored. These results indicate that shadowing results will apply for fairly long times. The point p_1 is, however, not necessarily a representative point. In fact, the local expansion rates, i.e. the β_i's, at the preimages of p_1 lying in the bubble-region are all much greater than unity and the backward trajectory through p_1 passes through strongly hyperbolic regions until it escapes the bubble-region. This is certainly not the case for every point in the bubble region.

While the asymptotic result of (5.4) was derived for systems in which the shadowing property holds rigorously and where the dynamics has a hyperbolic structure everywhere, it does give some indications as to what to expect in the typically non-uniformly hyperbolic chaotic processes. In most chaotic processes a Wiener trajectory will pass through regions where the strong transversality condition of transversal intersections of stable and unstable manifolds is not satisfied, i.e., there are homoclinic tangencies. Using again the terminology of our discrete-time formulation, this will lead to accumulation of displacements away from the preimages of the stable manifold through x^N, resulting in a wider "spread" of Wiener initial points about $f^{-N}(W^s(x^N))$. This is illustrated by choosing a point $p_2 = (-0.546, 0.32)$ close to the unstable manifold of p^- for the Poincaré map P_β, W^u_β; the preimages of p_2 (under the map $f \equiv P_\beta$), as well as the preimages of the stable manifold through

p_2, remain close to the wall for a long time. Since the likelihood that a Wiener trajectory will encounter a homoclinic tangency is increased significantly near the wall, the spread of Wiener initial points about the preimages of the stable manifold through p_2 increases, as is demonstrated by repeating the previous procedure in figure 5.4. That homoclinic tangencies are more likely in the near-wall region is explained heuristically by considering the entanglement of W^s_β and W^u_β near the wall, shown in figure 4.4. At a heteroclinic point $p \in W^s_\beta \cap W^u_\beta$, the stable direction is given by $T_p(W^s_\beta)$, and the unstable direction by $T_p(W^u_\beta)$, where $T_p(W^{s,u}_\beta)$ is the linear subspace tangent to $W^{s,u}_\beta$ at p. From figure 4.4 it is evident that as segments of $W^{s,u}_\beta$ accumulate at the wall they become increasingly parallel, except in a small neighborhood of p^- and p^+, and the angle between their intersections becomes increasingly closer to zero. Moreover, work of Hammel *et al.* (1988) and Grebogi *et al.* (1990) has shown that how long a noisy trajectory can be shadowed in a non-uniformly hyperbolic system depends on the severity of homoclinic tangencies encountered in its path. The poor match between figures 5.4(a) and (b) is therefore not surprising. Another way by which the shadowing property may be weakened is if the rate of convergence of points on the stable and unstable manifolds through a point x, in forward and backward time respectively, is not asymptotically exponential. The asymptotically algebraic and therefore slow convergence would mean that the component in the unstable direction of the noisy deviates in every time-step T is not exponentially contracted in backward time, and this would again lead to accumulation of displacements away from the preimages of the stable manifold through x. This is certainly the case for the heteroclinic points $p \in W^s_\beta \cap W^u_\beta$, due to the non-hyperbolicity of p^- and p^+. Since heteroclinic points become dense near the wall and their neighbouring points are expected to behave similarly due to continuously varying local stable and unstable directions, all points in a sufficiently thin

near-wall region will exhibit such behaviour. From these arguments it is clear that the shadowing property worsens as one approaches the near-wall region. Indeed, backward iterates of points on or in the immediate vicinity of the unstable manifold of p^-, W^u_β, will pass through the near-wall region and good (small δ) deterministic shadowing is not possible for these points. The fact is unfortunate since the zero-diffusivity solution (figures 4.2, 4.3) is localized entirely around W^u_β. However, we feel that the asymptotic expression of (5.4) continues to give the correct qualitative picture even when quantitative results are unsatisfactory.

5.3. Smoothing of the zero-diffusivity solution by diffusion at small scalar diffusivity

Due to the hyperbolic character of the dynamics in chaotic flows, the fine-scale direction (or the scalar gradient) at a point in the zero-diffusivity solution will be in the local stable direction. For a point p on the unstable manifold of p^-, $p \in W^u_\beta(\bar{\phi})$, the local unstable direction is $T_p(W^u_\beta(\bar{\phi}))$, while the local stable direction is in general complementary to $T_p(W^u_\beta(\bar{\phi}))$, unless p is a point of homoclinic tangency. It is therefore not surprising that scalar profiles extracted along $T_p(W^u_\beta)$ and in the direction orthogonal to $T_p(W^u_\beta)$ are strikingly different (see figure 4.5). These indicate that the scalar gradient at the point $p \in W^u_\beta$ is in a direction complementary to $T_p(W^u_\beta)$. Therefore, as long as the shadowing property holds, adding small scalar diffusion will smooth fine-scale structure in the zero-diffusivity solution around $p \in W^u_\beta(\bar{\phi})$, where the fine-scale direction is in general complementary to $T_p(W^u_\beta(\bar{\phi}))$. Since the zero-diffusivity distribution is almost entirely confined along $W^u_\beta(\bar{\phi})$, adding small scalar diffusion only smears out the zero-diffusivity solution about $W^u_\beta(\bar{\phi})$.

From the viewpoint being considered here, the scalar value at a point in the

bubble-region, in the presence of small scalar diffusion, depends on twin factors : firstly, the zero-diffusivity distribution in the local stable direction at that point built-up by the underlying chaotic advection and secondly, the local shape of the asymptotic weighting function imposed by the smoothing process of scalar diffusion. We consider now how these two factors vary at a point as time progresses, and also the effect of variations on the average in the local expansion rates, i.e., the β_i's. The former consideration will answer questions related to asymptotic values of the time-dependent scalar field, while the latter will address the numerically observed increase in the non-uniformity of the scalar field with increasing perturbation amplitude β. Attention is at first restricted to the sequence of scalar values $\theta_N(x,\bar{\phi}) \equiv \theta(x, t = NT + \bar{\phi}/\omega)$ at a point x for given phase or cross-section $\bar{\phi} \in [0, 2\pi)$. Since shadowing theory does not apply over infinite time-scales, we consider only *finite* N. The scalar value at a point x is said to have reached an asymptotic state if $\theta_N(x,\bar{\phi})$ does not change appreciably for $N > N_0$, where both N and N_0 are finite integers. That such an asymptotic state exists is evident from the sequence of scalar values $\{\theta_N(x \in W^u_{\beta=0.6}, \bar{\phi} = 0)\}_{N=0}^{30}$ obtained in figure 5.5, using the Wiener bundle method of (3.9); it should be evident from (3.9) that $\{\theta_N\}$ is a non-decreasing sequence. To keep the notation simple, we proceed below with $\bar{\phi} = 0$; it is then easily shown that the theory applies for any $\bar{\phi} \in [0, 2\pi)$, and therefore holds for all finite times.

It is clear that if the role of small scalar diffusion is a local smoothing of scalar gradient built-up in the zero-diffusivity solution, then the scalar value at a point in the presence of small scalar diffusion will be zero if the zero-diffusivity solution is also zero at that point and in a neighborhood of that point; the size of this neighborhood will of course depend on the variance of the smoothing function, and from (5.4) it is evident that for finite-times and large Pe, the size will be asymptotically small. From both theoretical arguments and numerical evidence presented in Chapter 4, it

is clear that the zero-diffusivity solution is confined entirely to the vicinity of $W^u_\beta(\bar{\phi})$, and therefore it will be sufficient to consider the dynamics of points in the vicinity of $W^u_\beta(\bar{\phi})$ even for the full advection-diffusion problem. Let $\bar{R}_w = (-1.5, 1) \times (0, \epsilon_1)$, where $\epsilon_1 = O(Pe^{-(\alpha+1)/2})$. Therefore $\bar{R}_w$ is the thin near-wall region in which the "initial" distribution $\theta(x, t_0)$ is non-zero. In what follows, we assume $t_0 = T$, which allows us to work with the cross-section $\bar{\phi} = 0$; the diffeomorphism f is now simply P_β. Let θ_{fr} denote the zero-diffusivity or frozen-field solution. Consider a point x in the vicinity of W^u_β, and let $\{x^n\}^0_{n=N}$ be the exact dynamical trajectory through x under backward iterations of f, i.e., $x^N \equiv x$. Then, $\theta_{fr}(x, t = NT + t_0) \neq 0$ if and only if $f^{-N}(x^N) \equiv x^0 \in \bar{R}_w$. Let $x \in W^s(y)$, where $y \in W^u_\beta$, and let $\{y^n\}^0_{n=N}$ be the exact dynamical trajectory through y under backward iterates of f, $y^N \equiv y$. Moreover, let $\forall\ N > N_1(\epsilon_1, y)$, $|f^{-N}(y^N) - p^-| < \epsilon_1$, where recall that p^- is the point of separation on the no-slip boundary. Then, if $x^0 \in \bar{R}_w$,

$$|x^0 - y^0| \simeq \lambda_N |x - y|, \tag{5.7}$$

where the segment of $W^s(y^0)$ in $\bar{R}_w$ is being approximated as a straight line and $|x - y|$ is assumed small; λ_N is the expansion factor of f^{-N} along the local stable direction of $y \in W^u_\beta$. Therefore $\theta_{fr}(y, t = NT + t_0) \neq 0$ for all $N > N_1(\epsilon_1, y)$ and from (5.7), the width of the zero-diffusivity solution at y will be $O(1/\lambda_N)$, where by "width" we mean the length over which the zero-diffusivity solution is non-zero in the local stable direction at y.

Since the exact dynamical trajectory through a point on the unstable manifold $y \in W^u_\beta$ under backward iterations of f approaches the separation point p^- and, since p^- is a non-hyperbolic stagnation point, the local expansion rates or β_n's along the backward trajectory approach unity. This fact is mathematically expressed in the following statement: $\forall\ y \in W^u_\beta$, $y \equiv y^N$ and $\forall\ \epsilon_0 > 0$, $\exists\ N_0(\epsilon_0, y) \in \mathbf{N}$ such that $\forall N > N_0$, $(\beta_N - 1) \leq \epsilon_0$. Indeed, this can be made precise by considering

the local representation of the Poincaré map near p^-. It is easily shown (see *C*.17, Appendix C) that for points (x_1, x_2) in an $O(\epsilon)$ neighborhood of p^-, $df^{-1}(x_1, x_2) \equiv dP_\beta^{-1}(x_1, x_2) = \mathbf{I} + \mathbf{r}$, where $\mathbf{I}$ is the Identity map and $\mathbf{r} = (r_1, r_2)$ is a homogeneous polynomial of degree $n \geq 1$ containing terms of $O(\epsilon)$. Since for the backward iterates of y close to p^- the local stable direction is well approximated by the coordinate x_1, it is a straightforward conclusion that, provided $f^{-N}(y)$ is in an $O(\epsilon)$ neighborhood of p^-, $(\beta_N - 1)$ is $O(\epsilon)$. Given $\epsilon_0 > 0$ small enough, choose N_0 such that $|f^{-N_0}(y) - p^-| = O(\epsilon_0^2)$, and the statement is proven. A verification is provided by numerical computations presented below (see figure 5.6).

Now, choosing ϵ_0 very small, $N_0(\epsilon_0, y) > N_1(\epsilon_1, y)$. Henceforth, we will suppress the dependence of N_0 on ϵ_0 and y. Since for all $N > N_0$

$$\lambda_N = (\beta_N \circ \cdots \circ \beta_{N_0+1}) \circ \lambda_{N_0},$$

it easily follows that

$$\lambda_N \leq (1 + \epsilon_0)^{(N-N_0)} \lambda_{N_0}. \tag{5.8}$$

Hence for all finite $N > N_0$

$$\lambda_{N_0} \leq \lambda_N \leq \lambda_{N_0} + O(\epsilon_0).$$

There is therefore an intermediate time-scale specified by $(N - N_0) < O(1/\epsilon_0)$ over which λ_N is infinitesimally close to λ_{N_0} and the width of the zero-diffusivity solution at y is $O(1/\lambda_{N_0})$. We note that though the right-hand side of (5.8) diverges for $N \to \infty$, this limit is irrelevant to our discussion since shadowing theory applies only on finite time-scales. The zero-diffusivity solution is therefore $O(1/\lambda_{N_1})$ wide at $y \in W_\beta^u$ when it first appears at $N = N_1$, but shrinks to an asymptotic width of $O(1/\lambda_{N_0})$ as N increases beyond N_0; of course since $N_0 > N_1$, $\lambda_{N_0} > \lambda_{N_1}$.

Owing to the non-hyperbolicity of p^-, backward iterates of y approach p^- very slowly. Since backward iterates of $x \in W^s(y)$, $O(1/\lambda_{N_0})$ close to y, lie on segments of

$f^{-N}(W^s(y))$ that are approximately parallel to the wall, their x_2-coordinate varies very slowly with N for N large. Again, this can be made precise by considering the local representation of $f^{-1} \equiv P_\beta^{-1}$ in the vicinity of any point on the no-slip boundary. For points (x_1, x_2) that are $O(\epsilon)$ close to the wall, it is easily shown (see Appendix C) that $|f_2^{-1}(x_1, x_2) - x_2| = O(\epsilon^2)$. Indeed, this is a consequence of the fact that every point on the no-slip boundary is non-hyperbolic. Now, from (4.1), the "initial" distribution in the near-wall boundary-layer varies only with the coordinate x_2 normal to the wall, except of course in a negligibly small neighborhood of p^-. As N increases beyond N_0, the x_2-coordinate of the backward iterates of $x \in W^s(y)$, $f_2^{-N}(x)$ (with x $O(1/\lambda_{N_0})$ close to y), remains $O(\epsilon_0^4)$ close to $f_2^{-N_0}(x)$ for all finite N, and therefore the backward iterates pick-up approximately the same scalar value from the "initial" distribution in $\bar{R}_w$. It is therefore concluded that on an intermediate time-scale specified by $N_0 < N < N_0 + O(1/\epsilon_0)$ the zero-diffusivity solution at y, and in an $O(1/\lambda_{N_0})$ vicinity of y along the local stable direction at y, does not change appreciably and can be said to have attained an asymptotic frozen-field-distribution. In addition, $\forall\ N > N_0$, and $\forall\ x \in W^s(y)$ such that x is $O(1/\lambda_{N_0})$ close to y, the variance of the Gaussian weighting function of (5.4) satisfies

$$\sigma_N^2 \leq \frac{2T}{Pe}\Big[\sum_{n=1}^{N_0} \frac{1}{\lambda_n^2} + \big(\frac{N - N_0}{\lambda_{N_0}^2}\big)\Big],$$

where use has been made of the fact that λ_n is a non-decreasing function of n. For most points in the bubble region away from the wall λ_{N_0} is large. Therefore again, for all finite $N > N_0$,

$$\sigma_{N_0}^2 \leq \sigma_N^2 \leq \sigma_{N_0}^2 + O(\frac{1}{\lambda_{N_0}^2}),$$

i.e., σ_N^2 is infinitesimally close to $\sigma_{N_0}^2$ over the intermediate time-scale specified by $(N - N_0) < O(1/\lambda_{N_0}^2)$ and can be said to have attained an asymptotic value. It follows then that the scalar distribution in the vicinity of $y \in W_\beta^u$, in the presence

of small scalar diffusion, will not change by any appreciable amount over an intermediate time-scale and can be said to have attained an asymptotic distribution. In fact, at larger perturbation amplitude β, the λ_n's are larger (see figure 5.6) and the asymptotic values, λ_{N_0} and $\sigma^2_{N_0}$, are attained in shorter time, i.e. N_0 decreases with β. This can explain the numerically observed feature that the asymptotic scalar distribution is attained over a shorter time-scale at larger perturbation amplitudes (compare figure 3.4 with figure 3.6). Since the arguments hold for any cross-section $\bar{\phi}$ and any $y \in W^u_\beta(\bar{\phi})$, the scalar field in the entire bubble-region will attain an asymptotic distribution. Moreover, at any particular point the asymptotic scalar value will be time-periodic and will have the same period as the period T of the advection field. Numerically obtained time-series in figure 3.13(b) supports this prediction.

We consider next the effect of an increase in local expansion rates. Fix $y \in W^u_\beta$, let $y \equiv y^N$, $N > N_1$, and suppose $N_1(\epsilon_1, y)$ is unchanged while the β_n's are increased. Increasing β_n's results in larger λ_N, which means a "thinner" zero-diffusivity distribution at y. Further, from (5.4), larger λ_n's yield smaller σ^2_N, and hence the scalar distribution at y, in the presence of scalar diffusion, is confined even closer to W^u_β. *Therefore, as the dynamics becomes more strongly hyperbolic, the zero-diffusivity solution is wrapped more tightly around W^u_β and diffusion is less effective as a smoothing process. Together, they account for the localized and non-uniform distributions obtained at larger perturbation amplitudes.* Of course we have no method for increasing β_n's without changing β, and consequently changing the geometrical structure of W^u_β. We cannot then consider a fixed y and examine the effect of increasing the β_n's. The only alternative is to compare y's, lying on W^u_β corresponding to different β's, that have approximately the same $N_1(\epsilon_1, y)$ for given ϵ_1. To examine this situation, we choose three representative y's: $y_1 \in W^u_{\beta=0.2}$,

$y_2 \in W^u_{\beta=0.6}$, $y_3 \in W^u_{\beta=0.8}$, all with the same $N_1(\epsilon_1, y)$ for ϵ_1 small. We choose $y_i \equiv y_i^N$, with $N = 10$, $i = 1,\ 2,\ 3$, i.e., we are considering $t = 10T + t_0$. In figure 5.6 we plot β_n, $n \in [1, 10]$, for all three cases; for given y_i, β_n is the expansion factor of f^{-1} in the local stable direction of $f^{-n+1}(y_i)$. Evidently, at larger β's, the β_n's and consequently the λ_n's are larger on account of the increased hyperbolicity of the dynamics under the Poincaré map $f \equiv P_\beta$. Not surprisingly the β_n's approach unity as n increases and preimages of y_i approach the non-hyperbolic separation point p^-.

Another method for increasing on the average the local expansion rates in the chaotic bubble-region is by modulating appropriately the coefficient A_{122} in the time-independent component $f^u(x)$ of the velocity field, given by (3.13). That this is indeed the case is shown by computing the local expansion rates or β_n's along the backward dynamical trajectory (under f^{-1}) through two representative points y_A, y_B lying on the unstable manifolds W_A, W_B respectively, where $W_A \equiv W^u_\beta$ for $\beta = 0.5$, $\omega = 0.5$ and $A_{122} = 4.5Kx_s$ while $W_B \equiv W^u_\beta$ for $\beta = 0.5$, $\omega = 0.5$ and $A_{122} = 2Kx_s$, and again $N_1(\epsilon_1, y_A) \simeq N_1(\epsilon_1, y_B)$. Note that the perturbation parameters β, ω are chosen to be identical to that in figures 3.16 and 3.17. The numerical results, displayed in figure 5.7, show that the local expansion rates for $A_{122} = 2Kx_s$ are significantly higher than that for $A_{122} = 4.5Kx_s$. Lowering A_{122} not only increases the size of the unperturbed bubble and consequently the size of the chaotic bubble-region in the associated time-periodically perturbed flow, but also increases on the average the local expansion rates. Then, following our discussion above, it is expected that the scalar distribution would become more non-uniform and localized about $W^u_\beta(\bar{\phi})$ at lower A_{122}. This explains the observations made in §3.6 regarding the sharp qualitative difference between the scalar distributions of figures 3.16(a,b) and 3.17(a,b) corresponding to two different values of the coefficient A_{122}.

We consider finally how the distribution varies, at a fixed time $t = NT + t_0$, as one moves further away from p^- in terms of arclength along W^u_β; again it is assumed $t_0 = T$, so that we can work with the cross-section $\bar{\phi} = 0$. As $y \in W^u_\beta$ moves away from p^- in terms of arclength along W^u_β, $N_1(\epsilon_1, y)$ increases and the zero-diffusivity solution attains a non-zero value at y at a later time. Consider two points $y_1,\ y_2 \in W^u_\beta$, where $y_1 <_l y_2$, i.e., y_1 is closer to p^- in terms of arclength along W^u_β. Fix $N > N_1(\epsilon_1, y_2) > N_1(\epsilon_1, y_1)$. Now, our numerical simulations show that the local expansion rates or β_n's in general decrease monotonically along each backward trajectory $\{y^n\}^0_{n=N}$ on W^u_β; this fact is evident from figure 5.6. On a cautionary note we add that this may be violated if the backward trajectory through $y \in W^u_\beta$ passes through regions with homoclinic tangencies, since these regions are also characterized by weak stretching; figure 5.7 shows one such case where the monotonic decrease in β_n's is violated in one iterate. Since $f^{-n}(y_1) <_l f^{-n}(y_2)$ for all $n \in [0, N]$ and, as long as β_n decreases monotonically as p^- is approached along W^u_β, $\lambda_n(y_1) < \lambda_n(y_2)$, where $\lambda_n(y_i)$ is the expansion factor of f^{-n} along the stable direction of y_i. Therefore $\lambda_N(y_1) < \lambda_N(y_2)$, and the zero-diffusivity distribution at y_2 is thinner than at y_1. Further, because of the larger $\lambda_n(y_2)$'s, $\sigma^2_N(y_2) < \sigma^2_N(y_1)$. Therefore a thinner zero-diffusivity distribution at y_2 is smoothed against a Gaussian with smaller variance, which means the scalar distribution about W^u_β, in the presence of scalar diffusion, should in general narrow down as one moves further away from p^- in terms of arclength along W^u_β; note that there is a (weak) gradient in the zero-diffusivity solution along W^u_β (see figure 4.5(a)), and $\theta_{fr}(y_2, t = NT + t_0) < \theta_{fr}(y_1, t = NT + t_0)$. From figures 3.3(a-d) and 3.6(a-d) it is evident that the numerical simulation results agree with the predictions made above, with the exception of regions where the manifold W^u_β has large curvature. Since these are also the regions where homoclinic tangencies are

likely (Farmer & Sidorowich 1991), the discrepancy is not entirely surprising. Note that since W^u_β is not a submanifold of $\mathbb{R}^2$, segments of W^u_β wind back infinitesimally close to each other such that the distributions along them may overlap, which can make verification of the previous prediction difficult (e.g., see figure 3.4). Also, for points $y \in W^u_\beta$ that are far away from p^- in terms of arclength along W^u_β, the backward trajectory through y is bound to pass through weakly stretched regions as W^u_β has a folded structure with several segments of large curvature signalling the likelihood of homoclinic tangencies, and for these points the theory becomes uncertain owing to likely violations in the assumption of monotonic decrease in β_n along the backward trajectory $\{y^n\}^0_{n=N}$. The predictions are therefore more likely to hold for the situation in figures 3.3(a-d) and 3.6(a-d) where the scalar distribution remains localized along W^u_β up to only a relatively short distance in terms of arclength along p^- as opposed to that in figure 3.4. The arguments given above remain unchanged if $N_1(\epsilon_1, y)$ is replaced by $N_0(\epsilon_0, y)$, and therefore the conclusions are identical for the asymptotic scalar distribution. Moreover, since $N_0(\epsilon_0, y)$ increases as $y \in W^u_\beta$ moves away from p^- in terms of arclength along W^u_β, the asymptotic distribution is attained over a longer time at points further away from p^- in terms of arclength along W^u_β. Finally, as N_0 increases, the asymptotic value of the standard deviation of the Gaussian weighting function will become much greater than the asymptotic width of the zero-diffusivity solution about W^u_β, i.e., $\sigma_{N_0} >> O(1/\lambda_{N_0})$, in which case a Gaussian smoothing of the zero-diffusivity solution will be nearly zero, and therefore the asymptotic scalar distribution, in the presence of small scalar diffusion, will tend to zero as one moves far away from p^- in terms of arclength along W^u_β. Comparing figure 2.3(a) with figure 3.3(d) shows that such is indeed the case. As usual the theory applies to any cross-section $\bar{\phi}$, leading to identical conclusions for the scalar distribution along $W^u_\beta(\bar{\phi})$.

We refrain from making any quantitative comparisons between scalar values obtained from our random-walk schemes and that predicted using the asymptotic shadowing result of (5.4). The main difficulty is the arbitrariness involved in choosing t_0, which is the cut-off time for the boundary-layer solution of Chapter 4 and determines the "initial" distribution for the fictitous zero-diffusivity solution. While the zero-diffusivity solution thus constructed offers a convenient heuristic tool for examining the role of small scalar diffusion, it seems difficult to extract any quantitative information from it. Moreover, the previously mentioned lack of good (small δ) deterministic shadowing indicates that any quantitative results based on (5.4) will be unsatisfactory.

For the case with surviving KAM tori enclosing the core-region of the bubble, the presence of invariant closed curves as well as the islands of stability enclosed within precludes the possibility of applying shadowing theory. In fact, the theory becomes uncertain whenever there are invariant curves since Wiener trajectories crossing invariant curves will not be shadowed (Klapper 1992a) and diffusion can produce effects that will not be captured by the shadowing theory. For the cases considered in this section, the flow-domain has no invariant curves and is very much the basis for arguing that shadowing theory will continue to give the correct qualitative results even when small δ shadowing is unlikely.

FIGURES

Figure 5.1(a): Distribution of 10^4 Wiener initial points that arrive at the point $p_1 = (0.25, 0.455)$ in time $t = 5T$. Relevant parameter values are $\beta = 0.6$, $\omega = 0.72$, $Pe = 10^6$, and $T = 2\pi/\omega$.

Figure 5.1(b): 10^4 points lined up along the stable direction at $p_1 = (0.25, 0.455)$ upto a length 3σ on either side of p_1 and integrated backwards for a length of time $5T$, where $\sigma = 0.0015$ and is computed using (5.4) for parameter values identical to (a).

Figure 5.2(a): Distribution of 10^4 Wiener initial points that arrive at the point $p_1 = (0.25, 0.455)$ in time $t = 5T$, where the Wiener trajectories are generated using (5.5) with time-step $\Delta t = 0.2$. Relevant parameter values are $\beta = 0.6$, $\omega = 0.72$, $Pe = 10^6$, and $T = 2\pi/\omega$.

Figure 5.2(b): 10^4 points lined up along the stable direction at $p_1 = (0.25, 0.455)$ upto a length 3σ on either side of p_1 and integrated backwards for a length of time $5T$, where $\sigma = 0.0018$ and is computed using (5.6) for parameter values identical to (a).

Figure 5.3(a): Distribution of 2×10^4 Wiener initial points that arrive at the point $p_1 = (0.25, 0.455)$ in time $t = 10T$. Relevant parameter values are $\beta = 0.6$, $\omega = 0.72$, $Pe = 10^6$, and $T = 2\pi/\omega$.

Figure 5.3(b): 2×10^4 points lined up along the stable direction at $p_1 = (0.25, 0.455)$ upto a length 3σ on either side of p_1 and integrated backwards for a length of time $10T$, where $\sigma = 0.0015$ and is computed using (5.4) for parameter values identical to (a).

Figure 5.4(a): Distribution of 10^4 Wiener initial points that arrive at the point

$p_2 = (-0.546, 0.32)$ in time $t = 10T$. Relevant parameter values are $\beta = 0.6$, $\omega = 0.72$, $Pe = 10^6$, and $T = 2\pi/\omega$.

Figure 5.4(b): 10^4 points lined up along the stable direction at $p_2 = (-0.546, 0.32)$ upto a length 3σ on either side of x and integrated backwards for a length of time $10T$, where $\sigma = 0.000714$ and is computed using (5.4) for parameter values identical to (a).

Figure 5.5: Sequence of scalar values $\theta_N = \theta(x_1, x_2, NT)$ vs. $N \in [1, 20]$, at $(x_1, x_2) = (-0.547, 0.321) \in W^u_\beta$, obtained using the Wiener bundle method for $\beta = 0.6$, $\omega = 0.72$, $Pe = 10^5$.

Figure 5.6: Local expansion rates, β_n, at points on the exact trajectory $\{y_i^n\}_{n=N}^0$, $N = 10$, $i = 1,\ 2,\ 3$, and (a) $y_1^N = (0.55, 0.1649) \in W^u_{\beta=0.2}$, (b) $y_2^N = (0.5, 0.15288)$ $\in W^u_{\beta=0.6}$, (c) $y_3^N = (0.5, 0.1476) \in W^u_{\beta=0.8}$. The perturbation frequency $\omega = 0.72$ in all three cases. The points y_1^N and y_2^N are plotted in figures 2(b) and (a) respectively.

Figure 5.7: Local expansion rates, β_n, at points on the exact trajectory $\{y_{A,B}^n\}_{n=N}^0$, $N = 10$, and (a) $y_A^N = (0.50352, 0.11174) \in W_A$, (b) $y_B^N = (-0.30030,\ 0.58182) \in$ W_B. Case (a) corresponds to $A_{122} = 4.5Kx_s$ and case (b) corresponds to $A_{122} = 2Kx_s$, where A_{122} is the coefficient in (3.10). The perturbation parameters are $\beta = 0.5$, $\omega = 0.5$ in both cases.

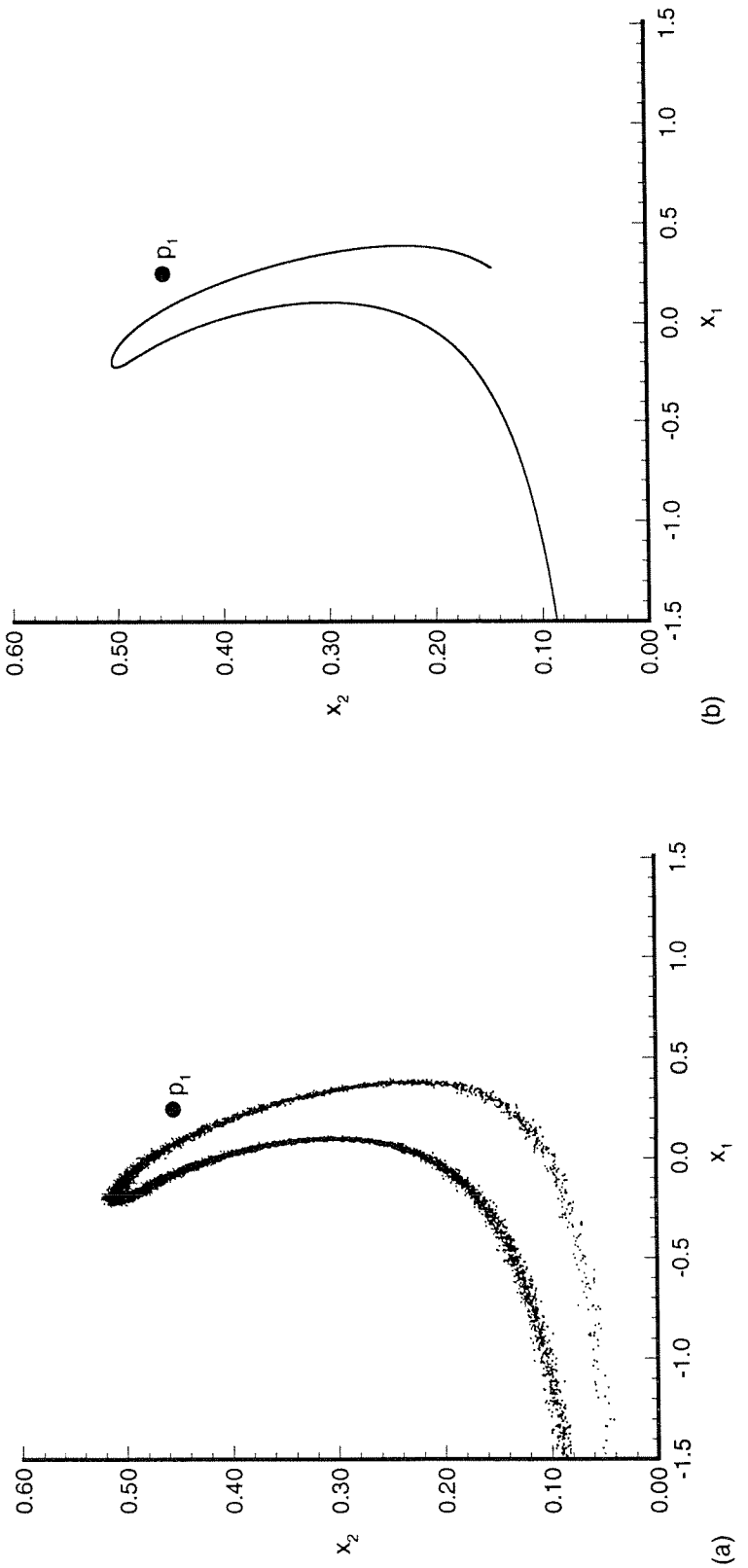
p1
0.60
0.50
0.40
0.30
0.20
0.10
0.00
-1.5
-1.0
-0.5
0.0
0.5
1.0
1.5
x2
x1
(a)
p1
0.60
0.50
0.40
0.30
0.20
0.10
0.00
-1.5
-1.0
-0.5
0.0
0.5
1.0
1.5
x2
x1
(b)

Figure 5.1(a,b)

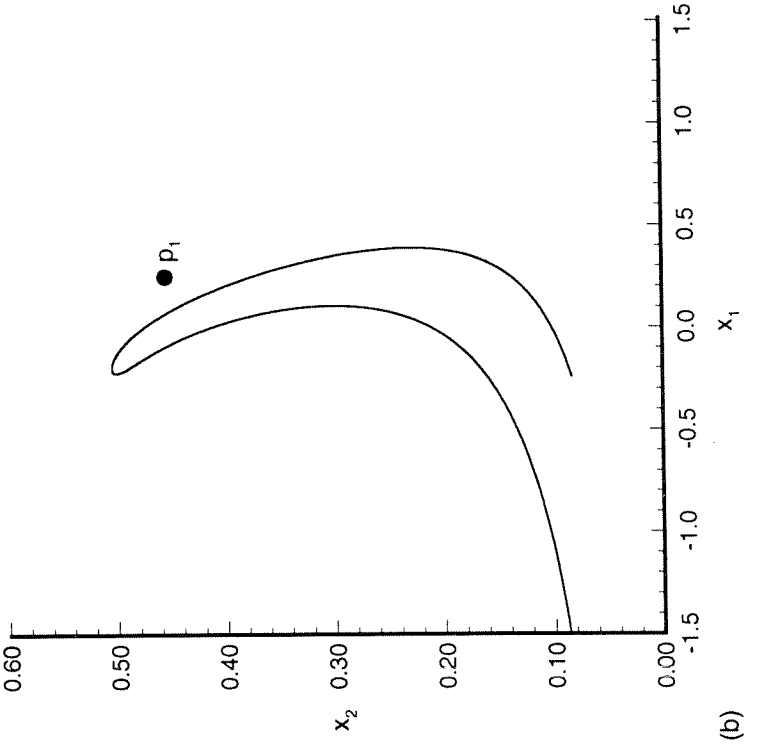
0.60
0.50
0.40
0.30
0.20
0.10
0.00
-1.5
-1.0
-0.5
0.0
0.5
1.0
1.5
x_2
x_1
p_1
(b)

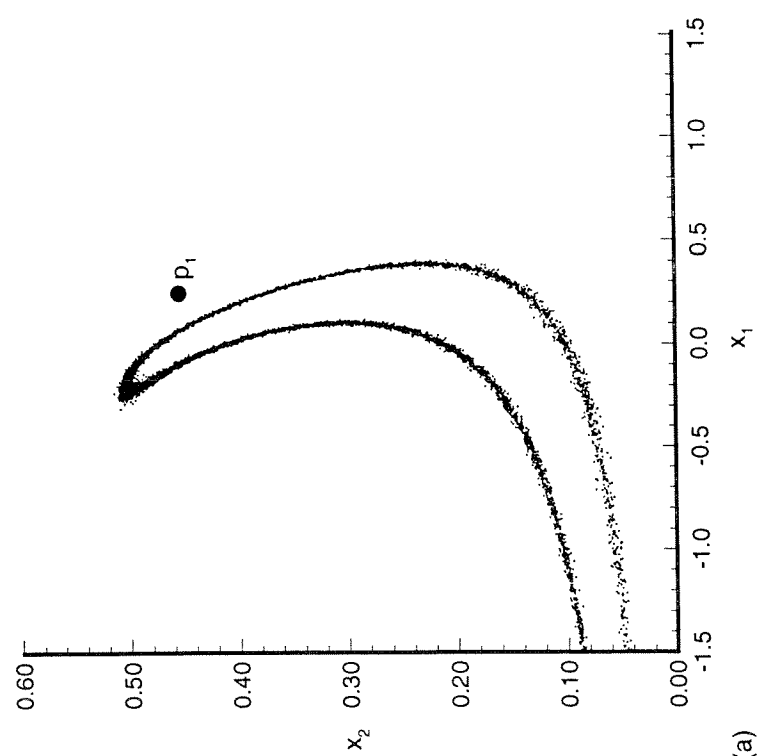
0.60
0.50
0.40
0.30
0.20
0.10
0.00
-1.5
-1.0
-0.5
0.0
0.5
1.0
1.5
x_2
x_1
p_1
(a)

Figure 5.2(a,b)

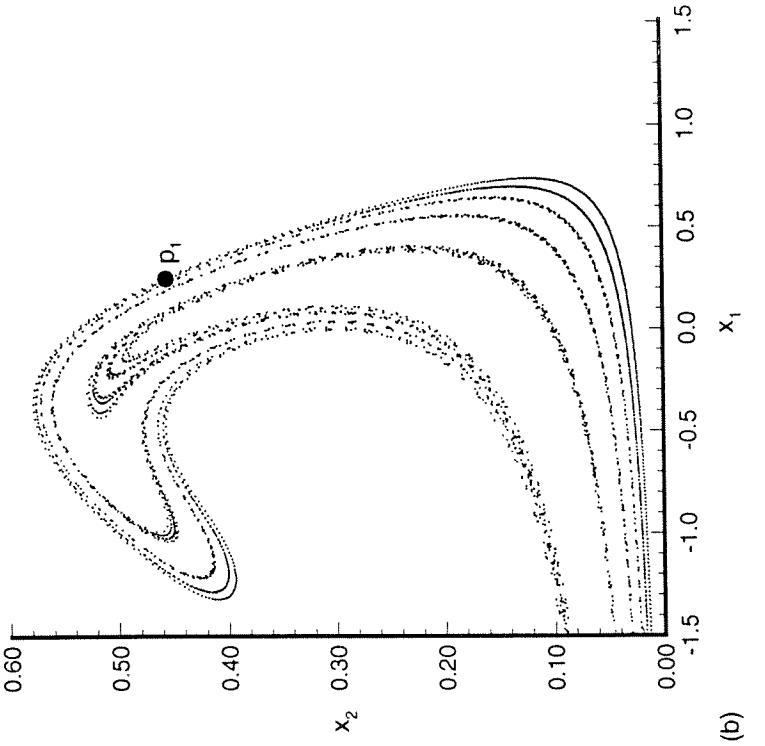
0.60
0.50
0.40
0.30
0.20
0.10
0.00
x_2
p_1
-1.5
-1.0
-0.5
0.0
0.5
1.0
1.5
x_1
(b)

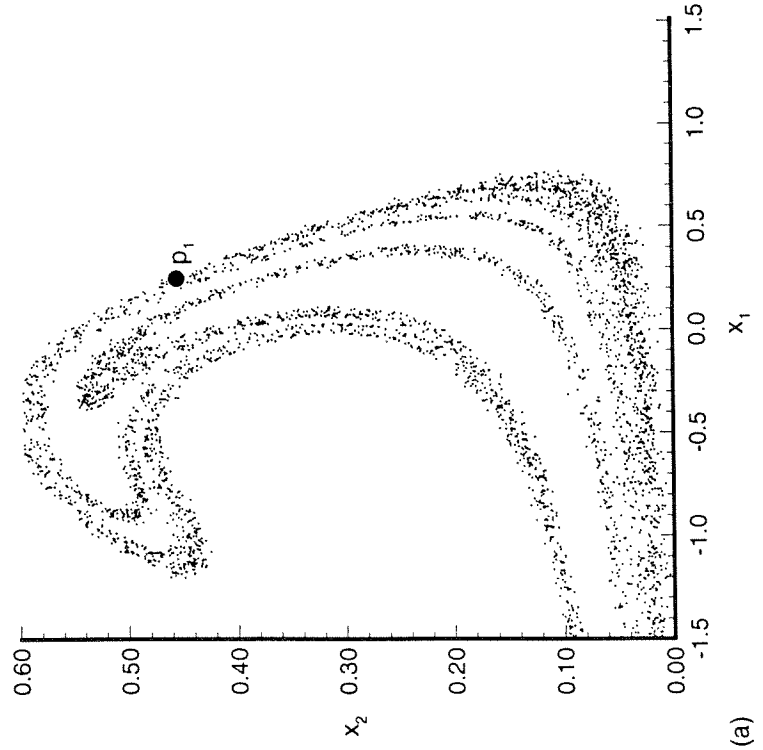
0.60
0.50
0.40
0.30
0.20
0.10
0.00
x_2
p_1
-1.5
-1.0
-0.5
0.0
0.5
1.0
1.5
x_1
(a)

Figure 5.3(a,b)

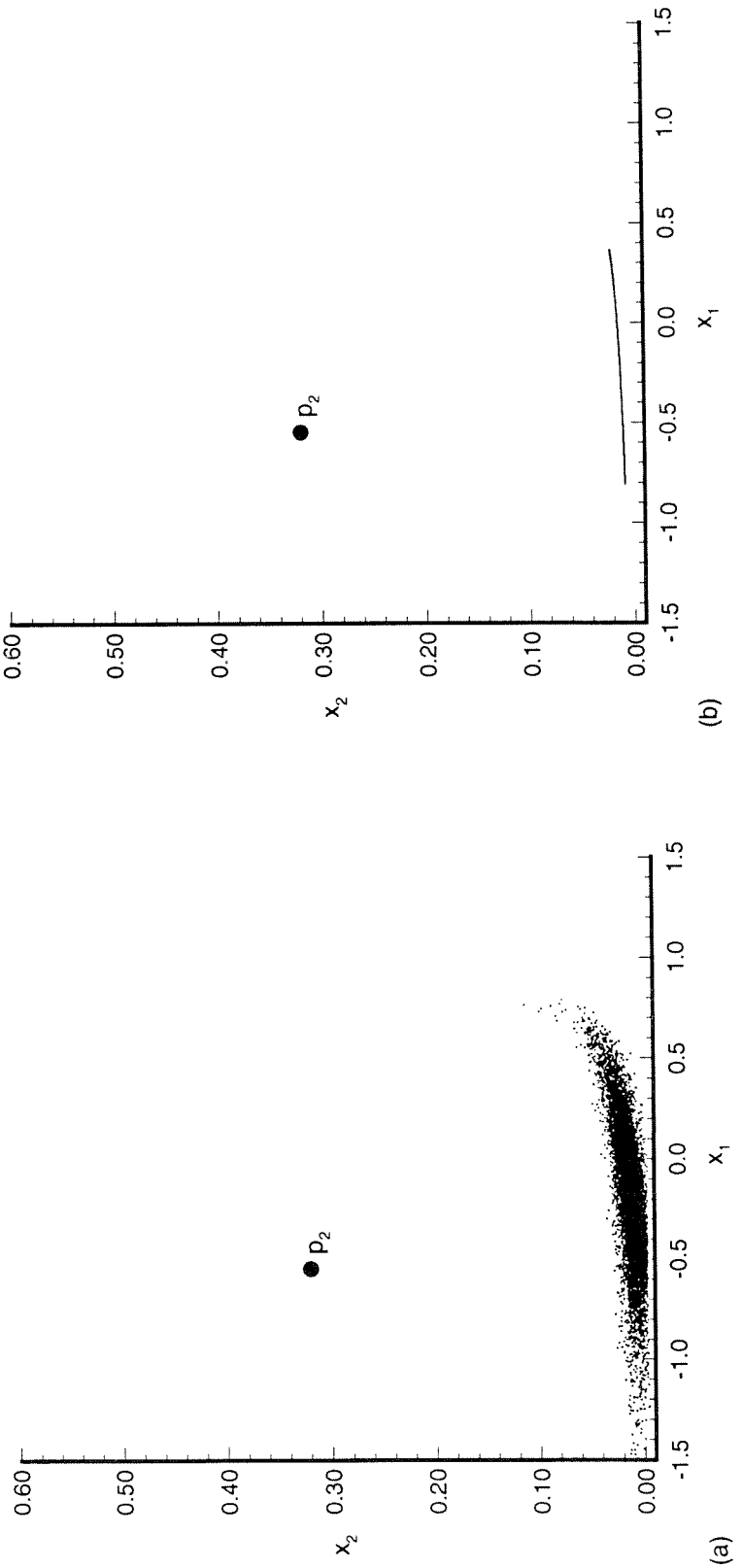

Figure 5.4(a,b)

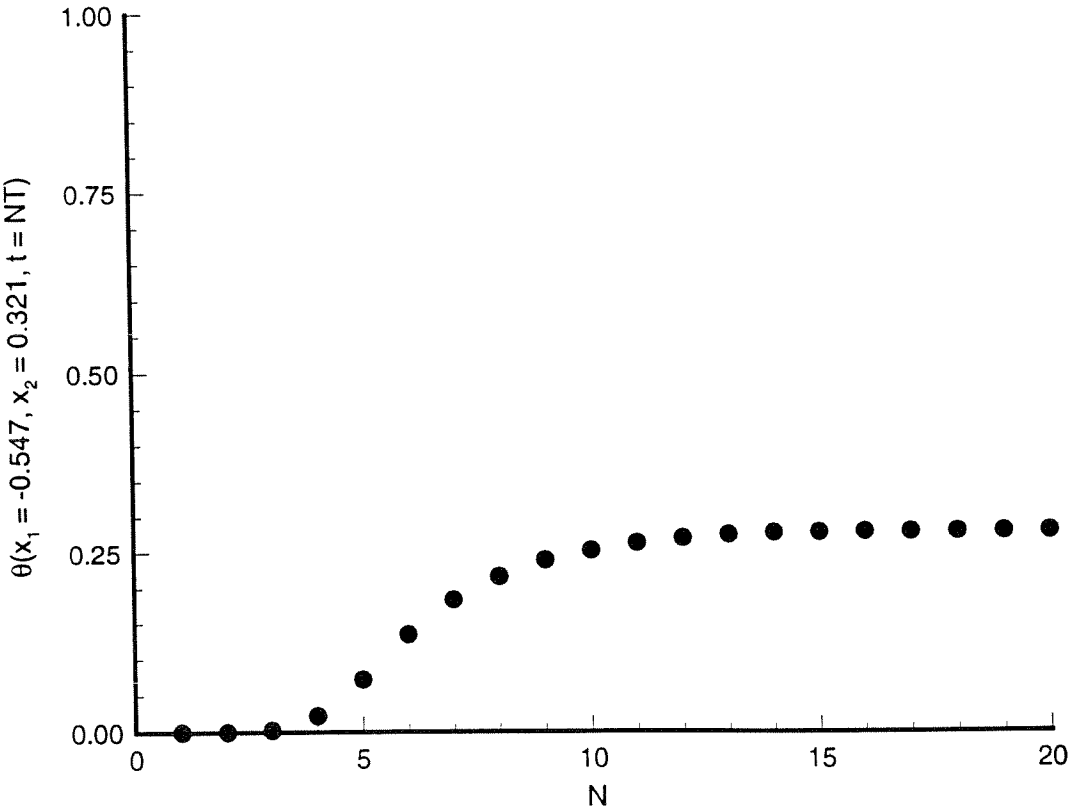

Figure 5.5

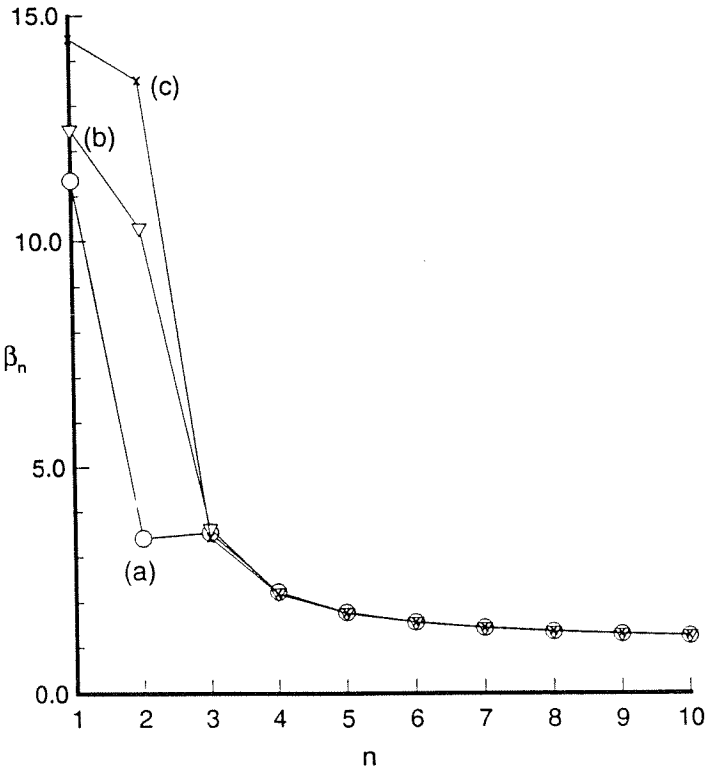

Figure 5.6

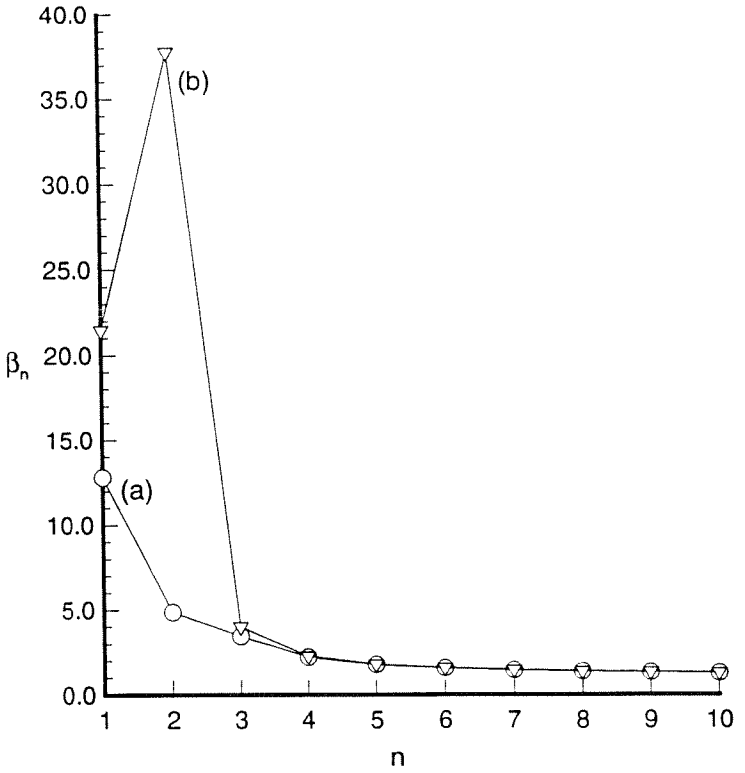

Figure 5.7

Chapter 6

Conclusions

We have examined scalar advection-diffusion in a two-dimensional flow with chaotic particle trajectories adjacent to an active no-slip surface at the limit of large Peclet number or small scalar diffusivity using results from dynamical systems theory. An unstable manifold emanating from a point of zero time-averaged shear-stress on the no-slip boundary is found to play a dominant role in the advection-diffusion of passive scalar from the boundary, particularly when the underlying chaotic particle motion is widespread and the dynamics in the flow has a pronounced hyperbolic character. It is found that the increased hyperbolicity results in scalar distributions that are localized entirely along the unstable manifold with sharp scalar gradients. Introducing a fictitious zero-diffusivity solution provides an understanding of the relationship between the stirring and mixing processes and shadowing theory gives a nice physical description of the role of small scalar diffusion as a local smoothing of fine scale variations created by the stirring process. A novel feature in this problem is the presence of the no-slip boundary and the interaction between the non-hyperbolicity at the boundary and the strongly hyperbolic character of the overlying chaotic advection in the bubble-region of the flow. The non-hyperbolicity at the

boundary is found to play an important role in the advection-diffusion process and strongly influences the time-evolution of the scalar field. The wall-integrated flux remains $O(Pe^{-2/3})$ even in the chaotic-advection-case. Introducing a time-periodic perturbation in the steady advection field introduces only weak time-dependence in the near-wall thermal boundary-layer after the initial transients have died down, resulting in weak enhancement in the asymptotic flux over the steady-advection-case. Our numerical simulation results show that in the presence of widespread chaotic particle motion the scalar distribution attains an asymptotic distribution over a time-scale that is much shorter than the time-scale over which an asymptotic distribution is attained in the steady flow. Moreover, this asymptotic distribution is found to be time-periodic with the same period as the velocity field.

Appendix A

Derivation of the Melnikov function

The Melnikov function, obtained below, is a signed measure of the distance between $W^s_\beta(\bar{\phi})$ and $W^u_\beta(\bar{\phi})$. More precisely, it is, up to a normalization factor, the coefficient in the first-order term of the Taylor-series expansion in β of the distance between $W^s_\beta(\bar{\phi})$ and $W^u_\beta(\bar{\phi})$ measured along the direction normal to the unperturbed heteroclinic orbit. We of course assume $W^s(\gamma^+(t))$ and $W^u(\gamma^-(t))$ persist for $\beta \neq 0$; supporting numerical evidence is available from figure 2.3. Moreover, the perturbed manifolds of the suspended system (2.10), $W^s(\gamma^+_\beta(t))$ and $W^u(\gamma^-_\beta(t))$, are assumed to be differentiable (C^r, $r \geq 2$) with respect to the parameter β. For normally hyperbolic invariant manifolds, both persistence and smoothness of their stable and unstable manifolds are guaranteed at small perturbations by the invariant manifold theorem of Hirsch *et al.* (1977), but because of the non-hyperbolicity of $\gamma^\pm(t)$ of (2.11), one is forced to resort to the above assumptions.

Denoting the projection of orbits lying on $W^s(\gamma^+_\beta(t))$, $W^u(\gamma^-_\beta(t))$ onto the cross-section $\Sigma^{\bar{\phi}}$ by $q^s_\beta(t,\tau)$ and $q^u_\beta(t,\tau)$ respectively, and expressing the stream function of (2.8) as the sum of a time-independent part ψ_0 and time-periodic part

ψ_1:

$$\psi = \psi_0 + \psi_1,$$

where

$$\begin{aligned} \psi_0 &= -\frac{x_2^2}{2} + x_2^3 + \frac{x_1^2 x_2^2}{2} - \frac{x_2^4}{6}, \\ \psi_1 &= x_1 x_2^3 \sin(\omega t), \end{aligned} \tag{A.1}$$

it can be shown (see Appendix B, Camassa & Wiggins 1991) that the Melnikov function is given by

$$\begin{aligned} M(\tau) = &\int_{-\infty}^{+\infty} \{\psi_0(q^0(t-\tau)),\ \psi_1(q^0(t-\tau), t)\} dt \\ &+ \lim_{\bar{t} \to -\infty} \Delta^u(\bar{t}, \tau) - \lim_{\bar{t} \to \infty} \Delta^s(\bar{t}, \tau), \end{aligned} \tag{A.2}$$

where $\{\ ,\ \}$ denotes the Poisson bracket (Guckenheimer & Holmes 1983), $q^0(t-\tau)$ is the unperturbed heteroclinic orbit on the heteroclinic connection ψ_h, $\tau \in \mathbb{R}$ parameterizes the heteroclinic orbit, and

$$\Delta^{s,u}(t, \tau) \equiv D\psi_0(q^0(t-\tau)) \cdot \frac{\partial q_\beta^{s,u}(t, \tau)}{\partial \beta} \bigg|_{\beta=0}. \tag{A.3}$$

The second and third terms in (A.2), called *boundary-terms*, always vanish in the hyperbolic case, i.e., when the heteroclinic orbit $q^0(t-\tau)$ asymptotes to hyperbolic stagnation points in forward and backward time. Note that

$$\lim_{t \to \infty} q^0(t-\tau) = p^+ \text{ and } \lim_{t \to -\infty} q^0(t-\tau) = p^-.$$

Since both p^+ and p^- are stagnation points,

$$\lim_{t \to \pm\infty} D\psi_0(q^0(t-\tau)) = 0.$$

This follows from the fact that the unperturbed vector field (i.e., 2.9 with $\beta = 0$) is given by $\dot{x} = JD\psi_0(x)$, where

$$J = \begin{pmatrix} 0 & 1 \\ -1 & 0 \end{pmatrix},$$

and since $p^{\pm}$ are stagnation points,

$$JD\psi_0(p^{\pm}) = 0,$$

which immediately implies

$$D\psi_0(p^{\pm}) = 0,$$

since J is non-singular. The second and third terms in $(A.2)$ will therefore vanish if $\lim_{t\to\infty} q_1^s(t,\tau) \equiv \frac{\partial q_\beta^s(t,\tau)}{\partial\beta}\Big|_{\beta=0}$ and $\lim_{t\to-\infty} q_1^u(t,\tau) \equiv \frac{\partial q_\beta^u(t,\tau)}{\partial\beta}\Big|_{\beta=0}$ are bounded. In the hyperbolic case, i.e., if p^+ and p^- were hyperbolic, one could obtain the following representation of solutions in $W^s(\gamma_\beta^+(t))$ and $W^u(\gamma_\beta^-(t))$, starting within $O(\beta)$ of $q^0(-\tau)$:

$$\begin{aligned} q_\beta^s(t,\tau) &= q^0(t-\tau) + \beta q_1^s(t,\tau) + O(\beta^2),\ t\in[0,\infty), \\ q_\beta^u(t,\tau) &= q^0(t-\tau) + \beta q_1^u(t,\tau) + O(\beta^2),\ t\in(-\infty,0], \end{aligned} \tag{A.4}$$

with uniform validity in the indicated semi-infinite time-intervals. This follows from work of Sanders (1982) who obtained the asymptotics of solutions in the perturbed manifolds. The result is non-trivial since the perturbation expansions of $(A.4)$ are uniformly valid on arbitrarily long or *semi-infinite* time-intervals, and establishes the boundedness of $q_1^{s,u}(t,\tau)$ on the appropriate semi-infinite time-intervals. Indeed, if the asymptotic convergence of $q^0(t)$ to $p^{\pm}$, and $q_\beta^{s,u}(t,\tau)$ to $\gamma_\beta^{\pm}(t)$ were *exponential*, results obtained by Sanders (1982) show that the exponential contraction along the (local) stable (resp. unstable) manifold of the then necessarily hyperbolic periodic orbits, $\gamma^{\pm}(t)$ and $\gamma_\beta^{\pm}(t)$, in forward (resp. backward) time would lead to the following estimates:

$$\begin{aligned} q_\beta^s(t,\tau) &= q^0(t-\tau) + O(\beta(1+e^{-\mu t})),\ t\in[0,\infty), \\ q_\beta^u(t,\tau) &= q^0(t-\tau) + O(\beta(1+e^{\mu t})),\ t\in(-\infty,0], \end{aligned}$$

where $\mu > 0$ and depends only on ψ_0. But the result becomes invalid in the non-hyperbolic case since now the asymptotic convergence of $q^0(t)$ to $p^{\pm}$, and $q_\beta^{s,u}(t,\tau)$

to $\gamma_\beta^\pm(t)$ is only algebraic. However, it is shown below that in spite of the non-hyperbolicity of $p^\pm$, $(A.4)$ remains valid for the flow under consideration and the boundary-terms in $(A.2)$ indeed drop out.

The assumption of smooth dependence of (local) stable and unstable manifolds on the parameter β is technically expressed by the statement that there exists a constant δ, independent of β, such that in a tubular δ-neighborhood U_δ of $\gamma^+(t) \equiv p^+ \times S^1$, and containing $\gamma_\beta^+(t)$, there exists within $O(\beta)$-distance from the local unperturbed stable manifold $W^s_{loc}(\gamma^+(t))$ a stable manifold $W^s_{loc}(\gamma_\beta^+(t))$ of (2.10). More precisely, $W^s_{loc}(\gamma_\beta^+(t))$ is C^r β-close to $W^s_{loc}(\gamma^+(t))$. Perturbed orbits starting within $O(\beta)$ of $q^0(-\tau)$ remain within $O(\beta)$ of $q^0(t-\tau)$ for *finite* times as a simple consequence of Gronwall's lemma, and one can therefore follow any such orbit from an arbitrary point near $q^0(-\tau)$ on ψ_h outside U_δ to the boundary of U_δ, at, say $t = t_1$ (Guckenheimer & Holmes 1983). Therefore

$$|q^s_\beta(t,\tau) - q^0(t-\tau)| = O(\beta),\ t \in [0, t_1).$$

Since $W^s_{loc}(\gamma_\beta^+(t))$ is assumed C^r β-close to $W^s_{loc}(\gamma^+(t))$,

$$|q^s_\beta(t_1,\tau) - q^0(t_1-\tau)| = O(\beta).$$

However, this does not ensure that $q^s_\beta(t,\tau)$ and $q^0(t-\tau)$ remain within $O(\beta)$ for all forward time despite the fact that, by assumption, there are points in $W^s_{loc}(\gamma^+(t))$ that are $O(\beta)$ near $q^s_\beta(t,\tau)$ for all $t > t_1$; these points may as well belong to different solutions (Sanders 1982). Now, in the hyperbolic case, i.e., say if $\gamma^\pm(t)$ were normally hyperbolic, for $O(\beta)$ perturbations in general $\gamma_\beta^\pm(t) = \gamma^\pm(t) + O(\beta)$, by the perturbation theory for normally hyperbolic invariant manifolds (Hirsch *et al.* 1977, Fenichel 1971), in which case $0 < \beta < \delta$, where δ specifies the size of the tubular δ-neighborhood U_δ; this is so in order that both the unperturbed and perturbed periodic orbits, $\gamma^\pm(t)$ and $\gamma_\beta^\pm(t)$, are contained within U_δ. But, our problem is

simplified by the fact that $\gamma_\beta^\pm(t)$ is *identical* to $\gamma^\pm(t)$, since the manifold emanation points on the no-slip boundary remain at $p^\pm$ for all time even in the time-periodically perturbed flow (see §2.2, §3.5 and Appendix C). That is to say,

$$\gamma_\beta^\pm(t) = \gamma^\pm(t).$$

Hence, one may choose δ to be $O(\beta)$, i.e., $\delta = C\beta$, C a positive constant. Since $W^s_{loc}(\gamma^+(t))$ and $W^s_{loc}(\gamma^+_\beta(t))$ are positively invariant by definition,

$$|q^s_\beta(t,\tau) - q^0(t-\tau)| = O(\beta),\ t \in (t_1, \infty).$$

Reversing time and considering $\gamma^-(t)$, one obtains a similar result for $q^u_\beta(t,\tau)$. In effect, we have shown that $q^s_1(t,\tau)$ is bounded for all $t \in [0,\infty)$, and $q^u_1(t,\tau)$ is bounded for all $t \in (-\infty, 0]$. Consequently, the boundary-terms in $(A.2)$ drop out.

It may be noted that the method outlined above will also work for the flow field considered in Camassa & Wiggins (1991) in their case of no-slip boundary conditions, making tedious calculations of $[\partial q^{s,u}_\epsilon(t,\tau)/\partial\epsilon]|_{\epsilon=0}$ (they use ϵ instead of β for perturbation amplitude) through the first variational equation unnecessary. Indeed, for our problem attempting to repeat a similar scheme leads to formidable complications on account of the more complicated form of the unperturbed heteroclinic orbit.

Finally, we obtain below a simplified form of the Melnikov function in $(A.2)$. Letting $t \to t + t_0$ in $(A.2)$ and substituting $(A.1)$ in $(A.2)$, yields

$$M(\tau) = A_1(\omega)\cos(\omega\tau) + A_2(\omega)\sin(\omega\tau), \tag{A.5}$$

where

$$A_1(\omega) = \int_{-\infty}^{+\infty} (f_1^u g_2^u - f_2^u g_1^u)(q^0(t))\sin(\omega t)dt, \tag{A.6}$$

$$A_2(\omega) = \int_{-\infty}^{+\infty} (f_1^u g_2^u - f_2^u g_1^u)(q^0(t))\cos(\omega t)dt, \tag{A.7}$$

and $(f_1^u, f_2^u) \equiv f^u$, $(g_1^u, g_2^u) \equiv g^u$ are same as in (2.9). By the symmetry of the unperturbed flow field

$$(q_1^0(t), q_2^0(t)) = (-q_1^0(-t), q_2^0(-t))$$

where q_1^0 is the x_1-component and q_2^0 is the x_2-component of q^0, and $q_1^0(0) = 0$. Moreover, it is easily seen that $(f_1^u g_2^u - f_2^u g_1^u)$ is an even function of x_1. Hence,

$$(f_1^u g_2^u - f_2^u g_1^u)(q_1^0(t), q_2^0(t)) = (f_1^u g_2^u - f_2^u g_1^u)(q_1^0(-t), q_2^0(-t)),$$

i.e., $(f_1^u g_2^u - f_2^u g_1^u)$ is an even function of t. It follows immediately that the integrand in $(A.6)$ is an odd function of t, and therefore

$$A_1(\omega) = 0.$$

Denoting $A_2(\omega)$ as $A(\omega)$ in $(A.5)$ yields (2.12), and $A(\omega)$ is given by $(A.7)$, which is identical to (2.13). In fact, $(A.7)$ can be further simplified by noting that the integrand in $(A.7)$ is an even function of t, which immediately implies

$$A(\omega) = 2\int_0^{+\infty} (f_1^u g_2^u - f_2^u g_1^u)(q^0(t)) \cos(\omega t) dt,$$

and this is the expression used in the numerical computations of $A(\omega)$.

Appendix B

Error estimation

B.1 Error estimate for the Wiener bundle method

From (3.9), the Wiener bundle solution at a point x at time t is given by

$$\theta(x,t) = \frac{n(x,t)}{N}, \tag{B.1}$$

where N is the number of "particles" released from the point x at time t, and $n(x,t) \leq N$ is the number of particles that reach the active portion of the wall and are terminated, out of the total N particles, after backward integration over a length of time t using (3.3). To each of the N particles is associated a discrete random variable $p_i(x,t)$, $i = 1,\ldots,N$, and $p_i(x,t) = 1$ if the i^{th} particle is one of the n particles that are terminated on reaching the active portion of the wall, $p_i(x,t) = 0$ otherwise. We consider (x,t) fixed and henceforth suppress these dependences. In terms of the p_i, $(B.1)$ becomes:

$$\theta = \frac{1}{N}\sum_{i=1}^{N} p_i. \tag{B.2}$$

The above is the "observed" value of the random variable θ. The mean of the observed value is presumed to be the correct value, in which case the standard deviation of the observed value is a measure of the error.

Let $E[\cdot]$ denote expectation. The variance of θ is given by

$$\begin{aligned}\sigma_\theta^2 &= E[(\theta - E[\theta])^2], \\ &= E[\theta^2] - (E[\theta])^2.\end{aligned}$$

Substituting $(B.2)$, and a little algebra, gives

$$\sigma_\theta^2 = \frac{1}{N^2}\left\{E\left[\sum_{i=1}^{N} p_i^2\right] + E\left[\sum_{i=1}^{N}\sum_{j=1,j\neq i}^{N} p_i p_j\right] - \left(E\left[\sum_{i=1}^{N} p_i\right]\right)^2\right\}. \qquad (B.3)$$

Now,

$$\begin{aligned}E\left[\sum_{i=1}^{N} p_i\right] E\left[\sum_{j=1}^{N} p_j\right] &= \sum_{i=1}^{N} E[p_i] \sum_{j=1}^{N} E[p_j], \\ &= \sum_{i=1}^{N} (E[p_i])^2 + \sum_{i=1}^{N}\sum_{j=1,j\neq i}^{N} E[p_i]E[p_j].\end{aligned} \qquad (B.4)$$

But, p_i, p_j, $i \neq j$, are independent random variables. Since they are independent, they are also uncorrelated, which implies

$$E[p_i p_j] = E[p_i]E[p_j] \quad \forall i \neq j. \qquad (B.5)$$

Substituting $(B.5)$ in $(B.4)$ yields

$$E\left[\sum_{i=1}^{N} p_i\right] E\left[\sum_{j=1}^{N} p_j\right] = \sum_{i=1}^{N} (E[p_i])^2 + E\left[\sum_{i=1}^{N}\sum_{j=1,j\neq i}^{N} p_i p_j\right]. \qquad (B.6)$$

Using $(B.6)$ in $(B.3)$ gives

$$\begin{aligned}\sigma_\theta^2 &= \frac{1}{N^2}\left\{E\left[\sum_{i=1}^{N} p_i\right] - \sum_{i=1}^{N} (E[p_i])^2\right\}, \\ &= \frac{1}{N^2}\sum_{i=1}^{N} \{E[p_i](1 - E[p_i])\}.\end{aligned} \qquad (B.7)$$

Since p_i can only take values of zero or unity,

$$0 \leq E[p_i] \leq 1,$$

which implies

$$0 \leq E[p_i](1 - E[p_i]) \leq \frac{1}{4}. \qquad (B.8)$$

Substituting $(B.8)$ in $(B.7)$ gives the following upper bound for the standard deviation:

$$\sigma_\theta \leq \frac{1}{2\sqrt{N}}. \qquad (B.9)$$

The estimate obtained above does not incorporate the dependence of the error on the scalar diffusivity, or the Peclet number. For any finite Peclet number, the error is indeed $O(N^{-1/2})$, but the specific Peclet number dependence cannot be easily extracted in this case. Some indication of the dependence of the error on the scalar diffusivity can be obtained in the simpler problem of conduction in a one-dimensional semi-infinite solid, which was considered as a test problem in §3.1. We consider this case below.

Using the notation of §3.1, the Wiener bundle solution at a point $z > 0$ at time t is again given by

$$\theta(z,t) = \frac{n(z,t)}{N},$$

where $n(z,t)$ is the number of Wiener trajectories that reach the heated boundary $z = 0$ over backward time t, and are terminated. N is the total number of particles released from point z at time t, as before. Again, one can define a discrete random variable $p_i(x,t),\ i = 1,\ldots,N$ for each of the N particles, and the calculations of above follow through to yield $(B.7)$ for the variance of θ. Now, in this case one can define

$$p_i = 1 - H(z_i(0)), \quad i = 1,\ldots,N,$$

where $H(\cdot)$ is the Heaviside step function and $z_i(0)$ is the z-coordinate of the i^{th} particle after backward integration of the corresponding Wiener trajectory over time t. Therefore,

$$E[p_i] = 1 - E[H(z_i(0))], \qquad (B.10)$$

where

$$E[H(z_i(0))] = \int_{-\infty}^{\infty} H(z_i(0))f(z_i(0))dz_i(0), \\ = \int_{0}^{\infty} f(z_i(0))dz_i(0), \tag{B.11}$$

and $f(z_i(0))$ is the probability density function for the distribution of Wiener initial points. Since the stochastic differential used to generate the backward Wiener trajectories is the one associated with the transient diffusion equation,

$$dz = (2D)^{1/2} dW_t,$$

with W_t now a one-dimensional Wiener process, it follows immediately that

$$f(z_i(0)) = \frac{1}{\sqrt{4\pi Dt}} e^{-(z_i(0)-z)^2/4Dt}, \tag{B.12}$$

i.e., the Wiener initial points are Gaussianly distributed with mean z and variance $2Dt$. Substituting $(B.10)$ in $(B.7)$ gives

$$\sigma_\theta^2 = \frac{1}{N^2} \sum_{i=1}^{N} \{E[H(z_i(0))](1 - E[H(z_i(0))])\}. \tag{B.13}$$

Now, regardless of the value of D,

$$0 \leq E[H(z_i(0))] \leq 1,$$

and again

$$\sigma_\theta \leq \frac{1}{2\sqrt{N}}.$$

But the dependence of the error on the conductivity or scalar diffusivity D is now transparent owing to the simple form of $(B.12)$. It is instructive to consider two limiting cases:

$$\lim_{D\to 0} E[H(z_i(0))] = \lim_{D\to 0} \int_0^\infty \frac{1}{\sqrt{4\pi Dt}} e^{-(z_i(0)-z)^2/4Dt} dz_i(0), \\ = \int_0^\infty \delta(z_i(0) - z) dz_i(0), \\ = 1,$$

which implies, from $(B.13)$,

$$\lim_{D\to 0} \sigma_\theta^2 = 0.$$

Contrastingly,

$$\begin{aligned}\lim_{D\to\infty} E[H(z_i(0))] &= \lim_{D\to\infty} \int_0^\infty \frac{1}{\sqrt{4\pi Dt}} e^{-(z_i(0)-z)^2/4Dt} dz_i(0), \\ &= \frac{1}{2},\end{aligned}$$

in which case, again from $(B.13)$,

$$\lim_{D\to\infty} \sigma_\theta^2 = \frac{1}{4N}.$$

The same analysis cannot be repeated for the advection-diffusion problem since the distribution of Wiener initial points is not easily obtained in that case.

We conclude that in general the error increases with increasing scalar diffusivity, or in the advection-diffusion case, with decreasing Peclet number. This is not surprising since the diffusive "jump" in a random-walk scheme is typically proportional to the square-root of the scalar diffusivity; for a given time-step Δt, this means the jump-lengths in a random-walk will be (typically) larger at increased scalar diffusivity, while the random-walk approximates the Wiener process only in the limit of infinitesimal jump-lengths.

B.2 Error estimate for the whole-field-random-walk algorithm

Obtained here is an error-estimate for the random-walk scheme for whole-field computations, developed in §3.1. From (3.5), the scalar value at a point x in the flow-domain, at time t, is given by

$$\theta(x,t) = \frac{n_{box}(x,t)}{N_d A_{box}}, \qquad (B.14)$$

where $n_{box}(x,t)$ is the number of particles at time t in a square box of size $A_{box} = \Delta x_1 \Delta x_2$, located at the point x. Suppose at time t there are N^t particles in the domain of the flow. To each of these N^t particles one may associate a discrete random variable $p_i(x,t)$, $i = 1,\ldots,N^t$, where $p_i(x,t) = 1$ if the i^{th} particle is in the box at x at time t, and $p_i(x,t) = 0$ otherwise. We shall consider x and t fixed, and henceforth suppress these dependences. Therefore, $(B.14)$ becomes

$$\theta = \frac{1}{N_d A_{box}} \sum_{i=1}^{N^t} p_i. \qquad (B.15)$$

The standard deviation of θ is a measure of the error.

A procedure identical to that in §B.1 yields the following expression for the variance of the random variable θ:

$$\sigma_\theta^2 = \frac{1}{(N_d A_{box})^2} \sum_{i=1}^{N^t} \{E[p_i](1 - E[p_i])\}, \qquad (B.16)$$

where $E[\cdot]$ again denotes expectation. Let $n \in \mathbf{N}$ be such that $0 \leq (N_d A_{box} - n) \leq 1$. Then, since the scalar value θ must be less than or equal to unity, it follows from $(B.15)$ that

$$\sum_{i=1}^{N^t} p_i \leq n.$$

Therefore, at least $N^t - n$ particles should have $p_i = 0$, and these will not contribute to the summation in $(B.16)$. Again, since

$$0 \leq E[p_i] \leq 1,$$

it follows that

$$\sigma_\theta^2 \leq \frac{n}{4(N_d A_{box})^2},$$

resulting in the following upper bound for the standard deviation:

$$\sigma_\theta \leq \frac{1}{2\sqrt{N_d A_{box}}},$$

and the error is therefore $O((N_d A_{box})^{-1/2})$. The dependence of the error on the Peclet number is expected to be similar to that outlined at the end of §B.1, but again we have no explicit closed-form analytical expression for the Peclet number dependence of the error.

Appendix C

Manifold emanation point for time-periodic flow over a plane wall

Shariff *et al.* (1991) generalized to the time-periodic case, the result for steady flow adjacent to a no-slip boundary that an invariant manifold emanates from the point of zero shear-stress. Their result of (3.11) applies only to manifolds emanating with non-zero slope. Here we shall show the result of (3.11) holds also for manifolds emanating with zero slope. Our result is precisely stated as follows: for two-dimensional time-periodic incompressible flows adjacent to a plane no-slip boundary, the necessary condition for a point on the no-slip boundary to have a one-dimensional (center) stable/unstable manifold for the corresponding Poincaré map, where the manifold is analytic at the emanation point, is given by (3.11). Applying to (2.9), condition (3.11) verifies the assumption in §2.2 that $\gamma_\beta^\pm(t) = \gamma^\pm(t)$. We shall also point out some properties of the Poincaré map, corresponding to the time-periodic advection field, in the vicinity of a point on the plane no-slip boundary, which find application in §5.3.

First we obtain a local Taylor-series representation of two-dimensional time-periodic incompressible flow near a non-hyperbolic stagnation point on a plane

no-slip boundary. Without loss of generality, the candidate point on the no-slip boundary is taken to be the origin of the series-expansion. Choosing rectangular coordinates (x_1, x_2), where x_1 is the coordinate along the wall and x_2 is the coordinate normal to the wall, writing the velocity vector $u(x_1, x_2, t)$ as an asymptotic expansion from the origin as in (2.1), and using the methods detailed in §2.1 to force the tensor coefficents in (2.1) to satisfy continuity, no-slip at the wall and the Navier-Stokes equations, yields the following second-order representation:

$$u_1 = A_{12}x_2 + 2A_{112}x_1x_2 + A_{122}x_2^2 + O(3), \qquad (C.1a),$$

$$u_2 = A_{222}x_2^2 + O(3), \qquad (C.1b),$$

where, from continuity, $A_{222} = -A_{112}$. The no-slip condition requires that all tensor coefficients, i.e., the $A_{ij\ldots}$'s, that do not contain 2 among any of its indices except the first, must be identically zero:

$$A_{i111\ldots} = 0, \qquad (C.2)$$

the condition being valid at all orders. Continuity requires $\frac{\partial u_i}{\partial x_i} = 0$, which specifies

$$A_{iijk\ldots} = 0. \qquad (C.3)$$

Since $(C.2)$ implies $A_{11} = 0$, $A_{111} = 0, \ldots$, and so on, we can factor out x_2 in $(C.1a)$. Combining $(C.2)$ and $(C.3)$ yields

$$A_{2211\ldots} = 0,$$

i.e., $A_{221} = 0$, $A_{2211} = 0, \ldots$, and so on. Thus we can factor out x_2^2 in $(C.1b)$. Expressing $(C.1)$ in terms of the partial derivatives of the velocity vector,

$$\begin{aligned} u_1 &= x_2[u_{1,2}(t) + \frac{1}{2}u_{1,22}(t)x_2 + u_{1,12}(t)x_1 + O(2)], \\ u_2 &= x_2^2[u_{2,22}(t) + O(1)]. \end{aligned} \qquad (C.4)$$

The partial derivatives are evaluated at $(0,0)$ and are periodic functions of t, with period T. We restrict attention to an $O(\epsilon)$ neighborhood of the origin. Taking initial point $(x_1(t_0), x_2(t_0))$ within $O(\epsilon)$ of $(0,0)$, the velocity field of $(C.4)$ is integrated to consistent order (see Shariff *at al.* 1991) to yield

$$\begin{aligned} x_1(t_0+T) - x_1(t_0) &= x_2(t_0)[\hat{u}_{1,2}(T) + x_1(t_0)\hat{u}_{1,12}(T) + x_2(t_0)C(T;t_0) + O(\epsilon^2)], \\ x_2(t_0+T) - x_2(t_0) &= x_2^2(t_0)[\frac{1}{2}\hat{u}_{2,22}(T) + O(\epsilon)], \end{aligned} \tag{C.5}$$

where $C(T;t_0)$ is given by

$$\begin{aligned} C(T;t_0) = \frac{1}{2}\hat{u}_{1,22}(T) + \int_{t_0}^{t_0+T} u_{1,2}(t)[\frac{1}{2}\hat{u}_{2,22}(t;t_0) - \hat{u}_{1,12}(t;t_0)]dt \\ + \hat{u}_{1,2}(T)\hat{u}_{1,12}(T), \end{aligned} \tag{C.6}$$

and hats denote time-integrals, e.g.,

$$\hat{u}_{2,22}(t;t_0) = \int_{t_0}^{t} u_{2,22}(s)ds,$$

while when the integration is over time T, we drop t_0, e.g.,

$$\hat{u}_{1,2}(T) = \int_{t_0}^{t_0+T} u_{1,2}(s)ds \equiv \int_0^T u_{1,2}(s)ds,$$

since the quantity becomes independent of initial time t_0 on account of the time-periodicity of the coefficients in $(C.4)$. We consider initial points based on the cross-section $\bar{\phi}$ of the Poincaré map $P^{\bar{\phi}}$ (see §2.2), and therefore let

$$\frac{\bar{\phi} - \phi_0}{\omega} = t_0,$$

where ϕ_0 is the initial phase of the velocity field in $(C.4)$, and $\omega = 2\pi/T$ is the frequency of the time-periodic velocity field. To simplify the notation, we replace (x_1, x_2) by (x, y), From $(C.5)$, the Poincaré map $P^{\bar{\phi}}$, locally near $(0,0)$, is given by

$$\begin{aligned} x_{i+1} &= x_i + y_i[\hat{u}_{1,2}(T) + \hat{u}_{1,12}(T)x_i + C(T;t_0)y_i + O(2)], \\ y_{i+1} &= y_i + y_i^2[\frac{1}{2}\hat{u}_{2,22}(T) + O(1)]. \end{aligned} \tag{C.7}$$

We seek a one-dimensional curve, emanating from $(0,0)$, that is invariant near the origin under the map $(C.7)$. We use power-series expansions, so we do require that this one-dimensional invariant manifold be analytic at (0,0). Let the invariant curve be given by

$$y_i = a_n x_i^n + a_{n+1} x_i^{n+1} + \cdots, \tag{C.8}$$

where $n \in \mathbf{N}$ specifies the lowest-order non-zero term in the series-representation of the invariant curve near the origin. Invariance requires

$$y_{i+1} = a_n x_{i+1}^n + a_{n+1} x_{i+1}^{n+1} + \cdots, \tag{C.9}$$

where (x_{i+1}, y_{i+1}) is given by $(C.7)$. Substituting $(C.7)$ in $(C.9)$ and using $(C.8)$ to write terms containing y_i in terms of x_i, gives

$$\begin{aligned} & a_n x_i^n \\ & + a_{n+1} x_i^{n+1} + a_{n+2} x_i^{n+2} + \cdots \\ & + O(x_i^{2n}) - a_n [x_i + \hat{u}_{1,2}(T) a_n x_i^n + O(x_i^{n+1}) + O(x_i^{2n})]^n \\ & - a_{n+1} [x_i + O(x_i^n)]^{n+1} - a_{n+2} [x_i + O(x_i^n)]^{n+2} - \cdots = 0. \end{aligned} \tag{C.10}$$

Expanding out each of the terms in the last line of $(C.10)$ and cancelling out with terms on the second line shows the lowest-order terms remaining from the last line are $O(x_i^{2n})$. Therefore, expanding out the second term on the third line shows the lowest-order term on the left-hand side of $(C.10)$ is $O(x_i^{n-1} \cdot x_i^n) = O(x_i^{2n-1})$, with coefficient $-a_n^2 \hat{u}_{1,2}(T)$. Hence, invariance requires

$$-a_n^2 \hat{u}_{1,2}(T) = 0 \quad \forall n \in \mathbf{N}. \tag{C.11}$$

Thus for any n, $a_n \neq 0$ if and only if

$$\hat{u}_{1,2}(T) = 0. \tag{C.12}$$

we therefore have the result that $(C.12)$ is a necessary condition for $(0,0)$ to have an analytic invariant manifold. Note that $(C.12)$ is only a necessary but not sufficient condition. For $n = 1$, $(C.12)$ is the result of (3.11).

Specializing $(C.10)$ to $n = 1$, i.e., the non-zero-slope-case, setting $\hat{u}_{1,2}(T) = 0$, and writing out terms up to $O(x_i^2)$, which is now the lowest-order term, gives

$$a_1^2 \frac{1}{2} \hat{u}_{2,22}(T) - a_1^2 \hat{u}_{1,12}(T) - a_1^2 C(T;t_0) = 0. \qquad (C.13)$$

Since we are seeking non-zero a_1, $(C.13)$ yields

$$a_1 = \frac{\frac{1}{2}\hat{u}_{2,22}(T) - \hat{u}_{1,12}(T)}{C(T;t_0)}, \qquad (C.14)$$

where $C(T;t_0)$ of $(C.6)$ is evaluated at $\hat{u}_{1,2}(T) = 0$. Since continuity requires $\hat{u}_{2,22}(t) = -\hat{u}_{1,12}(t)$, it immediately follows that $\hat{u}_{2,22}(t;t_0) = -\hat{u}_{1,12}(t;t_0)$ and $\hat{u}_{2,22}(T) = -\hat{u}_{1,12}(T)$. Substituting in $(C.14)$ and using $(C.6)$ gives

$$a_1 = \frac{-3\hat{u}_{1,12}(T)}{\hat{u}_{1,22}(T) - 3\int_{t_0}^{t_0+T} u_{1,2}(t)\hat{u}_{1,12}(t;t_0)dt}, \qquad (C.15)$$

and we have recovered Shariff *et al.*'s result for the non-zero slope (see Equation (19), Shariff *et al.* 1991). While $(C.12)$ is a necessary condition, from $(C.15)$,

$$\hat{u}_{1,12}(T) \neq 0, \qquad (C.16)$$

is a sufficient condition for the manifold to emanate with non-zero slope. It is easily verified from (2.9) that conditions $(C.12)$ and $(C.16)$ are satisfied at $(x_1, x_2) = (\pm 1, 0)$. Therefore, $p^{\pm}$ not only persist as points of zero shear-stress, but are also the manifold emanation points for $\beta \neq 0$, and the manifolds emanate with non-zero slope; an easy calculation gives $a_1 = 1/2$ at $(x_1, x_2) = (-1, 0) \equiv p^-$ and $a_1 = -1/2$ at $(x_1, x_2) = (1, 0) \equiv p^+$. Note from $(C.15)$ that in general the value of the non-zero slope can vary with the cross-section t_0 (equivalently, $\bar{\phi}$) of the Poincaré map, but

the manifold emanation point being the point on the no-slip boundary at which $(C.12)$ is satisfied, is independent of t_0 and therefore does not vary with the cross-section of the Poincaré map $P^{\bar{\phi}}$. This immediately implies $\gamma^{\pm}_{\beta}(t) = \gamma^{\pm}(t)$ in §2.2.

Next, we point out some important properties of the Poincaré map $P^{\bar{\phi}}$ of $(C.7)$, corresponding to the chaotic advection field of (2.9) in an $O(\epsilon)$ neighborhood of p^-. At $p^- \equiv (-1, 0)$, $u_{1,2}(t) = 0$ and hence $\hat{u}_{1,2}(T) = 0$. It follows then from $(C.7)$,

$$P^{\bar{\phi}} \equiv P_\beta = \mathbf{I} + O(\epsilon^2),$$

$$\Rightarrow dP_\beta = \mathbf{I} + O(\epsilon),$$

where $\mathbf{I}$ is the Identity map. Since P_β is a diffeomorphism, dP_β is an isomorphism, and we may take the inverse to obtain (Kato 1980)

$$dP_\beta^{-1} = \mathbf{I} + O(\epsilon). \qquad (C.17)$$

By integrating $(C.4)$ in backward time over the time-interval T, one can obtain an explicit expression for $(P^{\bar{\phi}})^{-1}$, near $(0, 0)$. In fact, it is easily shown that

$$(P^{\bar{\phi}})^{-1} = \mathbf{I} + O(\epsilon^2),$$

and this of course holds for P_β^{-1} near p^-.

Finally, we note that an existence and uniqueness theorem for invariant manifolds of a non-hyperbolic stagnation point on a plane no-slip boundary in two-dimensional time-periodic incompressible flow is still lacking. McGehee (1973) has proved a stable manifold theorem for an isolated non-hyperbolic fixed point. Casasayas, Fontich & Nunes (1992) do consider a class of two-dimensional maps having the origin as a non-hyperbolic fixed point and degenerate in the sense that it has a line of fixed points through it, but restrict attention to the non-area preserving case. Their methods do not generalize to the area-preserving case, and hence do not apply to incompressible flows.

Appendix D

Mean-square convergence of the discrete random processes of (5.1) and (5.2)

Let the time-step $\triangle t$ in (5.2) be given by $\triangle t = \frac{T}{M}$, $M \in \mathbf{N}$, M fixed and sufficiently large such that the discrete random process satisfying (5.2) approximates the stochastic process satisfying (3.3). Let $\{x^{nM}\}_{n=N}^{0}$ be a trajectory generated by (5.2) and $\{y^n\}_{n=N}^{0}$ be a trajectory generated by (5.1), with same fixed non-random initial point , $x^0 = y^0$. We shall show that $\forall\ n \in [0, N]$,

$$\lim_{Pe \to \infty} < |x^{nM} - y^n|^2 >= 0,$$

where again $< \cdot >$ denotes expectation and $|\cdot|$ the standard Euclidean norm in $\mathbb{R}^2$.

By the triangle inequality,

$$|x^{nM} - y^n| \leq |x^{nM} - f^n(x^0)| + |y^n - f^n(x^0)|.$$

Squaring and taking the expectation on both sides of the inequality,

$$< |x^{nM} - y^n|^2 > \leq < F_1 > + < F_2 > + < F_3 >,$$

where

$$F_1 = |x^{nM} - f^n(x^0)|^2,$$

$$F_2 = |y^n - f^n(x^0)|^2,$$

$$F_3 = 2|x^{nM} - f^n(x^0)| \cdot |y^n - f^n(x^0)|.$$

But $F_1 \equiv F_1(\eta, \xi)$, and since η, ξ are independent Gaussianly distributed random variables,

$$< F_1 >= \int_{-\infty}^{\infty} \int_{-\infty}^{\infty} F_1(\eta, \xi) w(\eta) w(\xi) d\eta d\xi,$$

where $w(\cdot)$ is a Gaussian distribution with mean zero and variance $2\triangle t/Pe$. But $w(\eta)w(\xi)$ is a smooth non-negative function satisfying $\int_{-\infty}^{\infty} \int_{-\infty}^{\infty} w(\eta)w(\xi)d\eta d\xi = 1$. Therefore $k^2 w(k\eta)w(k\xi)$, $k \in \mathbf{N}$, is a two-dimensional δ-sequence (Greenberg 1978), and since $F_1(\eta, \xi)$ is continuous at $(\eta,\ \xi) = (0, 0)$,

$$\lim_{k \to \infty} \int_{-\infty}^{\infty} \int_{-\infty}^{\infty} F_1(\eta, \xi) k^2 w(k\eta) w(k\xi) d\eta d\xi = F_1(0, 0).$$

Letting $Pe = k^2 \bar{Pe}$, $\bar{Pe}$ arbitrary but finite, it follows easily that $\lim_{Pe \to \infty} < F_1 > = F_1(0, 0)$. Since

$$x^{nM} = g_{nM-1}(g_{nM-2}(\cdots(g_0(x^0) + \rho)\cdots) + \rho) + \rho,$$

at $\rho \equiv (\eta,\ \xi) = (0, 0)$

$$F_1 = g_{nM-1} \circ g_{nM-2} \circ \cdots \circ g_0(x^0) - f^n(x^0) = 0.$$

Therefore, we have shown that

$$\lim_{Pe \to \infty} < F_1 >= 0.$$

Noting that $F_2 \equiv F_2(\eta_T, \xi_T)$ and $F_3 \equiv F_3(\eta, \xi, \eta_T, \xi_T)$, where η, ξ, η_T, ξ_T are all independent Gaussianly distributed random variables, the limiting forms of the terms $< F_2 >$ and $< F_3 >$ can be obtained in a manner very similar to that mentioned above, yielding

$$\lim_{Pe \to \infty} < F_2 > = 0 = \lim_{Pe \to \infty} < F_3 > .$$

The result clearly holds for every $n \in [0, N]$, which establishes the desired mean-square convergence.

References

Anosov, D.V. 1967 Geodesic flows on closed Riemannian manifolds with negative curvature. *Proc. Steklov Inst. Math.* **90**, 1; (Amer. Math. Soc. translation 1969).

Aref, H. 1984 Stirring by chaotic advection. *J. Fluid Mech.* **143**, 1.

Aref, H. & Jones, S.W. 1989 Enhanced separation of diffusing particles by chaotic advection. *Phys. Fluids* A**1**, 470.

Arnold, L. 1974 *Stochastic Differential Equations.* Wiley.

Batchelor, G.K. 1956 Steady laminar flow with closed streamlines at large Reynolds number. *J. Fluid Mech.* **1**, 177.

Bowen, R. 1975 ω-limit sets for Axiom A diffeomorphisms. *J. Diff. Eqns.* **18**, 333.

Camassa, R. & Wiggins, S. 1991 Chaotic advection in a Rayleigh-Bénard flow. *Phys. Rev.* A**43**, 774.

Carslaw, H.S. & Jaeger, J.C. 1959 *Conduction of Heat in Solids.* Oxford Univ. Press.

Casasayas, J., Fontich, E. & Nunes, A. 1992 Invariant manifolds for a class of parabolic points. *Nonlinearity* **5**, 1193.

Chandrasekhar, S. 1943 Stochastic problems in Physics and Astronomy. *Rev. Mod. Phys.* **15**, 1.

Chorin, A.J. 1973 Numerical study of slightly viscous flow. *J. Fluid Mech.* **57**, 785.

Chorin, A.J. & Marsden, J.E. 1979 *A Mathematical Introduction to Fluid Mechanics.* Springer.

Chow, S-N., Lin, X-B. & Palmer, K.J. 1989 A shadowing lemma with applications to semilinear parabolic equations. *SIAM J. Math. Anal.* **20**(3), 547.

Dallmann, U. 1988 Three-dimensional vortex structures and vorticity topology. *Fluid Dynamics Res.* **3**, 183.

Easton, R.W. 1986 Trellises formed by stable and unstable manifolds in the plane. *Trans. Amer. Math. Soc.* **294**(2), 719.

Eckart, C. 1948 An analysis of the stirring and mixing processes in incompressible fluids. *J. Mar. Res.* **7**, 265.

Farmer, J.D. & Sidorowich, J.J. 1991 Optimal shadowing and noise reduction. *Physica D* **47**, 373.

Fenichel, N. 1971 Persistence and smoothness of invariant manifolds for flows. *Indiana Univ. Math. J.* **21**, 193.

Ghosh, S., Chang, H-C. & Sen, M. 1992 Heat-transfer enhancement due to slender recirculation and chaotic transport between counter-rotating eccentric cylinders. *J. Fluid Mech.* **238**, 119.

Greenberg, M.D. 1978 *Foundations of Applied Mathematics.* Prentice-Hall.

Grebogi, C., Hammel, S.M., Yorke, J.A. & Sauer, T. 1990 Shadowing of physical trajectories in chaotic dynamics: containment and refinement. *Phys. Rev. Lett.* **65**, 1527.

Guckenheimer, J. & Holmes, P. 1983 *Nonlinear Oscillations, Dynamical Systems, and Bifurcations of Vector Fields.* Springer.

Haji-Sheikh, A. & Sparrow, E.M. 1967 The solution of heat conduction problems

by probability methods. *J. Heat Transfer, Trans ASME Series C* **89**, 121.

Hammel, S.M. 1990 A noise reduction method for chaotic systems. *Phys. Lett.* A**148**, 421.

Hammel, S.M., Yorke, J.A. & Grebogi, C. 1987 Do numerical orbits of chaotic dynamical processes represent true orbits? *J. Complexity* **3**, 136.

Hammel, S.M., Yorke, J.A. & Grebogi, C. 1988 Numerical orbits of chaotic processes represent true orbits. *Bull. Amer. Math. Soc.* **19**, 465.

Hirsch, M.W., Pugh, C.C. & Shub, M. 1977 *Invariant Manifolds.* Springer Lecture Notes in Mathematics, Vol. 583, Springer.

Jones, S.W. 1991 The enhancement of mixing by chaotic advection. *Phys. Fluids* A**3**, 1081.

Kato. T. 1980 *Perturbation Theory for Linear Operators.* Springer.

Khakhar, D.V. & Ottino, J.M. 1986 Fluid mixing (stretching) by time-periodic sequences of weak flows. *Phys. Fluids* **29**, 3503.

Klapper, I. 1991 Chaotic fast dynamos. Dissertation, Courant Institute of Mathematical Sciences, New York University.

Klapper, I. 1992a Shadowing and the role of small diffusivity in the chaotic advection of scalars. *Phys. Fluids* A**4**(5), 861.

Klapper, I. 1992b A study of fast dynamo action in chaotic helical cells. *J. Fluid Mech.* **239**, 359.

Ladyzhenskaya, O.A. 1975 Mathematical analysis of Navier-Stokes equations for incompressible flows. *Ann. Rev. Fluid Mech.* **7**, 249.

McGehee, R. 1973 A stable manifold theorem for degenerate fixed points with applications to celestial mechanics. *J. Diff. Eqns.* **14**, 70.

McKean, H.P. 1969 *Stochastic Integrals.* Academic.

Melnikov, V.K. 1963 On the stability of the center for time periodic perturbations. *Trans. Moscow Math. Soc.* **12**, 1.

Molchanov, S.A., Ruzmaikin, A.A. & Sokolov, D.D. 1985 Kinematic dynamo action in random flow. *Sov. Phys. Usp.* **28**, 307.

Pan, F.Y. & Acrivos, A. 1968 Heat transfer at high Péclet number in regions of closed streamlines. *Int. J. Heat Mass Transfer* **11**, 439.

Perry, A.E. & Chong, M.S. 1986a A series-expansion study of the Navier-Stokes equations with applications to three-dimensional separation patterns. *J. Fluid Mech.* **173**, 203.

Perry, A.E. & Chong, M.S. 1986b A series-expansion study of the Navier-Stokes equations with applications to three-dimensional separation patterns - a detailed treatment. *Rep.* FM-17, Mech. Engr. Dept. , University of Melbourne.

Press, W.H., Flannery, B.P., Teukolsky, S.A. & Vetterling, W.T. 1986 *Numerical Recipes.* Cambridge University Press.

Rhines, P.B. & Young, W.R. 1983 How rapidly is a passive scalar mixed within closed streamlines? *J. Fluid Mech.* **133**, 133.

Rom-Kedar, V., Leonard, A. & Wiggins, S. 1990 An analytical study of transport, mixing, and chaos in an unsteady vortical flow. *J. Fluid Mech.* **214**, 347.

Sanders, J.A. 1982 Melnikov's method and averaging. *Celestial Mechanics* **28**, 171.

Saffman, P.G. 1959 A theory of dispersion in porous medium. *J. Fluid Mech.* **6**, 321.

Shariff, K., Pulliam, T.H. & Ottino, J.M. 1991 A dynamical systems analysis of

kinematics in the time-periodic wake of a circular cylinder. *Lectures in Ap. Math.* **28**, 613.

Smale, S. 1967 Differentiable dynamical systems. *Bull. Amer. Math. Soc.* **73**, 747.

Tobak, M. & Peake, D.J. 1982 Topology of three-dimensional separated flows. *Ann. Rev. Fluid Mech.* **14**, 61.

Wang, M.C. & Uhlenbeck, G.E. 1945 On the theory of the Brownian motion II. *Rev. Mod. Phys.* **17**, 323.

Weiss, J.B. & Knobloch, E. 1989 Mass transport and mixing by modulated traveling waves. *Phys. Rev.* A**40**(5), 2579.

Wiggins, S. 1990 *Introduction to Applied Nonlinear Dynamical Systems and Chaos.* Springer.

Wiggins, S. 1992 *Chaotic Transport in Dynamical Systems.* Springer.

PART II

Convection-diffusion near a point of laminar separation in a two-dimensional boundary-layer

Chapter 1

Introduction

The transport of a passive scalar such as heat or dye into a steady convecting fluid across laminar boundary-layers can be studied in two asymptotic limits : one where advection dominates over diffusion and vice-versa. The important parameter is the Peclet number, $Pe = UL/D$, where U and L are the characteristic velocity and length scales of the flow and D is the molecular or thermal diffusivity. Pe is , therefore, the ratio of the diffusion time scale L^2/D to the convection time scale L/U, and reflects the relative importance of advection and diffusion in the convection-diffusion or thermal energy equation. In the large-Peclet-number limit, asymptotic results for two-dimensional laminar forced-convection heat or mass transfer are well known (Lighthill 1950, Morgan & Warner 1956, Acrivos & Goddard 1965). In the case of heat transfer from a stationary heated surface to a convecting fluid at large Pe, the transport process is convectively dominant everywhere except in a thermal boundary-layer adjacent to the hot surface, where conduction normal to the surface is balanced by convection. If the Prandtl number is also large, the thermal boundary-layer is very narrow compared to the velocity boundary-layer and temperature variations are confined to a thin region near the surface. However, in many laminar fluid flows, the velocity boundary-layer separates from the no-slip

boundary due to an adverse pressure gradient, resulting in reversed flow (Sclichting 1962). At the point of laminar separation the wall shear-stress vanishes and, in the case of two-dimensional flows, a dividing streamline emanates from the separation-point on the wall. One therefore expects a thickening of the thermal boundary-layer near the point of separation, and convection along the dividing streamline acts as a important physical mechanism for lifting heat or a passive impurity from the wall. The well-known results of two-dimensional laminar forced-convection heat transfer (Lighthill 1950, Morgan & Warner 1956, Acrivos & Goddard 1965) do not apply in the vicinity of a separation point, where the flow and the resulting convective transport is no longer dominantly parallel to the no-slip boundary and the standard thermal boundary-layer approximations break down (Acrivos & Goddard 1965).

In the terminology of dynamical systems theory, the separation point on the wall is a "non-hyperbolic fixed point" and the dividing streamline is its "one-dimensional unstable manifold." Since the entire no-slip boundary is a singular manifold with every point on it a non-hyperbolic fixed point, it is more convenient to use a term that distinguishes the separation point from the other non-hyperbolic fixed points on the boundary: no-slip critical point – which has been used in applications of critical-point theory to fluid flow patterns (Perry & Chong 1987). A no-slip critical point is a point on a no-slip boundary where the vorticity vector vanishes. It is more appropriate to use this term in place of "separation point," since we are interested in steady viscous flows that have the *topology* of a plane separated flow locally near the wall, which can therefore even arise in steady low Reynolds number flow past a rigid body and thus not necessarily due to the physical phenomenon of laminar separation. In all such flows, the one-dimensional unstable manifold of the no-slip critical point can be expected to have a considerable influence on the scalar field distribution for convection-diffusion of a passive scalar from

the wall. We study here the role of the one-dimensional unstable manifold of a no-slip critical point in steady heat transfer from the no-slip boundary at the small thermal diffusivity, large-Peclet-number, limit. This is part of a broader objective of detailing and characterizing the topology of separated flows (Tobak & Peake 1982) in terms of the distribution of "fixed points" (also called "stagnation points," or, "critical points") and "invariant manifolds," and the role played by these invariant curves and surfaces in the transport of a passive scalar, scalar field distribution, residence-times and fluxes.

We study steady heat transfer at large Peclet number near a no-slip critical point in a two-dimensional viscous flow that is symmetrical about the critical point. A hot spot at the wall is modeled as a local step change in temperature, with the step placed symmetrically about the critical point. The local streamlines are identical to that in normal plane stagnation flow (Hiemenz flow) in the vicinity of the stagnation point, but with the direction of flow reversed. We call our flow "normal plane separated flow." Figure 1.1 shows the streamlines in normal plane separated flow. The heat transfer problem, however, will clearly bear little or no similarity with that for the normal plane stagnation flow, because now we can expect convection of heat normal to the wall to contribute to dominant order, locally near the critical point. We obtain a viscous, incompressible, two-dimensional flow that has the topology of a normal plane separated flow in the form of a Taylor-series expansion from the no-slip critical point, which is also an asymptotically exact solution of the Navier-Stokes and continuity equations. The Taylor-series expansion method (Perry & Chong 1986, Dallmann 1983) assumes the solutions of the continuity and Navier-Stokes equations for incompressible flow are smooth; conditions for the validity of such an assumption have been examined by Ladyzhenskaya (1975).

The advantage of the Taylor-series expansion method is that one can generate

laminar boundary-layer flows, especially separation patterns with desired topological features, as local Taylor-series expansions to arbitrary order without regard to the outer inviscid flow. We are seeking an asymptotic representation of the steady large-Pe temperature field locally near the no-slip critical point and a Taylor-series expansion of the velocity field truncated to leading-order will turn out to be sufficient for the purposes of our asymptotic analysis. We note in passing that this holds only when the temperature variations are confined to a region that shrinks closer to the no-slip critical point with increasing Peclet number. The representation of the temperature field is then asymptotically exact in the vicinity of the critical point at the limit of large Pe. An interesting counter-example is the similar large-Pe convection-diffusion problem of transport of a passive scalar near the no-slip critical point in steady, viscous, incompressible axisymmetric flow over an active no-slip surface. A local approximation of the velocity field in a viscous flow with the desired topology can again be constructed in the form of an asymptotic expansion from the critical point. But, as we demonstrate in the Appendix, higher order terms in the velocity field contribute to dominant order in the large-Pe asymptotic representation of the temperature field since the thermal boundary-layer grows away from the critical point with increasing Peclet number. In that case, an asymptotic leading-order representation of the local velocity field does not serve any useful purpose and it illustrates the limitations of the method as an aid in seeking local asymptotic solutions to convection-diffusion problems. With the local representation of steady, viscous, incompressible flow near the no-slip critical point in normal plane separated flow, we solve for the steady temperature field in the asymptotic limit of large Peclet number using the method of matched asymptotic expansions. The matched asymptotic expansion method has been applied previously by others (Shraiman 1987, Nadim, Cox & Brenner 1986) to handle the convection-diffusion

problem near stagnation points at the singular limit of large Peclet number or vanishingly small molecular diffusivity, but the spatial periodicity of their flow and the consequent spatial periodicity of the thermal boundary-layer solution results in an extra "consistency condition," which renders their problem much different from ours.

The organization of this part of the thesis is as follows: in Chapter 2 we obtain the local representation of a viscous, incompressible flow that has the topological features of a normal plane separated flow. In Chapter 3 we set up the heat transfer problem, delineate the various convective-diffusive regimes and distinguish one "outer" region and three "inner" regions. We also solve for the asymptotic temperature field in the outer region. In Chapter 4 we consider the three inner regions. In Chapter 5 we complete our solution by "matching" the different convective-diffusive regimes using the method of matched asymptotic expansions. We also remark on the possible existence of other convective-diffusive regimes. In Chapter 6 we compare our asymptotic representation with a numerical computation of point values of the temperature field at large Peclet number, using a Monte Carlo scheme based on the Wiener bundle solution. We also discuss the advantage offered by the Wiener bundle method in comparison to other numerical schemes, in the context of our large-Pe transport problem. Additionally, a whole field numerical computation is carried out at two moderately large Peclet numbers using finite-differences, to further verify the predictions of the asymptotic theory. We end with some concluding remarks in Chapter 7. The Appendix contains a brief discussion of a similar scalar transport problem that illustrates a case where a local Taylor-series representation of the velocity field is of limited usefulness.

FIGURES

Figure 1.1: Streamlines in normal plane separated flow.

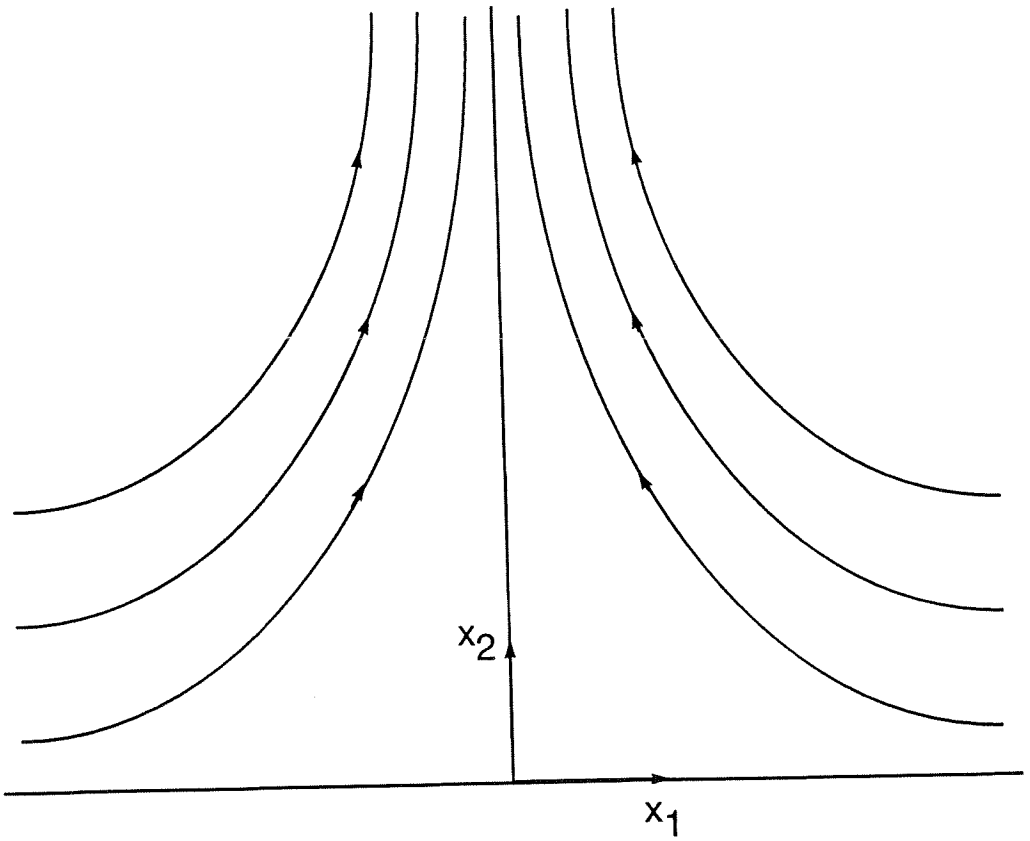

Figure 1.1

Chapter 2

Velocity field in normal plane separated flow

We apply the method developed by Perry & Chong (1986) and Dallmann (1983) to obtain a local approximation of the velocity field in normal plane separated flow. The velocity vector $u(x)$, $x \in \mathbb{R}^2$, $u \in \mathbb{R}^2$, is written in the form of an asymptotic expansion from the origin

$$u_i = A_i + A_{ij}x_j + A_{ijk}x_jx_k + A_{ijkl}x_jx_kx_l + O(4), \tag{2.1}$$

where the $i, j, k..$'s can take on values of 1 or 2 since our flow is two-dimensional, and $O(m)$ represents a homogeneous polynomial of degree $n \geq m$. The basic idea behind the method is to force the tensor coefficients $A_{ijk..}$'s to satisfy the Navier-Stokes and continuity equations, as well as boundary and symmetry conditions. The number of unknown tensor coefficients is greater than the number of equations generated from the Navier-Stokes equations, continuity equations and no-slip constraints, and the difference between the number of unknown coefficients and the number of connecting relationships grows rapidly with increasing order of the expansion. The undetermined coefficients can be regarded as parameters in the vector field and are often associated with the vorticity distribution in the flow.

The origin of our rectangular coordinates is chosen to be the no-slip critical

point (see figure 1.1), and a third-order expansion from the critical point is constructed. Since both velocity and shear-stress vanish at the no-slip critical point, the A_i's and the A_{ij}'s are all zero. By forcing the remaining coefficients to satisfy the equations of continuity and Navier-Stokes, no-slip constraints and symmetry about the x_2-axis, we obtain

$$\begin{aligned} u_1 &= -2K_1 x_1 x_2 - 3K_2 x_1 x_2^2 + O(4), \\ u_2 &= K_1 x_2^2 + K_2 x_2^3 + O(4). \end{aligned} \tag{2.2}$$

The parameter K_1 is related to the shear-stress distribution at the wall and K_2 is naturally associated with the vorticity distribution in the flow. We are of course assuming steady flow. For positive values of K_1, K_2, the asymptotic third-order expansion of (2.2) has the topological structure of normal plane separated flow, locally near the no-slip critical point. We therefore assume $K_1, K_2 > 0$. Since we are dealing with incompressible flow, we set

$$u_1 = \frac{\partial \psi}{\partial x_2}, u_2 = -\frac{\partial \psi}{\partial x_1}, \tag{2.3}$$

to obtain the stream function

$$\psi(x_1, x_2) = -K_1 x_1 x_2^2 - K_2 x_1 x_2^3 + O(5), \tag{2.4}$$

$\psi = 0$ at $x_2 = 0$. It is important to note the generality of this formulation: for any viscous boundary-layer with the topological structure of normal plane separated flow , an asymptotic expansion from the no-slip critical point of the stream function describing the flow will always have the form given by (2.4), irrespective of the particular nature of the inviscid "outer" flow.

Chapter 3

The boundary-value problem at large Peclet number

We consider steady heat transfer from the stationary no-slip boundary of a normal plane separated flow; the equations and the physics of the transport mechanism apply to the transport of any passive scalar. Without any loss of generality, the no-slip critical point of the normal plane separated flow is taken to be the origin of our rectangular coordinates, as shown in figure 1.1. The x_2-axis is then the dividing streamline, or one-dimensional unstable manifold of the critical point. Let T_w be the temperature at the wall ($x_2 = 0$) from $x_1 = -L$ to $x_1 = L$, and T_a the temperature everywhere else on the wall and in the far field. Moreover, we assume $T_w > T_a$, and therefore heat is transmitted from the wall into the fluid. We begin with the steady-state thermal energy equation for constant property incompressible flows

$$\frac{\partial \psi}{\partial x_2}\frac{\partial T}{\partial x_1} - \frac{\partial \psi}{\partial x_1}\frac{\partial T}{\partial x_2} = \alpha\left(\frac{\partial^2 T}{\partial x_1^2} + \frac{\partial^2 T}{\partial x_2^2}\right), \tag{3.1}$$

$x_1 \in (-\infty, +\infty)$, $x_2 \in (0, \infty)$. $T(x_1, x_2)$ is the temperature at any point in the flow and α is the thermal diffusivity of the fluid. We non-dimensionalise (3.1) by

defining dimensionless variables:

$$\theta = \frac{T - T_a}{T_w - T_a},\ \overline{x}_1 = \frac{x_1}{L},\ \overline{x}_2 = \frac{x_2}{L},\ \overline{\psi} = \frac{\psi}{K_1 L^3}.$$

In dimensionless variables, (3.1) becomes

$$\frac{\partial \overline{\psi}}{\partial \overline{x}_2}\frac{\partial \theta}{\partial \overline{x}_1} - \frac{\partial \overline{\psi}}{\partial \overline{x}_1}\frac{\partial \theta}{\partial \overline{x}_2} = \frac{\alpha}{K_1 L^3}\left(\frac{\partial^2 \theta}{\partial \overline{x}_1^2} + \frac{\partial^2 \theta}{\partial \overline{x}_2^2}\right). \tag{3.2}$$

Recognizing $K_1 L^3/\alpha$ as the Peclet number Pe, we obtain

$$P\theta = 0, \tag{3.3}$$

where P denotes the linear differential operator

$$P = \frac{\partial \psi}{\partial x_2}\frac{\partial}{\partial x_1} - \frac{\partial \psi}{\partial x_1}\frac{\partial}{\partial x_2} - \frac{1}{Pe}\left(\frac{\partial^2}{\partial x_1^2} + \frac{\partial^2}{\partial x_2^2}\right). \tag{3.4}$$

The overbars have been dropped and it will be understood that all variables are now dimensionless. The stream function, in terms of the dimensionless variables, becomes

$$\psi(x_1, x_2) = -x_1 x_2^2 - \lambda x_1 x_2^3 + O(5), \tag{3.5}$$

where $\lambda = K_2 L/K_1$. Equation (3.3), with the boundary conditions

$$\begin{aligned} \theta(|x_1| \to \infty, x_2) &= 0, \\ \theta(x_1, x_2 \to 0) &= 1 - H(|x_1| - 1), \\ \theta(x_1, x_2 \to \infty) &= 0, \end{aligned} \tag{3.6}$$

completely specifies the boundary-value problem. $H(\cdot)$ in (3.6) is the Heaviside step-function.

As is generally recognized, it is not feasible to derive exact solutions to such convection-diffusion problems for arbitrary Pe. One then looks for an asymptotic solution, such as the thermal boundary-layer solution to be considered here, which

may be regarded as the limiting form of the temperature field θ for large values of the Peclet number. The Reynolds number of the flow is defined as

$$Re = \frac{K_1 L^3}{\nu},$$

ν being the kinematic viscosity of the fluid. Therefore

$$Pe = RePr,$$

where

$$Pr = \nu/\alpha$$

is the Prandtl number of the fluid, κ being the thermal conductivity. In considering $Pe \to \infty$ we mean, in particular, Re fixed with $Pr \to \infty$.

A regular perturbation solution of (3.3) at $Pe \to \infty$ yields

$$\{\theta^r, \psi\} = 0, \tag{3.7}$$

where $\{f(x_1, x_2), g(x_1, x_2)\}$ denotes the Poisson bracket of the two functions, f and g. Since ψ is a time-independent Hamiltonian, (11) implies

$$\theta(x_1, x_2) = \theta^r(\psi(x_1, x_2)) + O(Pe^{-1}). \tag{3.8}$$

The regular perturbation solution at the small thermal-diffusivity, large-Peclet-number, limit neglects diffusion to leading-order and specifies $\theta = O(Pe^{-1})$ everywhere except at the wall and along the dividing streamline, where $\theta = 1 + O(Pe^{-1})$. Large temperature gradients then necessarily obtain in the vicinity of the wall and the dividing streamline, and in those regions we expect thermal boundary-layers where the conduction terms in (3.4) cannot be ignored, even at the asymptotic limit of $Pe \to \infty$. It therefore becomes necessary to derive "inner" equations, valid in the thermal boundary-layers at the wall and straddling the dividing streamline.

An inner-field analysis will involve a careful consideration of the domain near the no-slip critical point, termed here as the "transition region," which connects the boundary-layer at the wall with that straddling the dividing streamline. The possible existence of other convective-diffusive regimes interior to the transition region must also be recognized. Finally, since the flow field and the temperature boundary conditions are exactly symmetrical about the dividing streamline, we shall solve for the temperature field in the right-half plane; the solution in the left-half plane can be obtained from symmetry.

The near-wall boundary-layer is termed Region I, the transition region is termed Region II, the boundary-layer along the dividing streamline is termed Region III, and the region outer to the thermal boundary-layers is termed Region IV. These are outlined in figure 3.1. In Region IV, x_1 and x_2 are both $O(1)$ and hence in the large-Peclet-number limit one obtains an "outer" solution identical to the regular perturbation solution of (3.8)

$$\theta(x_1, x_2) = \theta^{IV}(\psi(x_1, x_2)) + O(Pe^{-1}), \tag{3.9}$$

where θ^{IV} denotes the $O(1)$ temperature field in Region IV. Since we can only apply the far field boundary conditions in Region IV, it follows that the temperature along all streamlines in Region IV is $O(Pe^{-1})$ and, hence,

$$\theta^{IV} = 0 \tag{3.10}$$

everywhere in Region IV. This will be used as a "matching condition" in our inner-field analysis, which we perform in the next section.

FIGURES

Figure 3.1: Convective-diffusive regimes.

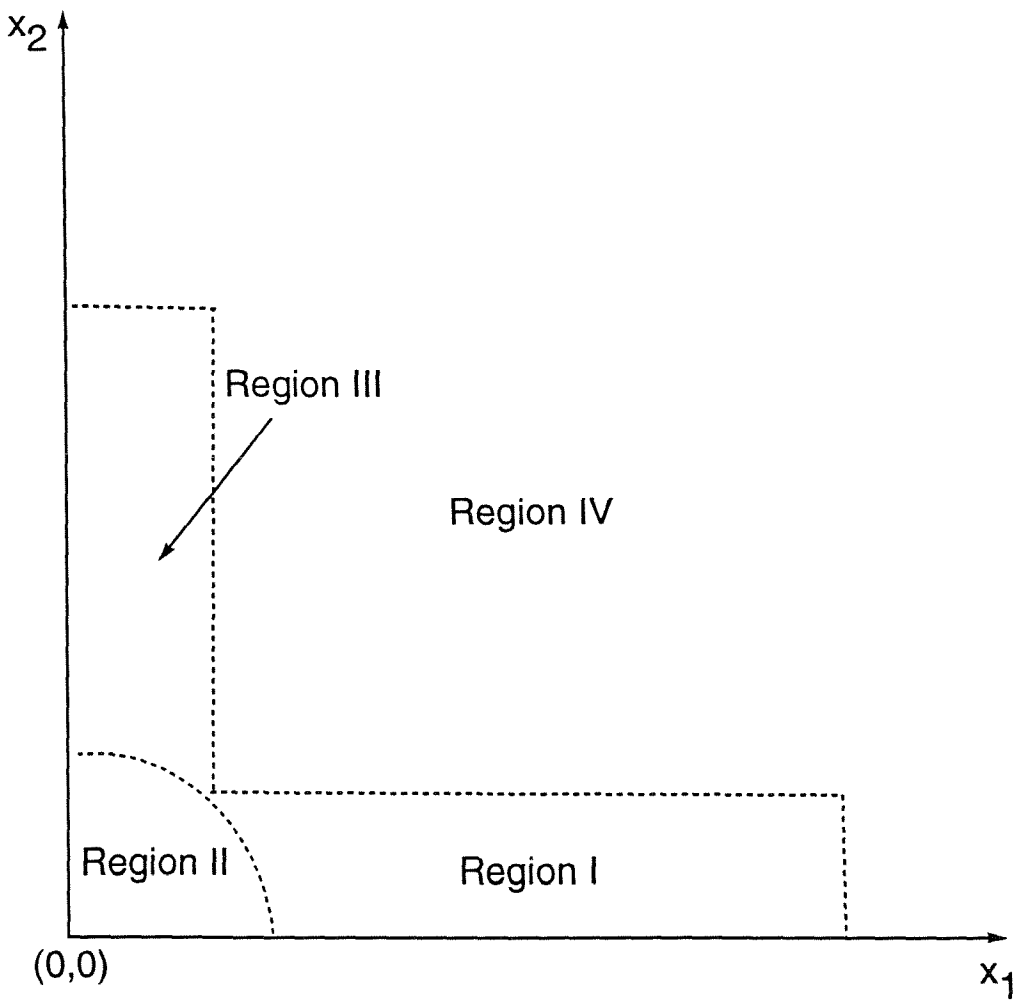

Figure 3.1

Chapter 4

Inner analysis

4.1 Region I

One recalls at this point that, in the limit $Pe \to \infty$, such that $Pr \to \infty$ with Re fixed, the near-wall thermal boundary-layer is much thinner than the velocity boundary-layer and the asymptotic expression for the differential operator P of (3.4) depends, primarily, on the limiting form of the stream function near $x_2 = 0$. From (3.5),

$$\psi(x_1, x_2) = -x_1 x_2^2 + O(x_2^3). \tag{4.1}$$

A conventional dominant balance argument, balancing convection with conduction normal to the wall, yields the appropriate scaled variable for the boundary-layer analysis (Morgan & Warner 1956, Levich 1962)

$$\hat{x}_2 = Pe^{1/3} x_2, \tag{4.2}$$

whereas x_1 is $O(1)$ in Region I. For convenience, we set $\hat{x}_1 = 1 - x_1$. In these new variables, the stream function becomes

$$\psi = Pe^{-2/3}(\hat{x}_1 - 1)\hat{x}_2^2 + O(Pe^{-1}), \tag{4.3}$$

and the differential operator P of (3.4) can be expressed as

$$P = Pe^{-1/3}(P_o + O(Pe^{-1/3})), \tag{4.4}$$

where

$$P_o \equiv 2(1-\hat{x}_1)\hat{x}_2\frac{\partial}{\partial \hat{x}_1} + \hat{x}_2^2\frac{\partial}{\partial \hat{x}_2} - \frac{\partial^2}{\partial \hat{x}_2^2}, \tag{4.5}$$

$\hat{x}_1 \in (0,1)$, $\hat{x}_2 \in (0,\infty)$. The ansatz

$$\theta = \theta^I(\hat{x}_1, \hat{x}_2) + O(Pe^{-1/3})$$

yields the following equation and boundary conditions, to leading-order:

$$P_o\theta^I = 0, \tag{4.6a}$$

$$\theta^I(\hat{x}_1, \hat{x}_2 \to 0) = 1, \tag{4.6b}$$

$$\theta^I(\hat{x}_1, \hat{x}_2 \to \infty) = 0, \tag{4.6c}$$

$$\theta^I(\hat{x}_1 \to 0, \hat{x}_2) = 0, \tag{4.6d}$$

where boundary condition (4.6c) is also the "matching condition" with the outer solution of (3.10). The equations of (4.6) represent, of course, the well-known boundary-layer approximation to the energy equation (Lighthill 1950, Morgan & Warner 1956). A transformation, introduced by Herbeck (1954), is applied to this case to obtain the following independent variables

$$\begin{aligned} \sigma &= \sqrt{2(1-\hat{x}_1)}\ \hat{x}_2, \\ \tau &= \frac{2\sqrt{2}}{3}[1-(1-\hat{x}_1)^{3/2}]. \end{aligned} \tag{4.7}$$

In the transformed variables, the equations of (4.6) become

$$\begin{aligned} &\sigma\frac{\partial\theta^I}{\partial\tau} - \frac{\partial^2\theta^I}{\partial\sigma^2} = 0, \\ &\theta^I(\sigma \to 0, \tau) = 1, \\ &\theta^I(\sigma \to \infty, \tau) = 0, \\ &\theta^I(\sigma, \tau \to 0) = 0. \end{aligned} \tag{4.8}$$

An exact solution to the equations of (4.8) was obtained by Acrivos (1960) using a "similarity" transformation, with similarity variable

$$\eta = 9^{-1/3}\frac{\sigma}{\tau^{1/3}},$$

to yield:

$$\theta^I(\eta) = 1 - \frac{1}{\Gamma(\frac{1}{3})}\int_0^{\eta^3} z^{-2/3}e^{-z}dz, \tag{4.9}$$

where $\Gamma(\cdot)$ denotes the Gamma function. Expressing the similarity variable in terms of the original variables,

$$\eta = 9^{-1/3}Pe^{-1/3}\sqrt{2x_1}x_2\left[\frac{2\sqrt{2}}{3}(1 - x_1^{3/2})\right]^{-1/3}, \tag{4.10}$$

and substituting (4.10) in (4.9) yields the leading-order temperature field, $\theta^I(x_1, x_2)$, in Region I.

The representation for the temperature field in the near-wall boundary-layer, obtained above, does not hold in regions where the wall shear-stress vanishes (Acrivos & Goddard 1965); at the no-slip critical point the shear-stress vanishes and (4.1) is then no longer the leading-order representation of ψ. Therefore, in the vicinity of the critical point we expect different convective-diffusive regimes with $x_1 < O(1)$, and where the dominant balance arguments of Region I do not hold. Before considering the domain near the critical point, we shall first obtain the inner equations for the boundary-layer straddling the dividing streamline. As we shall see, obtaining the appropriate scaled variables in Region III will considerably aid the inner-field analysis near the critical point.

4.2 Region III

The appropriate boundary-layer scalings in Region III will be obtained by a combination of a dominant balance argument and an overall thermal energy balance.

We let $x_1 = O(Pe^{-\alpha})$ and $x_2 = O(Pe^{-\beta})$ in the boundary-layer straddling the dividing streamline. The quantities α and β are unknown, with β satisfying: $\beta < 1/3$. Moreover, let $x_1 = O(Pe^{-\delta})$ and $x_2 = O(Pe^{-\gamma})$ in the transition region, or Region II, which connects regions I and III. The scalings in the thermal boundary-layer at the wall do not hold in the neighborhood of the no-slip critical point. The scalings in the boundary-layer straddling the dividing streamline are also expected to breakdown in the vicinity of the critical point. In between is a convection-diffusion regime – the transition region – which is of intermediate size, and we therefore set $\delta > 0$, $\gamma < 1/3$.

Heat diffusing into the fluid at the hot surface is, primarily, convected away through a narrow boundary-layer straddling the dividing streamline at distances much above the near-wall boundary-layer, $x_2 >> O(Pe^{-1/3})$. In other words, heat diffusing into the fluid at the near-wall boundary-layer and the transition region, is eventually channelled through a narrow layer along the dividing streamline, and an overall thermal energy balance requires, in mathematical terms, that these two quantities be of the same order. The microscopic heat or thermal energy balance for steady, incompressible flows is given, in dimensionless variables, by

$$\nabla.(u\theta - \frac{1}{Pe} \nabla \theta) = 0.$$

Integrating over the entire fluid area D interior to a closed envelope, determined by the wall, the dividing streamline, a line parallel to the wall running across the boundary-layer straddling the dividing streamline, and a line parallel to the dividing streamline intersecting the wall at $x_1 >> 1$, and using the divergence theorem, yields

$$Q_1 + Q_2 = 0,$$

where

$$Q_1 = \int_{\partial D_1} (u\theta - \frac{1}{Pe} \nabla \theta)(-j) ds$$

is the contribution due to the transfer of heat from the hot surface, with ∂D_1 representing the wall and j the unit-vector in the x_2-direction, while

$$Q_2 = \int_{\partial D_2} (u\theta - \frac{1}{Pe} \bigtriangledown \theta)(j) ds$$

is the contribution due to the convective and diffusive transport of heat through the boundary-layer straddling the dividing streamline, with ∂D_2 representing a horizontal cut across the boundary-layer. Since the velocity vector u vanishes at the no-slip boundary, it follows that the only contribution to Q_1 comes from the diffusive flux of heat through the near-wall boundary-layer and the transition region with, as we shall determine below, the former being the dominant contribution. One obtains,

$$Q_1 = \frac{1}{Pe}\left[Pe^{1/3} \int_0^1 \frac{\partial \theta^I}{\partial \hat{x}_2}|_{\hat{x}_2 \to 0} \, dx_1 + O(Pe^{\gamma-\delta}) \right], \tag{4.11}$$

where $\hat{x}_2$ is the scaled variable and θ^I the $O(1)$ temperature field, in Region I. One recalls, from §4.1, that x_1 is O(1) in Region I and since $(\gamma - \delta) < 1/3$, it follows that

$$Q_1 = O(Pe^{-2/3}).$$

This is a consequence of the fact that the dominant contribution to heat transfer at the wall is from the flux of heat into the near-wall boundary-layer; the flux of heat into the transition region near the no-slip critical point does not contribute, to leading-order. The possible existence of other convective-diffusive regimes interior to the transition region has not been discounted, but as long as their x_2-dimension is not less than that of the near-wall boundary-layer, i.e., $x_2 \geq O(Pe^{-1/3})$, their contribution to Q_1 would be necessarily less than $O(Pe^{\gamma-\delta-1})$ and therefore irrelevant to our asymptotic analysis. Since convection normal to the wall is more pronounced in the vicinity of the no-slip critical point than in the near-wall boundary-layer, it is reasonable to expect that the smallest convective-diffusive regime interior to the

transition region will not be narrower than the near-wall boundary-layer. We elaborate further on this at the end of Chapter 5. Thermal energy balance, therefore, requires that Q_2 must also be $O(Pe^{-2/3})$. We have,

$$Q_2 = \int_0^\infty (u_2\theta - \frac{1}{Pe}\frac{\partial\theta}{\partial x_2})|_{x_2}\, dx_1. \tag{4.12}$$

Since Q_2 determines the convective and diffusive efflux of heat across a horizontal surface ∂D_2, which is placed across the boundary-layer straddling the dividing streamline, (4.12) must be evaluated using the scaled coordinates of Region III. We had set $x_1 = O(Pe^{-\alpha})$ and $x_2 = O(Pe^{-\beta})$ in Region III, where $\beta < 1/3$. In addition, we assume $\beta > 0$. In physical terms, this implies that Region III necessarily decays in length with increasing Peclet number. The assumption will be justified later, but for now we will proceed with $0 < \beta < 1/3$. Since $u_2 = -\partial\psi/\partial x_1$, from (3.5)

$$u_2 = x_2^2 + O(x_2^3).$$

The convective and diffusive contributions to Q_2 are easily determined to be

$$u_2\theta = O(Pe^{-2\beta}),$$
$$\frac{1}{Pe}\frac{\partial\theta}{\partial x_2} = O(Pe^{\beta-1}).$$

Since $\beta < 1/3$, it follows that

$$\beta - 1 < -2\beta. \tag{4.13}$$

The relationship indicates that the dominant contribution to Q_2 comes from the convective flux of heat across ∂D_2. Defining scaled variables in Region III, $\tilde{x}_1 = Pe^{\alpha}x_1$, $\tilde{x}_2 = Pe^{\beta}x_2$, and expressing Q_2 in terms of the scaled variables, one obtains

$$\begin{aligned} Q_2 &= \int_0^\infty [Pe^{-2\beta}\tilde{x}_2^2\theta + O(Pe^{\beta-1})]Pe^{-\alpha}d\tilde{x}_1, \\ &= O(Pe^{-(\alpha+2\beta)}). \end{aligned}$$

Thermal energy balance, therefore, yields a relationship that determines the relative scales in Region III:

$$\alpha + 2\beta = \frac{2}{3}. \tag{4.14}$$

To completely determine α and β, an additional relationship is required and this is obtained from a dominant balance argument: in RegionIII, which is the boundary-layer straddling the dividing streamline, conduction normal to the dividing streamline must balance convection along it. Using the stream function of (3.5), and balancing appropriate terms in the differential operator of (3.4), one obtains another relationship between the coordinate scales in Region III:

$$2\alpha + \beta = 1. \tag{4.15}$$

Solving (4.14) and (4.15) completely determines α and β,

$$\alpha = \frac{4}{9},\ \beta = \frac{1}{9}. \tag{4.16}$$

In obtaining the above we had assumed $\beta > 0$. We still have to justify that assumption: allowing for $\beta \leq 0$ requires that we take into account the higher order terms of the velocity field in making an order-estimate of the convective contribution to Q_2, in which case it becomes necessary to verify that a higher order asymptotic expansion does not alter our conclusions. The analysis is now repeated with $\beta \leq 0$. Hence, we have $u_2\theta = O(Pe^{-n\beta})$, where now $n \geq 2$. From (4.13),

$$-n\beta > \beta - 1$$

for all $n \geq 2$ and $\beta \leq 0$, and the dominant contribution to Q_2 still comes from the convective rather than the diffusive flux. But now Q_2 is $O(Pe^{-(\alpha+n\beta)})$, and thermal energy balance requires

$$\alpha + n\beta = \frac{2}{3}. \tag{4.17}$$

The dominant balance argument now yields the following relationship

$$2\alpha + (n-1)\beta = 1. \tag{4.18}$$

It is easy to verify that for any $n \geq 2$, the linear simultaneous equations of (4.17) and (4.18) are not solved by any $\beta \leq 0$. For $n = 2$ these, of course, reduce to the equations of (4.14) and (4.15) which are solved by a pair of positive α and β, as given by (4.16). This completely justifies our previous assumption of positive β. Thus the size of the boundary-layer straddling the dividing streamline shrinks with increasing Peclet number and, since $\alpha > \beta$, the width decreases more rapidly than the length. It is important to note that because α and β are both positive quantities, it is sufficient to retain only the first term in the series expansion of the velocity field for the purposes of a asymptotic analysis. The advantage gained from the formulation of Chapter 2 is now obvious. Our discussion also indicates when it may not be possible to truncate to leading-order an asymptotic expansion for the velocity field and still seek a leading-order representation of the temperature field. Such a case is presented in the Appendix.

With $\tilde{x}_1 = Pe^{4/9}x_1$ and $\tilde{x}_2 = Pe^{1/9}x_2$ as the scaled variables in Region III, the asymptotic form of the thermal energy equation becomes

$$-2\tilde{x}_1\tilde{x}_2\frac{\partial\theta}{\partial\tilde{x}_1} + \tilde{x}_2^2\frac{\partial\theta}{\partial\tilde{x}_2} = \frac{\partial^2\theta}{\partial\tilde{x}_1^2} + O(Pe^{-1/9}), \tag{4.19}$$

$\tilde{x}_1 \in (0,\infty)$,$\tilde{x}_2 \in (0,\infty)$. Using the ansatz

$$\theta = \theta^{III}(\tilde{x}_1,\tilde{x}_2) + O(Pe^{-1/9}),$$

and a transformation to the pair of independent variables,

$$s = \tilde{x}_1\tilde{x}_2^2 = Pe^{2/3}x_1x_2^2, \tag{4.20a}$$

$$\rho = \frac{\tilde{x}_2^3}{3} = Pe^{1/3}\frac{x_2^3}{3}, \tag{4.20b}$$

one obtains the following boundary-value problem, to leading-order:

$$\frac{\partial \theta^{III}}{\partial \rho} = \frac{\partial^2 \theta^{III}}{\partial s^2}, \tag{4.21a}$$

$$\frac{\partial \theta^{III}}{\partial s}(s \to 0, \rho) = 0, \tag{4.21b}$$

$$\theta^{III}(s \to \infty, \rho) = 0, \tag{4.21c}$$

$$\theta^{III}(s, \rho \to 0) = \theta_o(s), \tag{4.21d}$$

$s \in (0, \infty)$,$\rho \in (0, \infty)$. The inner equation in Region III, (4.21a), is a "transient" diffusion equation with ρ as the time-like variable. It is easy to verify that (s, ρ) are "streamline-coordinates" to dominant order, where ρ is the coordinate along the streamline and s is the coordinate transverse to the streamline. Within the boundary-layer region of thickness $O(Pe^{-4/9})$, straddling the dividing streamline up to a length of $O(Pe^{-1/9})$, convection along streamlines is balanced by diffusion transverse to the streamline. The result is not unexpected since the streamlines are dominantly parallel to the dividing streamline in Region III. The first boundary condition (4.21b) is the symmetry condition arising from symmetry about the x_2-axis. Boundary condition of (4.21c) is also the matching condition with the outer solution of (3.10), while the last one is an unknown initial condition, to be obtained by matching the solution in Region III with that in the transition region. Using Fourier transforms and the method of images, the boundary-value problem of (4.21) is easily solved in terms of $\theta_o(s)$:

$$\theta^{III}(s, \rho) = \frac{1}{2\sqrt{\pi \rho}} \left\{ \int_0^\infty \theta_o(\acute{s}) \left[e^{-\frac{(s-\acute{s})^2}{4\rho}} + e^{-\frac{(s+\acute{s})^2}{4\rho}} \right] d\acute{s} \right\}. \tag{4.22}$$

The boundary condition (4.21c) at $s \to \infty$ is satisfied if and only if the initial value also vanishes at infinity:

$$\theta_o(s \to \infty) = 0. \tag{4.23}$$

The expression of (4.22) completely determines the asymptotic temperature field in Region III provided a $\theta_o(s)$, satisfying (4.23), can be obtained from an appropriate "matching condition." This warrants an asymptotic analysis of the transition region, which we perform below.

4.3 Region II

At the beginning of §4.2 we had set $x_1 = O(Pe^{-\delta})$ and $x_2 = O(Pe^{-\gamma})$ in the transition region, with δ and γ satisfying the following inequalities: $\delta > 0$, $\gamma < 1/3$. With α and β of (4.16) completely determining the size of Region III, we are now in a position to further improve the above inequalities. The sizes of the near-wall boundary-layer and the boundary-layer straddling the dividing streamline are now specified, and since the transition region connecting these two boundary-layers is of intermediate size, it follows immediately that

$$\begin{aligned} 0 < \delta < \frac{4}{9}, \\ \frac{1}{9} < \gamma < \frac{1}{3}. \end{aligned} \tag{4.24}$$

Moreover, an overall thermal energy balance would require, as in Region III, the relative scales in Region II be also determined from a relationship as in (4.14); the quantities δ and γ must therefore satisfy

$$\delta + 2\gamma = \frac{2}{3}. \tag{4.25}$$

The exact size of the transition region remains undetermined, but the inequalities of (4.24) are sufficient to obtain the asymptotic form of the thermal energy equation in this region. For any δ, γ lying within the range of values specified by (4.24), the thermal energy equation reduces to

$$-2\bar{x}_1\bar{x}_2\frac{\partial\theta}{\partial\bar{x}_1} + \bar{x}_2^2\frac{\partial\theta}{\partial\bar{x}_2} = O(Pe^{(\frac{1}{3}-3\gamma)}),$$

where $\bar{x}_1 = Pe^{\delta}x_1$, $\bar{x}_2 = Pe^{\gamma}x_2$ are the scaled variables in Region II, $\bar{x}_1 \in (0,\infty)$,$\bar{x}_2 \in (0,\infty)$. From (4.24), $(\frac{1}{3} - 3\gamma) < 0$ and, therefore, to dominant order

$$-2\bar{x}_1\bar{x}_2\frac{\partial\theta^{II}}{\partial\bar{x}_1} + \bar{x}_2^2\frac{\partial\theta^{II}}{\partial\bar{x}_2} = 0, \tag{4.26}$$

where θ^{II} represents the $O(1)$ temperature field in Region II. Setting $s = \bar{x}_1\bar{x}_2^2$, it follows that

$$\theta^{II} = \theta^{II}(s). \tag{4.27}$$

Expressing s in terms of the original unscaled variables gives $s = Pe^{(\delta+2\gamma)}x_1x_2^2$, and using the relationship of (4.25),

$$s = Pe^{2/3}x_1x_2^2. \tag{4.28}$$

We note that s is a scaled stream function. Therefore equation (4.27) can be interpreted in simple terms: to dominant order, the temperature field in the transition region is constant along streamlines. Notice also that s of (4.28) is identical to s of (4.20a), which explains the use of the same notation. This will be exploited in the asymptotic matching of the different convective-diffusive regimes.

Chapter 5

Asymptotic matching

The asymptotic representation of the steady temperature field in Region I at $Pe \to \infty$ is given by (4.9). This result, however, does not hold once we approach Region II. From (4.27), the temperature field in Region II, to dominant order, is constant along streamlines. But this result, in turn, breaks down as we approach Region I. There is an "overlap domain," of size $O(Pe^{-\delta}) < x_1 < O(1)$, where both solutions are valid. Matching of the two solutions in this overlap domain would yield a temperature distribution over streamlines in Region II, which can then be used as the "initial" profile in (4.21d) since temperature is constant along streamlines in the transition region. The requisite matching is accomplished by the method of matched asymptotic expansions.

We first match Region II with Region I. Using the conventional terminology (Van Dyke 1964) of matched asymptotic expansions, Region I is taken to be the "outer" region with respect to Region II, which is taken to be the "inner" region. The pair (x_1, s) are chosen as independent variables in the outer region, where s is given by (4.28). In the inner region, the pair $(\bar{x}_1, s)$ are chosen as independent variables, where $\bar{x}_1 = Pe^{\delta} x_1$ is the scaled variable of §4.3. The outer representation

is obtained by expressing (4.9) in terms of (x_1, s):

$$\theta^I(x_1, s) = 1 - \frac{1}{\Gamma(\frac{1}{3})} \int_0^{\eta^3} z^{-2/3} e^{-z} dz, \tag{5.1}$$

where the similarity variable η is now written as a function of the new pair of independent variables,

$$\eta = \left(\frac{1}{3}\right)^{1/3} \frac{\sqrt{s}}{(1 - x_1^{3/2})^{-1/3}}. \tag{5.2}$$

Since $x_1 = Pe^{-\delta} \bar{x}_1$ and, recalling from (4.24), $\delta > 0$, the inner representaion of the outer representation, which is simply the outer representation expanded in terms of the inner variables, becomes

$$\theta^I(\bar{x}_1, s) = 1 - \frac{1}{\Gamma(\frac{1}{3})} \int_0^{\frac{s^{3/2}}{3}} z^{-2/3} e^{-z} dz + \text{higher order terms.} \tag{5.3}$$

The inner representation is simply

$$\theta^{II} = \theta^{II}(s) \tag{5.4}$$

and, since s is both the inner and the outer variable, the outer representation of the inner representation is also given by (5.4). Therefore, the asymptotic matching principle (Van Dyke 1964) yields

$$\theta^{II}(s) = 1 - \frac{1}{\Gamma(\frac{1}{3})} \int_0^{\frac{s^{3/2}}{3}} z^{-2/3} e^{-z} dz. \tag{5.5}$$

It now remains to match Region II with Region III. The matching will be performed in a overlap domain, of size $O(Pe^{-\gamma}) < x_2 < O(Pe^{-1/9})$. Again, Region II is taken to be the "inner" region, while Region III is now the "outer" region with respect to Region II. The pair (s, x_2) are chosen as independent variables in the outer region, while $(s, \bar{x}_2)$ are chosen as independent variables in the inner region, where $\bar{x}_2 = Pe^{\gamma} x_2$ is the scaled variable of §4.3. The outer representation, given by (4.22),

is easily expressed in terms of (s, x_2) by replacing ρ of (4.20b) with $Pe^{1/3}x_2^3/3$. Since $x_2 = Pe^{-\gamma}\bar{x}_2$ and, recalling from (4.24), $\gamma > 1/9$, the inner representation of the outer representation is simply

$$\theta^{III} = \theta_o(s) + \text{higher order terms.} \tag{5.6}$$

The outer representation of the inner representation is again given by (5.4). The asymptotic matching principle yields

$$\theta_o(s) = \theta^{II}(s), \tag{5.7}$$

and therefore the "initial" condition to the diffusion problem of (4.21) is also given by the expression of (5.5). It is easy to verify that $\theta_o(s)$ vanishes at $s \to \infty$, as required by (4.23). Substituting for $\theta_o(s)$ in (4.22), the solution in Region III is complete:

$$\begin{aligned}\theta^{III}(s,\rho) = \frac{1}{2\sqrt{\pi\rho}}\Bigg[&\int_0^\infty \left(1 - \frac{1}{\Gamma(\frac{1}{3})}\int_0^{\frac{(\acute{s})^{3/2}}{3}} z^{-2/3}e^{-z}dz\right)e^{-\frac{(s-\acute{s})^2}{4\rho}}d\acute{s} \\ &+\int_0^\infty \left(1 - \frac{1}{\Gamma(\frac{1}{3})}\int_0^{\frac{(\acute{s})^{3/2}}{3}} z^{-2/3}e^{-z}dz\right)e^{-\frac{(s+\acute{s})^2}{4\rho}}d\acute{s}\Bigg].\end{aligned} \tag{5.8}$$

We end this Chapter with some concluding remarks on the possible existence of different convective-diffusive regimes interior to the transition region. The solution of (5.5) may not hold all the way up to the no-slip critical point. In particular, it is possible that there exists a domain around the critical point, of size $x_1 = O(Pe^{-1/3})$ and $x_2 = O(Pe^{-1/3})$, where convection balances diffusion and all the terms in the operator P of (3.4) are of equal order. We call this near-critical-point boundary-layer as Region II_a, for convenience. The boundary-layer problem in Region II_a, therefore, does not simplify even to dominant order and all terms in the thermal energy equation must be retained. We note, however, that the stream function

ψ in Region II_a is $O(Pe^{-1})$ while ψ in the transition region is $O(Pe^{-(\delta+2\gamma)})$, or, from (4.25), $O(Pe^{-2/3})$. Hence, the presence of Region II_a is irrelevant to the asymptotic analysis in the transition region and the convective-diffusive process in this region will not contribute to the leading-order-representation of the temperature field in the regions outer to it. But it must be kept in mind that the domain of validity of the asymptotic solution in the transition region, given by (5.5), might not include a near-critical-point boundary-layer of length $O(Pe^{-1/3})$ and thickness also $O(Pe^{-1/3})$.

Chapter 6

Comparison with numerical results

Supporting numerical evidence for the asymptotic result of (5.8) was obtained using a method based on the theory of Brownian motion, called the Wiener bundle method. The method has been used before to treat the convection-diffusion of magnetic field in magnetohydrodynamics (Molchanov, Ruzmaikin & Sokolov 1985, Klapper 1992) and also in the solution of heat conduction problems (Haji-Sheikh & Sparrow 1967). The method is also called a pseudo-Lagrangian method since it is a generalization of the Lagrangian solution for zero diffusivity. Consider the full dimensionless time-dependent evolution equation for the scalar field $\theta(x,t)$

$$\frac{\partial\theta}{\partial t} + u \cdot \nabla\theta = \frac{1}{Pe}\nabla^2\theta, \tag{6.1}$$

where $u = (u_1, u_2)$ is given by the asymptotic expansion of (2.2). Time t has been non-dimensionalised using the characteristic time-scale for convection, $1/K_1L$. At $Pe = \infty$, i.e., for the case of zero-diffusivity, (6.1) is solved by considering θ as constant along pathlines in the flow. Hence $\theta(x(x_o,t),t) = \theta(x_o,0)$, where $x(x_o,t)$ is the Lagrangian variable defined by $dx = udt$, $x(x_o,0) = x_o$. The zero-diffusivity Lagrangian solution can be generalized to the case of non-zero diffusivity, i.e., finite Pe, by averaging over a bundle of random (Wiener) trajectories. A Wiener

trajectory is generated using the stochastic differential

$$dx = udt + (2/Pe)^{1/2} dW_t, \tag{6.2}$$

where W_t is a two-dimensional Wiener process (McKean 1969). Since the Wiener process is the integral of the generalized stochastic white noise process, (6.2) is completely equivalent to the generalized Langevin equation,

$$\begin{aligned} \dot{x}_1 &= -\frac{\partial \psi}{\partial x_2} + \eta(t), \\ \dot{x}_2 &= \frac{\partial \psi}{\partial x_1} + \xi(t), \end{aligned} \tag{6.3}$$

where ψ is the stream function and $(\eta(t), \xi(t))$ is two-dimensional white noise, i.e., $\eta(t)$ and $\xi(t)$ are stationary stochastic processes with a Gaussian probability distribution, such that their autocorrelation is a delta function

$$< \eta(t)\eta(t') > = < \xi(t)\xi(t') > = \ (2/Pe)\delta(t - t'),$$

and their cross-correlation is zero,

$$< \eta(t)\xi(t') > = \ 0;$$

$< \cdot >$ denotes the expected value. Therefore, starting at a point x at time t and integrating backwards in time using (6.3) yields a "bundle" of Wiener trajectories, each of which starts from a random point x_o at $t = 0$ and reaches x at time t. Each Wiener trajectory carries with it the temperature of the point from which it originates, just as in the zero-diffusivity Lagrangian solution, and an expectation taken over the bundle of Wiener trajectories determines the temperature at point x at time t. The Wiener bundle solution of (6.1) is given by

$$\theta(x, t) = < \theta(x_o, 0) >, \tag{6.4}$$

where the average is taken over all Wiener trajectories starting at a random point x_o and ending at a given non-random point x in time t. That (6.4) is indeed a solution of (6.1) is a classical result (McKean 1969).

While the Wiener bundle method is generally inefficient for whole field computations, it offers the unique advantage of allowing calculation of the temperature at a single point without calculating the whole field. Therefore, when only a few point values are desired, the Wiener bundle method offers a distinct advantage over other numerical schemes. Moreover, the singular limit of large Pe is not easily tackled by numerical schemes that embrace the Eulerian approach and attempt to solve directly the partial differential equation of (6.1); using the Wiener bundle method it is easily possible to compute point values of the temperature at even very high Peclet numbers. Finally, a scalar transport problem in an unbounded domain poses some difficulty to say a finite-difference solution because of the far-field boundary conditions, which have to be specified at some finite distance in any implementation of the numerical scheme. No such difficulty is encountered in the Wiener bundle method.

The large-Pe asymptotic result of (5.8) was used to obtain a temperature profile over distance x_1 from the dividing streamline, at a distance $x_2 = 0.75$ from the wall and $Pe = 1000$. This is plotted as a solid line in figure 6.1(a); the plot is shown only for positive x_1-values since the result is symmetrical in x_1. Point values of temperature at several x_1 along $x_2 = 0.75$ were evaluated for $Pe = 1000$ at two different t using the Wiener bundle method, and these are also displayed in figure 6.1(a). The temperature value is obtained by integrating backwards in time a collection N of "particles" that are located at the given $(x_1, x_2 = 0.75)$ at time t, using the generalized Langevin equations of (6.3), where the stream function ψ is given by the asymptotic expansion of (3.5) truncated to leading order,

i.e., $\psi = -x_1 x_2^2$. Since a constant temperature wall can be treated as a perfectly absorbing boundary for a Brownian particle (Chandrasekhar 1943), the Wiener trajectory of a particle is terminated once it reaches the wall in backward time. The temperature θ at the point $(x_1, x_2 = 0.75)$ at time t is given by

$$\theta = \frac{1}{N} \sum_{i=1}^{N} \delta_{wi}, \tag{6.5}$$

where $\delta_{wi} = 1$ if the i^{th} particle reaches the heated portion of the wall before time t, and $\delta_{wi} = 0$ otherwise. Equation (6.5) is therefore an expectation over the temperature values "carried" by the Wiener trajectories that reach $(x_1, x_2 = 0.75)$ in time t. Point values of temperature were also computed at a smaller x_2, which are plotted in figure 6.1(b). Results at a lower Peclet number, $Pe = 500$, are displayed in figure 6.2(a,b); the solid line represents the asymptotic result of (5.8) in all four figures. In figure 6.1(b) the temperature falls off much less rapidly with increasing distance x_1 from the dividing streamline in contrast to figure 6.1(a), showing the thickening of the boundary-layer as the wall is approached. Comparing figures 6.1(a) and (b), the match between the numerical and the asymptotic result worsens at lower x_2, which is expected since the asymptotic result of (5.8) loses validity as we approach the transition region. The wider distribution of temperature in figures 6.2(a,b) indicates the thickening of the boundary-layer as the Peclet number decreases. Comparing figures 6.1(a) and 6.2(a), and 6.1(b) and 6.2(b), the peak value of temperature, $\theta(x_2 = 0)$, reduces only marginally despite doubling the Peclet number, indicating the slow decay ($O(Pe^{-1/9})$) in the length of the boundary-layer straddling the dividing streamline. We note that the number N of particles used to compute point values of $\theta(x, t)$ was taken to be $5\text{x}10^4$. Standard error estimates in Monte Carlo methods indicate the error is $O(N^{-1/2})$, which is small in comparison to the error in the asymptotic result, which is $O(Pe^{-6/9})$. It will also be noted that since it is the leading-order representation of the velocity field that has been used

in the numerical computations, the error due to higher order terms in the Taylor-series expansion of (2.4) has not been brought into consideration. The error in the representation of the temperature field in Region III is therefore only $O(Pe^{-6/9})$ and not $O(Pe^{-1/9})$.

Whole field computaions were also carried out at two moderately large Peclet numbers, $Pe = 50$ and $Pe = 100$, using finite difference; contour levels of temperature are plotted in figures 6.3(a) and (b), respectively. The full time-dependent equation of (6.1) was solved over a "computational box" $x_1 \in [-1.5, 1.5]$, $x_2 \in [0, 2]$. The initial profile $\theta(x_1, x_2, 0)$ was taken to be unity at the hot surface, ($|x_1| \leq 1, x_2 = 0$), and zero everywhere else, while the boundary conditions were specified in accordance with (3.6). The finite-difference solution involved updating temperature values at the nodes of a spatial mesh spread over the computational box at every time-step, until the temperature converged to a steady value at all nodes within $x_1 \in [-1, 1]$, $x_2 \in [0, 1]$. Comparing figures 6.3(a) and (b), it is evident that with increasing Pe, the temperature variations are confined closer to the wall and the dividing streamline, and that the boundary-layer straddling the dividing streamline decreases in both length and breadth with the breadth decreasing more rapidly than the length. Finally, we note that some error is incurred in specifying the far-field boundary condition at a finite x_2 in the finite-difference solution, $x_2 = 2$ in this particular case.

FIGURES

Figure 6.1: Point values of temperature at $t = 25$ and $t = 50$ for $Pe = 1000$, computed numerically at several $x_1 \geq 0$ and (a) $x_2 = 0.75$, (b) $x_2 = 0.5$, using the Wiener bundle method. The solid line represents the asymptotic solution of (5.8) at the same Pe.

Figure 6.2: Point values of temperature at $t = 20$ and $t = 50$ for $Pe = 500$, computed numerically at several $x_1 \geq 0$ and (a) $x_2 = 0.75$, (b) $x_2 = 0.5$, using the Wiener bundle method. The solid line represents the asymptotic solution of (5.8) at the same Pe.

Figure 6.3: Contour levels of the steady temperature field obtained using finite difference, at (a) $Pe = 50$, (b) $Pe = 100$.

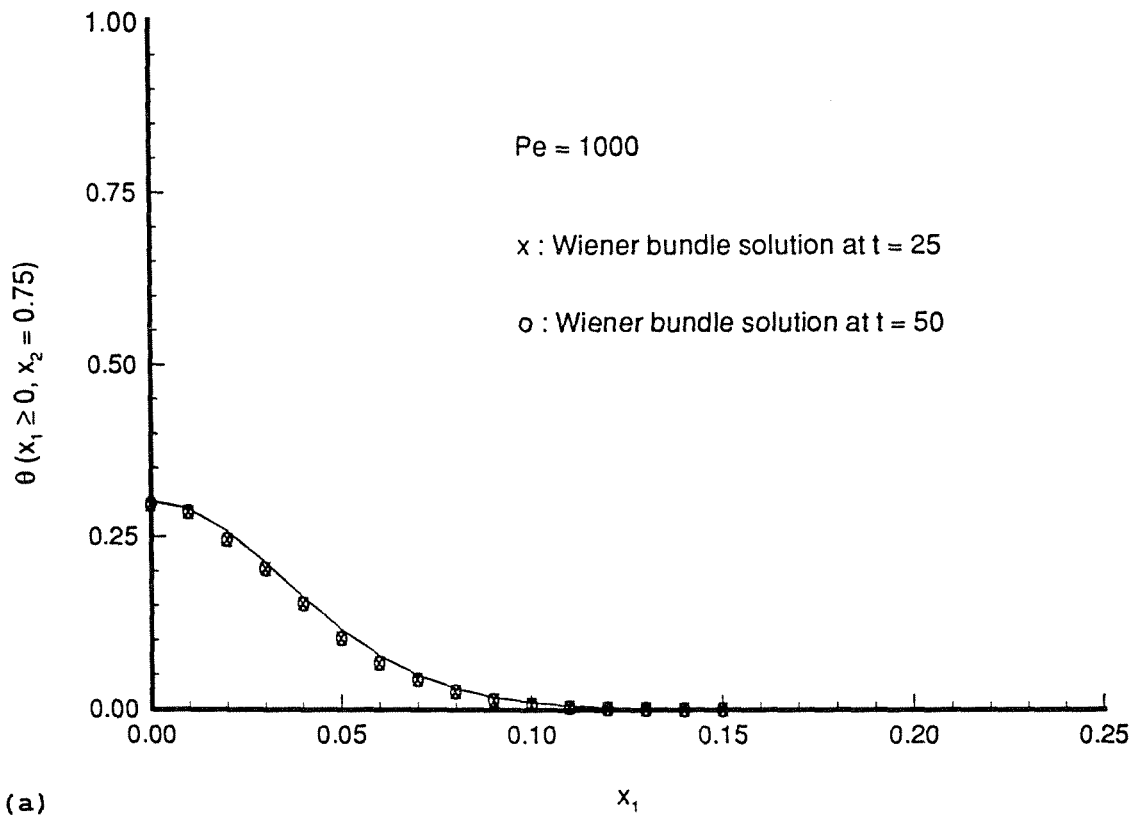
1.00
0.75
0.50
0.25
0.00
0.00
0.05
0.10
0.15
0.20
0.25
θ (x1 ≥ 0, x2 = 0.75)
x1
Pe = 1000
x : Wiener bundle solution at t = 25
o : Wiener bundle solution at t = 50
(a)

Figure 6.1(a)

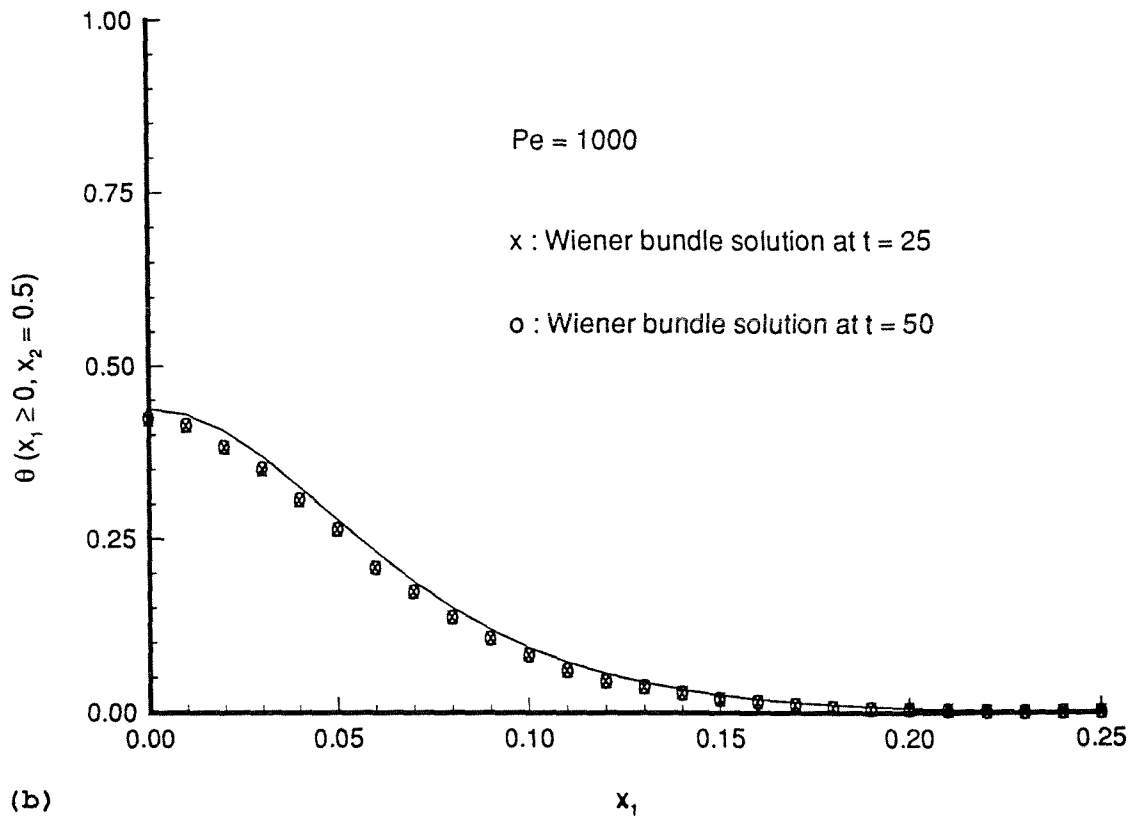
1.00
0.75
0.50
0.25
0.00
0.00
0.05
0.10
0.15
0.20
0.25
Pe = 1000
x : Wiener bundle solution at t = 25
o : Wiener bundle solution at t = 50
θ (x1 ≥ 0, x2 = 0.5)
x1
(b)

Figure 6.1(b)

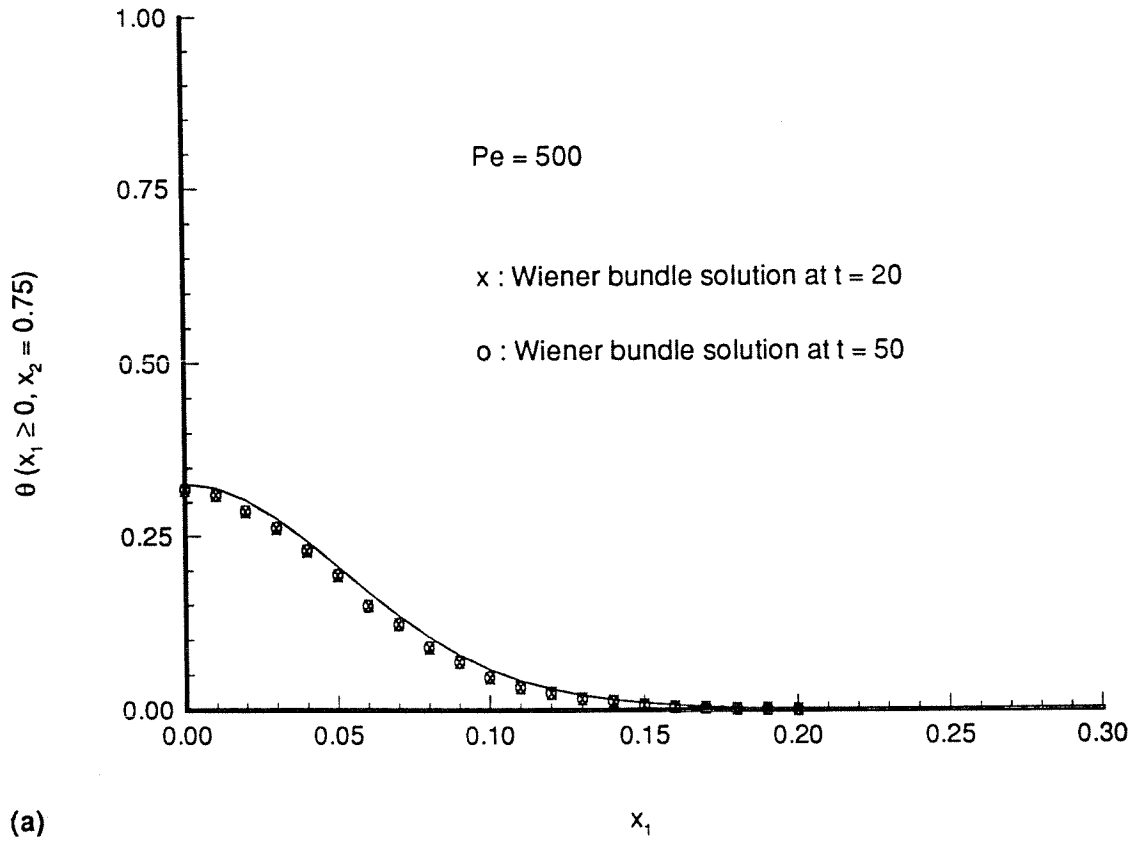
1.00
0.75
0.50
0.25
0.00
0.00
0.05
0.10
0.15
0.20
0.25
0.30
Pe = 500
x : Wiener bundle solution at t = 20
o : Wiener bundle solution at t = 50
θ (x1 ≥ 0, x2 = 0.75)
x1
(a)

Figure 6.2(a)

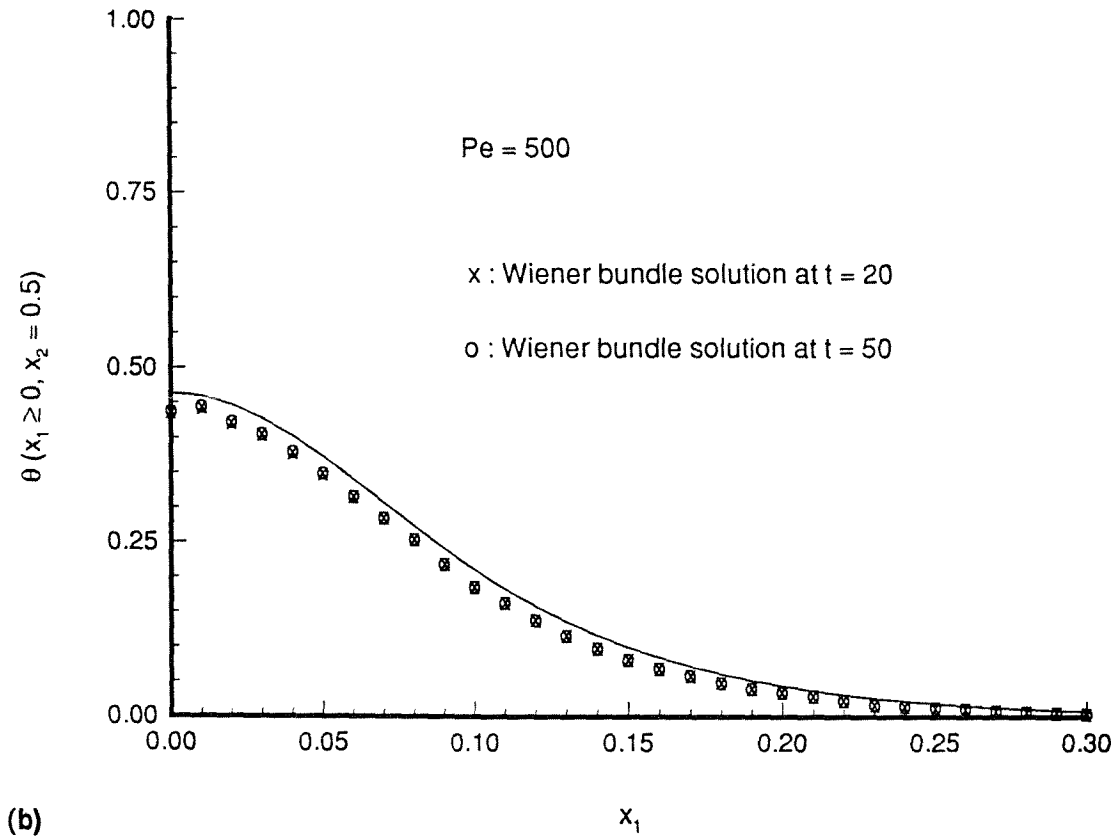
1.00
0.75
0.50
0.25
0.00
0.00
0.05
0.10
0.15
0.20
0.25
0.30
Pe = 500
x : Wiener bundle solution at t = 20
o : Wiener bundle solution at t = 50
θ (x1 ≥ 0, x2 = 0.5)
x1
(b)

Figure 6.2(b)

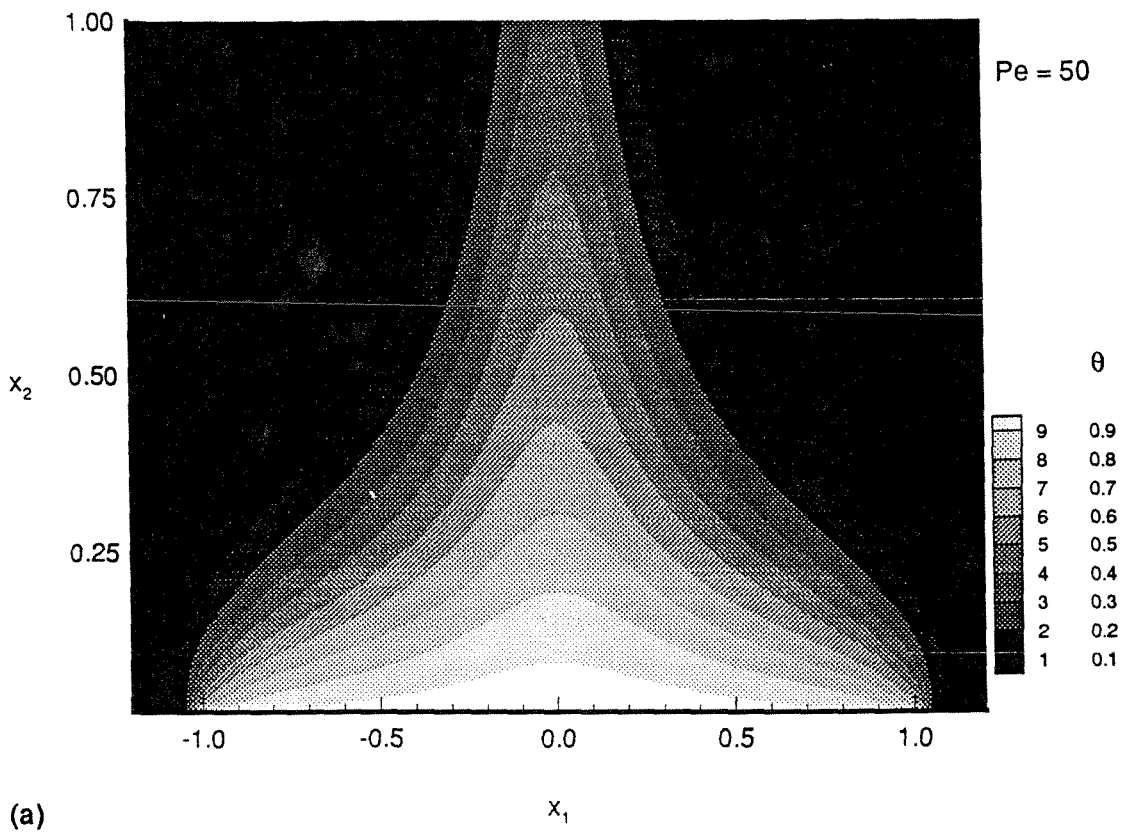
1.00
0.75
0.50
0.25
x_2
Pe = 50
θ
9 0.9
8 0.8
7 0.7
6 0.6
5 0.5
4 0.4
3 0.3
2 0.2
1 0.1
-1.0
-0.5
0.0
0.5
1.0
x_1
(a)

Figure 6.3(a)

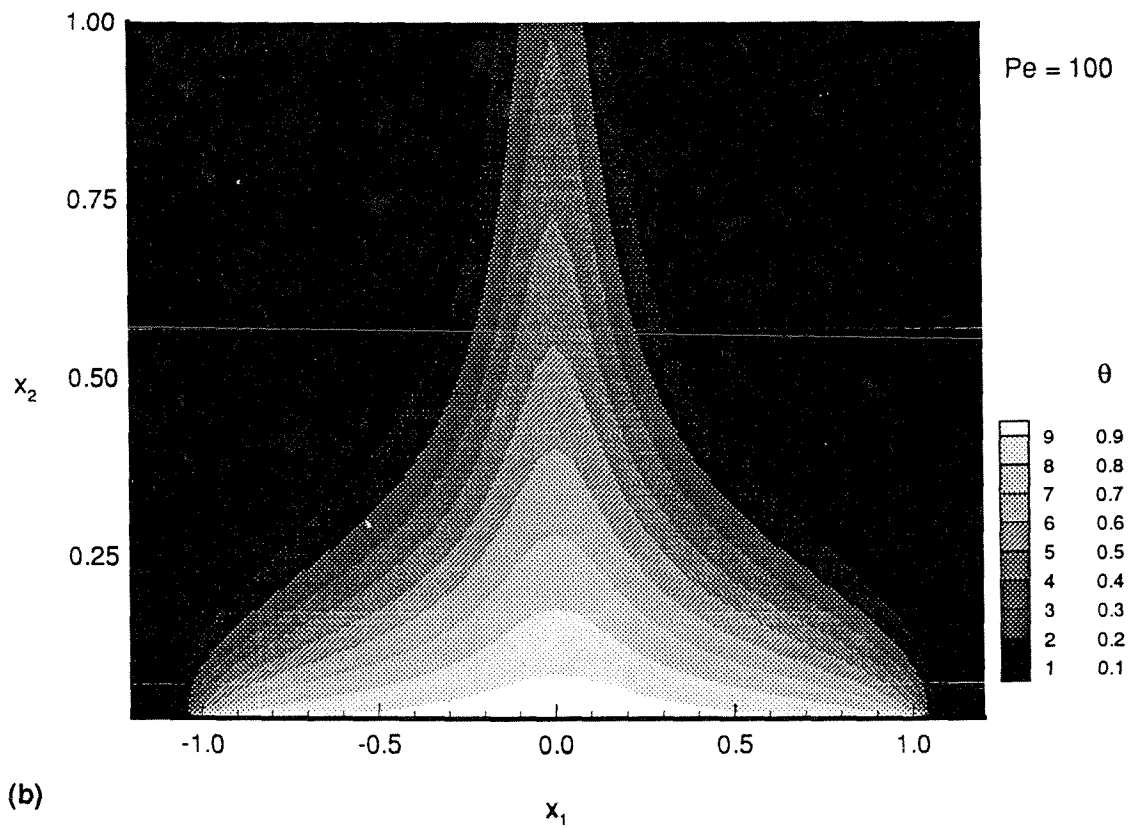
1.00
0.75
0.50
0.25
x_2
Pe = 100
θ
9 0.9
8 0.8
7 0.7
6 0.6
5 0.5
4 0.4
3 0.3
2 0.2
1 0.1
-1.0
-0.5
0.0
0.5
1.0
x_1
(b)

Figure 6.3(b)

Chapter 7

Conclusions

An asymptotic representation of the temperature field has been obtained for steady heat transfer in the vicinity of the no-slip critical point in normal plane separated flow at the small thermal diffusivity, large-Peclet-number, limit except possibly in a domain of length $O(Pe^{-1/3})$ and thickness $O(Pe^{-1/3})$ around the critical point. We have shown the existence of a boundary-layer of thickness $O(Pe^{-4/9})$, straddling the dividing streamline up to a distance of $O(Pe^{-1/9})$ above the hot surface. Since the x_1-dimension of this boundary-layer decays as one-ninth the exponent of the Peclet number, it shrinks very slowly with increasing Pe as compared to the x_2-dimension of the boundary-layer, and heat is convected away up to a fair distance from the hot surface even at moderately large Pe. In contrast, the near-wall boundary-layer is of thickness $O(Pe^{-1/3})$ and shrinks much more rapidly with increasing Peclet number. There is also a near-critical-point convection-diffusion region where the temperature is constant along streamlines. The temperature field in the boundary-layer straddling the dividing streamline approaches the asymptotic solution of (5.8) very slowly with increasing Peclet number, since it decays from this asymptote as $O(Pe^{-1/9})$. Finally, since the formulation used only the topology of normal plane separated flow, the results apply to an entire class of laminar flows: we

have obtained the temperature distribution, up to dominant order, for the steady, large-Pe transfer of heat from a "hot spot" at a no-slip boundary into any arbitrary viscous boundary-layer flow that has the topology of normal plane separated flow near a no-slip critical point, where the hot spot is located about the critical point. Our results apply to the transport of any passive scalar.

Appendix

Axisymmetric flow over a wall

Here we examine large-Peclet-number heat transfer from a local hot-spot at the no-slip critical point in viscous, incompressible axisymmetric flow over a wall. A local approximation to a spiral flow over a flat no-slip boundary with the one-dimensional unstable manifold of the no-slip critical point normal to the wall is constructed in the form of a asymptotic expansion from the critical point. Choosing (x_1, x_2) as canonical (Perry & Fairlie 1974) coordinates on the plane wall and x_3 the direction of the unstable manifold, the Taylor-series expansion method yields the following second-order approximation of the velocity field

$$u_1 = -K_1 x_1 x_3 - K_2 x_2 x_3 + O(3),$$

$$u_2 = K_2 x_1 x_3 - K_1 x_2 x_3 + O(3),$$

$$u_3 = K_1 x_3^2 + O(3),$$

where $K_1, K_2 > 0$. A transformation to cylindrical coordinates with $z \equiv x_3$ and (r, θ) on the plane wall, gives the following axisymmetric flow,

$$u_r = -K_1 r z + O(3),$$

$$u_z = K_1 z^2 + O(3), \qquad (A.1)$$

$$u_\theta = K_2 z + O(3),$$

where K_1 determines the stability of the no-slip critical point and for $K_1 > 0$ the flow is directed away from the wall, while K_2 determines the direction of rotation. The Stokes stream function ψ for the axisymmetric flow is obtained by setting $u_z = \frac{1}{r}\frac{\partial \psi}{\partial r}$, $u_r = -\frac{1}{r}\frac{\partial \psi}{\partial z}$, which gives

$$\psi = \frac{1}{2} K_1 r^2 z^2 + O(5).$$

A local hot-spot at the wall is modeled as a step change in temperature over a circle of radius L centered at the no-slip critical point, such that the temperature is T_w inside the circle and T_a everywhere else on the wall, with $T_w > T_a$. Temperature and space variables are non-dimensionalised as in the normal-plane-separated-flow problem, with the dimensionless temperature now represented by T instead of θ to avoid confusion with the angular variable. In dimensionless variables, the full heat transfer problem becomes

$$-\frac{1}{r}\frac{\partial \psi}{\partial z}\frac{\partial T}{\partial r} + \frac{1}{r}\frac{\partial \psi}{\partial r}\frac{\partial T}{\partial z} = \frac{1}{Pe}\left(\frac{1}{r}\frac{\partial}{\partial r}(r\frac{\partial T}{\partial r}) + \frac{\partial^2 T}{\partial z^2}\right),$$

$r \in (0, \infty)$, $z \in (0, \infty)$, with boundary conditions

$$T(r \to \infty, z) = 0,$$

$$T(r, z \to 0) = 1 - H(r-1),$$

$$T(r, z \to \infty) = 0,$$

where T is the dimensionless temperature, $Pe = K_1 L^3/\alpha$, and the dimensionless stream function, denoted again by ψ, is given by

$$\psi = \frac{1}{2} r^2 z^2 + O(5).$$

The problem is rendered two-dimensional, to dominant order, since the velocity field of $(A.1)$ is, to dominant order, independent of the azimuthal angle θ, while the temperature boundary conditions are also independent of θ.

As before, there are at least four-different convective-diffusive regimes: a near-wall boundary-layer (Region I), a transition region (Region II) in the vicinity of the no-slip critical point, a boundary-layer along the unstable manifold of the critical point (Region III), and a outer region (Region IV) where the solution, to dominant order, is zero everywhere. In Region I r is $O(1)$ and z is $O(Pe^{-1/3})$, and the asymptotic solution in the near-wall thermal boundary-layer is obtained in much the same manner as in the normal-plane-separated-flow problem. The solution for the $O(1)$ temperature T^I in the near-wall boundary-layer is identical to (4.9) with a slightly modified similarity variable,

$$\eta = 3^{-1/3} Pe^{1/3} rz(1-r^3)^{-1/3}.$$

To obtain the appropriate boundary-layer scalings in Region III, we again perform a thermal energy balance. As before, we let $r = O(Pe^{-\alpha})$, $z = O(Pe^{-\beta})$ in Region III, where $\beta < 1/3$, and let $r = O(Pe^{-\delta})$, $z = O(Pe^{-\gamma})$ in Region II, where $\delta > 0$, $\gamma < 1/3$. Proceeding as in §4.2, the heat Q_1 diffusing from the wall into the near-wall boundary-layer and the transition region is given by

$$\begin{aligned} Q_1 &= \frac{2\pi}{Pe}\left[Pe^{1/3} \int_0^1 \frac{\partial T^I}{\partial \hat{z}}|_{\hat{z}\to 0}\, r dr + O(Pe^{\gamma-2\delta}) \right], \\ &= O(Pe^{-2/3}), \end{aligned}$$

where $\hat{z} = Pe^{1/3} z$ is the scaled normal variable of Region I, while the heat Q_2 that is convected away through Region III

$$\begin{aligned} Q_2 &= 2\pi \int_0^\infty [Pe^{-2\beta}\tilde{z}^2 T + O(Pe^{\beta-1})] Pe^{-2\alpha}\tilde{r} d\tilde{r}, \\ &= O(Pe^{-(2\alpha+2\beta)}), \end{aligned}$$

where $\tilde{r} = Pe^{\alpha} r$, $\tilde{z} = Pe^{\beta} z$ are scaled variables in Region III. Since Q_1 and Q_2 must be of the same "order," it follows that the relative scales in Region III are determined by

$$\alpha + \beta = \frac{1}{3}.$$

The dominant balance argument of §4.2 still applies and it provides an additional relationship between α and β,

$$2\alpha + \beta = 1,$$

which completely determines the scalings in Region III:

$$\alpha = \frac{2}{3},\ \beta = -\frac{1}{3}.$$

Unlike the normal-plane separated-flow problem, we now have $\beta < 0$; since Region III shrinks in lateral extent much more rapidly ($\sim Pe^{-2\alpha}$) in the axisymmetric-flow problem, it has to grow in length with increasing Pe in order to maintain thermal energy balance. However, the result of $\beta < 0$ poses a problem: $z = O(Pe^{1/3})$ in Region III, which means the thermal boundary-layer along the unstable manifold of the no-slip critical point grows away from the critical point with increasing Pe. This conclusion was reached by proceeding with a local approximation of the velocity field, constructed as a second order asymptotic expansion from the critical point, where the higher order terms were ignored. But if $z = O(Pe^{1/3})$, higher order terms in the velocity field will contribute to leading-order in a asymptotic representation of the temperature field. Hence, in contrast to the normal-plane-separated-flow problem, a asymptotic representation of the temperature field in Region III cannot be obtained using the truncated velocity field of (2.2). Moreover, the result of $\beta = 1/3$ is itself in doubt since the order estimate of (3.4) was obtained using the truncated velocity field of (2.2); for $\beta < 0$, the higher order terms in the velocity field make the leading-order contribution to Q_2 and accounting for these might well modify the result obtained in (3.5).

References

Acrivos, A. 1960 Solution of the laminar boundary layer energy equations at high Prandtl numbers. *Phys. Fluids* **3**, 657.

Acrivos, A. & Goddard, J.D. 1965 Asymptotic expansions for laminar forced-convection heat and mass transfer. Part 1. Low speed flows. *J. Fluid Mech.* **23**, 273.

Chandrasekhar, S. 1943 Stochastic problems in Physics and Astronomy. *Rev. Mod. Phys.* **15**, 1.

Dallmann, U. 1983 Topological structures of three-dimensional flow separation. *DFVLR Rep. No.* IB 221-82 A07 (Göttingen, Germany).

Haji-Sheikh, A. & Sparrow, E.M. 1967 The solution of heat conduction problems by probability methods. *J. Heat Transfer, Trans ASME Series C* **89**, 121.

Herbeck, M. 1954 Approximate solutions for heat transfer with convection flows. *J. Aero. Sci.* **21**, 142.

Klapper, I. 1992 A study of fast dynamo action in chaotic helical cells. *J. Fluid Mech.* **239**, 359.

Ladyzhenskaya, O.A. 1975 Mathematical analysis of Navier-Stokes equations for incompressible flows. *Ann. Rev. Fluid Mech.* **7**, 249.

Levich, V.G. 1962 *Physico Chemical Hydrodynamics.* Prentice-Hall.

Lighthill, M.J. 1950 Contributions to the theory of heat transfer through a laminar

boundary layer. *Proc. Roy. Soc. Lond.* **A202**, 359.

McKean, H.P. 1969 *Stochastic Integrals.* Academic.

Molchanov, S.A., Ruzmaikin, A.A. & Sokolov, D.D. 1985 Kinematic dynamo action in random flow. *Sov. Phys. Usp.* **28**, 307.

Morgan, G.W. & Warner, W.H. 1956 On heat transfer in laminar boundary layers at high Prandtl number. *J. Aero. Sci.* **23**, 937.

Nadim, A.,Cox, R.G. & Brenner, H. 1986 Taylor dispersion in concentrated suspensions of rotating cylinders. *J. Fluid Mech.* **164**, 185.

Perry, A.E. & Chong, M.S. 1986 A series-expansion study of the Navier-Stokes equations with applications to three-dimensional separation patterns. *J. Fluid Mech.* **173**, 203.

Perry, A.E. & Chong, M.S. 1987 A description of eddying motions and flow patterns using critical-point concepts. *Ann. Rev. Fluid Mech.* **19**, 125.

Perry, A.E. & Fairlie, B.D. 1974 Critical points in flow patterns. *Adv. Geophys.* **18B**, 299.

Schlichting, H. 1962 *Boundary Layer Theory.* McGraw-Hill. .

Shraiman, B.I. 1987 Diffusive transport in a Rayleigh-Bénard convection cell. *Phys. Rev.* **A36(1)**, 261.

Tobak, M. & Peake, D.J. 1982 Topology of three-dimensional separated flows. *Ann. Rev. Fluid Mech.* **14**, 61.

Van Dyke, M. 1964 *Perturbation Methods in Fluid Mechanics.* Academic.